UNIVERSITY OF SOUTHAMPTON

Faculty of Social and Human Sciences

School of Mathematics

Mathematical modelling of tissue metabolism and growth

by

Christopher Joseph Catt

Thesis for the degree of Doctor of Philosophy

October 2010

UNIVERSITY OF SOUTHAMPTON

ABSTRACT

FACULTY OF SOCIAL AND HUMAN SCIENCES

SCHOOL OF MATHEMATICS

Doctor of Philosophy

MATHEMATICAL MODELLING OF TISSUE METABOLISM AND GROWTH

by Christopher Joseph Catt

The work presented in this thesis is concerned with modelling the growth of tissue constructs, with particular focus on the effects the local micro environment has on the cell cycle and metabolism. We consider two cases; multicellular tumour spheroids and orthopaedic tissue constructs. This thesis is divided into two parts. In the first part we will present a multispecies model of an avascular tumour that studies how a cell's metabolism affects the cell cycle, spheroid growth and the mechanical forces that arise during growth. The second part consists of a study of the growth of an engineered cartilaginous tissue layer. Experimental observations will be compared to a model of the distribution of cells and extracellular matrix.

The efficiency of cancer treatments such as radiotherapy and chemotherapy are sensitive to the local environment of a cell. Therefore an essential task in tumour biology is to understand the microenvironment within a tumour. Many mathematical models study the effects of nutrients and waste products, usually assuming growth is limited by the diffusion of a single nutrient. We will look in detail at the metabolic pathways from which cells obtain energy (ATP). A multispecies model is presented that considers the transition from aerobic to anaerobic respiration and includes relevant chemical and ionic buffering reactions and transport mechanisms. Results show that potential ATP production affects the cell cycle and consequently the rate of growth. This model is simplified using mathematical analysis and is integrated with a morphoelastic model to study the development of mechanical forces. The model shows that mechanical effects are particularly important during necrosis, where large tensile forces are shown to develop. A review of the equations governing nutrient conservation is given, by developing alternative macroscopic equations based on the microscopic features of a tumour using homogenization techniques.

The second part of this thesis studies the growth of cartilaginous tissue. Bio-materials are being engineered in an attempt to replace dysfunctional tissue in the human body using cells extracted from living organisms. We model the growth of a cartilaginous tissue construct that has been grown from expanded chondrocytes seeded onto collagen coated filters. A model is developed to explain the distribution of cells and the concentration and distribution of collagen and GAGs. This is achieved by studying the local environment of the cells. Model predictions are compared to a range of experimental data and show most of the growth takes place in the upper region of the construct.

Contents

List of tables **v**

List of figures **ix**

DECLARATION OF AUTHORSHIP **x**

List of publications **xi**

Acknowledgements **xii**

1 Introduction **1**

2 Modelling the effects of metabolism on the growth of tumour spheroids **3**

2.1 Introduction 3

2.2 Literature review of cell metabolism 7

2.3 Review of Casciari's multispecies model 15

2.4 Tumour modelling: Full model 17

2.4.1 Diffusion coefficients 19

2.4.2 Charge migration 20

2.4.3 Conservation of cells 21

2.4.4 Initial and boundary conditions 22

2.4.5 Production terms 24

2.4.6 Growth . . . 30
2.4.7 Summary of modelling equations . . . 31
2.4.8 Parameters and data fitting . . . 32
2.4.9 Results and discussion of full model . . . 34
2.5 Tumour modelling: Simple model . . . 40
2.5.1 Analysis of full model and derivation of simplified model . . . 41
2.5.2 Metabolic reactions . . . 42
2.5.3 Growth . . . 43
2.5.4 Summary equations for the simplified model . . . 44
2.5.5 Parameters and fitting . . . 45
2.6 Results and discussion of simple model . . . 46
2.7 Discussion . . . 48

3 Mechanical forces within a growing MCTS 50

3.1 Introduction . . . 50
3.2 Literature review . . . 51
3.3 Morophoelasticity model . . . 53
3.4 Incompressible limit . . . 56
3.5 Sensitivity analysis . . . 58
3.6 Results . . . 60
3.7 Application to a sliced tumour . . . 66
3.8 Results . . . 67
3.9 Discussion . . . 68

4 Diffusion through a cellular region **70**

4.1 Introduction . . . 70

4.2 Homogenization theory . . . 70

4.3 Diffusion model . . . 71

4.3.1 Case 1: $\beta < 2$ . . . 73

4.3.2 Case 2: $\beta = 2$ . . . 75

4.3.3 Case 3: $\beta \geq 3$ . . . 78

4.4 Application to tumours . . . 78

4.4.1 Example 1: Ellipsoid cells . . . 78

4.4.2 Example 2: Spherical cells . . . 81

4.5 Discussion . . . 84

5 Modelling of engineered orthopaedic tissue **85**

5.1 Introduction . . . 85

5.1.1 Tissue and cartilage . . . 86

5.2 Literature review . . . 88

5.2.1 Metabolism and the role of oxygen . . . 89

5.2.2 Experimental . . . 91

5.2.3 Mathematical modelling . . . 92

5.3 Experimental setup . . . 94

5.3.1 Tissue processing; histology and quantitative assays . . . 95

5.3.2 Data analysis . . . 96

5.4 Review of the experimental data . . . 101

5.5 Cartilage layer model . . . 101

5.6 Modelling equations . . . 103

5.6.1 Source terms . . . 105

5.6.2 Collagen and growth . . . 106
5.6.3 Initial conditions . . . 107
5.6.4 Boundary conditions . . . 108
5.6.5 Model simplifications . . . 112
5.6.6 Full system of equations . . . 112
5.6.7 Parameters and fitting . . . 113
5.7 Method and results . . . 115
5.8 Discussion . . . 118

6 Conclusions **122**

A Nondimensional analysis of full tumour model **125**

B Nondimensional analysis of full tumour model **128**

C Tissue images **130**

Bibliography **130**

List of Tables

2.1 Data from Figure 3 in [56] showing the thickness of the viable rim for EMT6/Ro tumour spheroid grown in medium with various concentrations of oxygen, glucose. Oxygen and glucose concentrations specified for the surrounding medium 13

2.2 Initial concentrations, diffusion coefficients and Sherwood coefficients for the chemical species. The Sherwood numbers N_{sh_i}, denote the rate of transfer of a species across the spheroid surface and are a function of the spheroid radius S such that $N_{sh_i} = 1 + Nsc \cdot 10^4 \cdot S^{1.099}$. 19

2.3 Table of parameters given in the literature for the full model. 27

2.4 Fitted parameters for the full model. 34

2.5 Table of parameters given by the literature for the simple model. 44

2.6 Fitted parameters for the simple model. 45

3.1 Values of sensitivity to growth parameter κ. 61

5.1 Parameters resulting from the experimental setup and data. 98

5.2 Parameter values taken from the literature. 106

5.3 Fitted parameters values. 114

A.1 Nondimensional constants. 127

List of Figures

2.1 A schematic of the cell cycle showing the ordered phases. 6

2.2 Sketch of a growing MCTS broken down into regions based on cell activity. . . 7

2.3 Schematic of the diffusion of nutrients and waste products. Nutrients diffuse into the tumour from the surrounding medium and are consumed by the cells, whilst waste products are synthesized inside the tumour and diffuse out. 20

2.4 A schematic of the boundary layer that surrounds the tumour spheroid. The size of the tumour is denoted by $S(t)$, whilst the boundary layer is of size Δ. . 22

2.5 Comparison of possible expressions to represent the consumption rate of oxygen. P_{ox}^{max} (- - -) is shown alongside the expression used by Casciari *et al.* [24] (—), a Michaelis Menten expression specifically fitted to the data (+) and experimental data (o) [22]. 33

2.6 Growth derived by solving the full tumour model (—) and fitting to experimental data (o, +) [97]. 35

2.7 The concentration of oxygen (**A**) and glucose (**B**) through tumour spheroids of radii 200μm (+), 500μm (- - -) and at the final size of 1435μm (—). 36

2.8 **A**: The average consumption rates of the spheroid for oxygen (—) and glucose (—) compared against experimental data (+, o) [54]. **B**: The concentration of oxygen at the centre (—) and surface (—) of a tumour compared against experimental data (+, o) [122]. 37

2.9 **A**: The size of the proliferating (—×—) and viable (—), rims. **B**: The concentration of ATP through tumour spheroids of radii 200μm (+), 500μm (- - -) and at the final size of 1435μm (—). 37

2.10 The concentration of carbon dioxide (**A**) and lactate (**B**) through tumour spheroids of radii $200\mu m$ (+), $500\mu m$ (- - -) and at the final size of $1435\mu m$ (—). 39

2.11 The pH (**A**) and electric potential gradient (**B**) through tumour spheroids of radii $200\mu m$ (+), $500\mu m$ (- - -) and at the final size of $1435\mu m$ (—). 40

2.12 The diameter of spheroid (**A**) and concentration of oxygen at the spheroid surface (**B**), predicted for Sherwood numbers of $N_{sh_i} \cdot 10^{-2}$ (+), N_{sh_i} (- - -) and $N_{sh_i} \cdot 10^{2}$ (—). 40

2.13 Growth derived by solving the simplified model (—) and fitting to experimental data (o, +) [97]. 46

2.14 The concentration of oxygen (**A**) and glucose (**B**) through tumour spheroids of radii $200\mu m$ (+), $500\mu m$ (- - -) and at the final size of $1392\mu m$ (—). 47

2.15 The concentration of ATP (**A**) and averaged velocity (**B**) through the tumour spheroid, at radii of $200\mu m$ (+), $500\mu m$ (- - -) and at the final size of $1392\mu m$ (—). 47

2.16 **A**: The average consumption rates of the spheroid for oxygen (—) and glucose (—) compared against experimental data (+ , o) [54]. **B**: The concentration of oxygen at the centre (—) and surface (—) of a tumour compared against experimental data (+, o) [122]. 48

3.1 The rate of growth (**A**), and velocity (**B**) through a tumour spheroid of radii $250\mu m$ (+), $339\mu m$ (- - -) and $500\mu m$ (—). 60

3.2 The radial stress (**A**), circumferential stress (**B**), radial stain (**C**) and circumferential strain (**D**) through a tumour of radii $250\mu m$ (+), $339\mu m$ (- - -) and $500\mu m$ (—) in which growth is insensitive to stress. 62

3.3 The radial stress (**A**), circumferential stress (**B**), radial stain (**C**) and circumferential strain (**D**) through a tumour spheroids of radii $250\mu m$ (+), $339\mu m$ (- - -) and $500\mu m$ (—) in which $\kappa\mu = \mathcal{O}(1)$. 63

3.4 The radial stress (**A**), circumferential stress (**B**), radial stain (**C**) and circumferential strain (**D**) through a tumour spheroids of radii $250\mu m$ (+), $339\mu m$ (- - -) and $342\mu m$ (—) in which growth is highly sensitive to stress. 64

3.5 Geometry used for COMSOL simulation of sliced MCTS. 67

3.6 Nondimensional deformation of a sliced tumour spheroid with radius 500μm. The darkest regions indicate areas of greatest expansion, whilst the lightest region indicates greatest contraction. 68

4.1 Schematic of the periodic array of cells. 71

4.2 Schematic of the microscopic (**A**) and macroscopic (**B**) setup considered. . . . 72

4.3 Ellipsoid cell contained inside periodic region implemented in COMSOL simulation. 79

4.4 Graphical solutions to the first order problem for χ_i. Plot **A** shows the solution to χ_1, **B** to χ_2 and **C** to χ_3. 80

4.5 Schematic of a spheroid cell contained inside its periodic region. 81

4.6 Graphical solutions to the first order problem for χ_i. Plots **A**, **B** and **C** show the solutions to χ_1, χ_2 and χ_3 respectively. 82

4.7 Two dimensional schematic of the cubic (**A**) and face centred cubic lattice (**B**) packing arrangements. Arrowed lines and hashed circles indicate the flow of nutrients. 84

5.1 Schematic of the Millipore filter and layer of cartilage. 94

5.2 Tissue samples at 14 (**A**) and 49 days (**B**). The staining indicates the presence of collagen (blue) and GAGs (red). The cells can be seen as darker dots, distributed throughout the tissue but at highest density at the surface of the membrane and at the surface of the tissue. 95

5.3 A sample of an analysed slice of tissue. The original sample (**A**), the adjusted image (**B**), and the one dimensional image (**C**), are given. 96

5.4 Histograms showing the averaged distribution of cells through the tissue samples. The first bar of each histogram represents the cell density next to the Transwell membrane in the lower band. The right hand bar in each histogram is the cell density in the upper band at the tumour surface. The bars in between represent the cell density in the central region. The height of each band is approximately 15μm. 97

5.5 Data showing the distribution of GAG within the structure at 49 days (**A**) and the accumulated quantity of GAG released (**B**). 99

5.6 Data showing the average height of the tissue over time (**A**), and the number of cells per tissue slice (**B**). The experimental data (+), averaged data (—) and a linear fit to the averaged data (- - -) are given. 99

5.7 Experimental data showing the number of cells in the lower band (—), upper band (-o-) and in the central region (- - -). Both the lower and upper bands are $15\mu m$ high. 100

5.8 Schematic of the idealised model and modelling notation. The upper and lower bands are $15\mu m$ in height. The cells in the upper band are proliferating whilst the cells in the lower band are quiescent. The central region contains cells producing collagen and GAGs and increases in depth over time. 102

5.9 Schematic of the modelling equations. 111

5.10 Height of the central region. Experimental data (o) and linear fit (+) are given alongside the modelling result (—). 113

5.11 Density of cells within the central region at 14, 21 and 31 days. The histograms show the averaged experimental data, whilst the continuous line represents the results of the model. 115

5.12 Density of cells within the central region at 35, 42 and 49 days. The histograms show the averaged experimental data, whilst the continuous line represents the results of the model. 116

5.13 The density of cells producing collagen (**A**), and the velocity of growth (**B**) through the central region at 14 (—), 31 (- - -) and 49 days (+). 117

5.14 The density of cells producing GAGs (**A**) and the density of GAG (**B**) through the central region at 14 (—), 31 (- - -) and 49 days (+). 117

5.15 **A**: Distribution of GAG through the central region at 49 days (—) compared to experimental data (- - -). **B**: Total mass of GAG released from the tissue layer (—) alongside GAG released through the Transwell membrane (- - -), the upper surface (++) and experimental data (o). 118

B.1 Convergence plot of the finite difference code used to solve the simplified tumour model in Chapter 2. The log of the error when solving the model using 5, 10, 20 and 40 grid points compared to the result using 80 grid points is shown (+) against a fit of all four error points (—) and a fit of the final three error points (- - -). The corresponding gradients of the fitted curves are -2.441 and -2.003. . 129

DECLARATION OF AUTHORSHIP

I, Christopher Joseph Catt, declare that the thesis entitled "Mathematical modelling of tissue metabolism and growth" and the work presented in the thesis are both my own, and have been generated by me as the result of my own original research. I confirm that:

- this work was done wholly or mainly while in candidature for a research degree at this University;
- where I have consulted the published work of others, this is always clearly attributed;
- where I have quoted from the work of others, the source is always given. With the exception of such quotations, this thesis is entirely my own work;
- I have acknowledged all main sources of help;
- where the thesis is based on work done by myself jointly with others, I have made clear exactly what was done by others and what I have contributed myself;
- none of this work has been published before submission.

Signed:

Date:

List of Publications

1. R.J. Shipley, G.W. Jones, R.J. Dyson, B.G. Sengers, C.L. Bailey, C.J. Catt, C.P. Please, and J.Malda. Design criteria for a printed tissue engineering construct: A mathematical homogenization approach. *Journal of Theoretical Biology*, 259(3):489502, 2009.

Acknowledgements

During the last three years I have been very fortunate to work with a range of talented and understanding academics. Above all I would thank Colin Please; my ramblings must have seemed endless and questions trivial, but yet his enthusiasm and tolerance has appeared unwavering; thank you. I am particularly grateful to Tiina Roose, for her guidance on all things biology related and her tireless efforts to make my work resemble something like the English language. I would also like to thank our Dutch friends, Jos Malda, Bram Sengers and Wouter Schuurman, they have endured a regular deluge of 'weird' questions, but without whom this thesis would look very different.

I would like to thank the members of QUT for making my stay so enjoyable and to give my biggest thanks to Pam and Robyn Please, for letting me into their home and making me feel so welcome during an experience I will never forget.

My thanks also go to the post-grads at the University of Southampton, in particular those who have deciphered my philosophising, made sense of my pictures and taken this journey with me. Lastly I would like to thank my family and friends; many of you will never read this and if you are, I suggest for the sake of your sanity you stop now, but thank you for humouring my incomprehensible rants, keeping me sane and for reminding me there is a real world outside the bubble I have so contently resided within. And finally, to the question I have been asked countless times... No but we did try.

To Lily

Chapter 1

Introduction

Mathematical modelling in biology is a rapidly growing area, both in terms of the resources allocated to research and the range of problems being studied. Compared to other scientific disciplines, mathematics has played a relatively small role in biology, however the potential for development is huge and, although still in its infancy, bio-mathematics has already been applied to a diverse variety of problems, ranging from neuroscience to ecology and ecosystems.

In this thesis we shall study two closely related biological problems that share many properties but have had differing levels of mathematical attention thus far. These are the growth of tumours and the growth of engineered tissue. Since early work by Burton [18] and Greenspan [68] the mathematical modelling of tumour growth has developed such that at present over 90,000 articles can be found by using a simple Google scholar search for 'mathematical model tumour OR tumor'. An equivalent search for 'mathematical model cartilage' returns a relatively small 16,000 articles. With a much lower library of literature regarding tissue, there are obviously many more areas to explore, but equally less knowledge to base these models on.

This thesis will principally consist of two parts. The first part, containing Chapters 2, 3 and 4, will be focused on modelling the growth of multicellular tumour spheroids. Whilst the second part, Chapter 5, will study the growth of cartilage tissue. Each chapter will begin with a brief introduction and overview of the background knowledge that forms the basis of the following work. Similarly each chapter will end with a discussion of the results that have been derived and the possible consequences to the model and future research.

Multicellular tumour spheroids are often used to model tumour growth due to the simplicity of their structure and their similarity to tumours found *in vivo*. In Chapter 2 we shall study the growth of a tumour spheroid, focusing on how the metabolism of the cell affects its energy requirements and how the energy is obtained. A review of the cell cycle and literature regarding cell metabolism is given, followed by a mathematical model that studies the growth of a tumour

spheroid, that includes all relevant chemical species and transport methods. This model is then compared to experimental data before being simplified to a reduced model that also simulates the growth of a tumour spheroid but only includes the components that have the most effect.

In Chapter 3 the simplified model of tumour growth is used to study the mechanical forces that develop inside a growing tumour spheroid. The various different approaches to studying tumour mechanics is discussed, before a detailed explanation of a morphoelastic model that was proposed by Hall [71]. This morphoelastic model is then implemented and used to derive the stresses and strains that are generated. A potential application to experimental data will then be given, showing the deformation of a tumour that has been sliced in half.

The final study of tumour growth will be given in Chapter 4. This will review the governing equations used to study the nutrient concentration, by developing alternative macroscopic equations, based on the microscopic features of the tumour using homogenization theory. Features of these resulting equations will then be shown using example geometries and by making comparisons to known data.

A study of the *in vitro* growth of a layer of cartilage tissue will be given in Chapter 5. The ideas that form the eventual model are based on both the experimental literature and experimental data. Thus a review of tissue metabolism and structure is given, followed by a review of the experimental data and a discussion of the possible characteristics that result from the data analysis. Using these ideas a mathematical model is then derived that simulates the growth of the tissue layer as well as the cell distribution and make up of the extracellular matrix. The modelling predictions will then be compared to the experimental data. The notation used in this chapter will be independent of that that has been previously defined. To this extent all previously defined variables and parameters can be discounted.

This thesis will end with a brief summary of the results and conclusions of the work developed in each chapter; this is given in Chapter 6.

Chapter 2

Modelling the effects of metabolism on the growth of tumour spheroids

2.1 Introduction

Every year the leading British cancer charity, Cancer Research UK, spend over three hundred million pounds on cancer research. Yet in 2008 alone there was 156,000 deaths due to cancer and a positive diagnosis was made every two minutes [179]. On a worldwide scale over twelve million people were diagnosed with cancer in 2008 of which over seven million died [46]. The mortality rate for people diagnosed with cancer is falling, but with over two hundred known types of cancer there is obviously a lot of work still to be done.

Cancer develops due to mutations in the genes that affect cell division. The cell cycle determines whether a healthy cell is required to divide to aid the body in growth or regeneration. During this process there are various checkpoints that must be satisfied before the cell eventually reproduces. The mutation in a cancerous cell causes the cell to ignore the decisions made in the cell cycle and rapidly divide independent of the body's needs for more cells. A region of cells experiencing uncontrolled proliferation is known as a tumour. This produces a region of densely packed cells that demands a large amount of energy to survive. Thus in this region a large quantity of nutrients are consumed and a large amount of waste is produced. Whilst the diameter of the tumour is relatively small, nutrients will be transported to the cells by diffusion. Once a tumour has reached a certain size the cells in the outer regions will consume the nutrients before they are able to diffuse through to the inner regions. The cells in the inner region wills now be unable to obtain the necessary energy supply to continue proliferation. An *in vivo* tumour in this situation will become vascularised, forming new blood vessels to provide an enhanced transport mechanism and supply the tumour with the necessary nutri-

ents to continue growing. However in an *in vitro* tumour, the cells with limited nutrients will proliferate at a slower rate or potentially die.

The success of medical treatments such as radiotherapy and chemotherapy are dependent on the local micro-environment of cells [177] and yet the distribution of chemotherapeutic drugs inside a tumour is poorly understood [117, 118]. The tumour's micro-environment is determined by nutrient and waste consumption, production and transport. Therefore it is of interest to study how a group of cells will grow and how the concentrations of the chemical species residing inside tumours are affected by cellular consumption, production, transport and interactions between these components.

There is an extensive library of literature on the mathematical modelling of tumour growth. In main these modelling studies have concentrated on *in vitro* tumours in which there is a large amount of experimental data published. Modelling the growth of an *in vitro* tumour is simpler than modelling the equivalent growth *in vivo*. This is due to the controlled environment in which an *in vitro* experiments takes place in and the absence of effects such as vascularisation. One of the earliest and most influential papers in the area of tumour modelling was by Greenspan [68]. It introduced the concept of regional cell behaviour dependent on the concentration of a general growth limiting nutrient. Since then many approaches have been developed to model tumour growth. These have included such effects as the appearance of necrotic cores [78, 145, 146], the build up of stress [5, 110], cell migration and interaction within their local environment [6, 14, 143], as well as further investigation into the cell cycle state at which cells exist in different regions of the tumour [186]. The above discussion only refers to *in vitro* tumour growth. There has been some extensions of these models to *in vivo* tumours, for example the environmental differences and effects of vascularisation have been explored [15, 161]. For a more comprehensive review on mathematical modelling of tumour growth see recent review papers by Araujo and McElwain [8] or Roose *et al.* [151].

Existing mathematical models most commonly consider the growth of an *in vitro* tumour being controlled by the concentration of a single nutrient. The limiting species is generally thought to be either oxygen or glucose [68]. However in many single species mathematical models the model is simplified by considering a general species, normally referred to as 'nutrients'. Existing single species models are generally used to examine the behaviour and characteristics of a tumour, such as in [161, 186, 188]. However there have been limited attempts to model the growth of a tumour using a single species model and relate the results to experimental data, [122]. Similarly there have been few models presented examining the role of multiple species in metabolic processes within cells. The most advanced of this type of model is presented by Casciari *et al.* [24]. In this chapter we will present a multispecies model of a tumour growing *in vitro* that mirrors the concepts presented by Casciari *et al.* [24]. The model presented will develop a structure to study the growth behaviour of a multicellular tumour spheroid (MCTS)

for critically low concentrations of nutrients and at high concentrations of waste products. The different stages of the cell cycle and effects of mitosis, quiescence and necrosis shall be taken into account. The distribution of oxygen, glucose, carbon dioxide, lactic acid and pH within an avascular tumour will be modelled as well as a detailed investigation into the metabolic pathways from which cells obtain energy. In this model the relevant buffering reactions are included together with waste production by cells. In addition to the diffusive effects on nutrient movement, the effects of charge migration of ionic molecules are also incorporated. The results of the model will give a greater insight into what factors limit growth and what is important to include in a model of a MCTS. The model is reduces to a two species model in which oxygen and glucose are retained. A further reduction to a single species model is shown to be unrealistic.

This chapter will begin with a brief overview of the cell cycle before an in depth discussion of tumour growth and modelling. In particular we shall focus on how metabolic effects can alter the internal environment and growth of a tumour. Section 2.3 will then given a brief review of a multispecies model that has many underlying characteristics that we wish to build upon. The concepts of the tumour model presented in this thesis and the resulting modelling equations will be presented in Section 2.4. The model is solved and the results are given in Section 2.4.9. These results are then analysed in Section 2.5 and used to develop a simplified model of tumour growth that retains the same characteristics as the original model but in a reduced framework. The results of this simplified model are presented in Section 2.6. Finally an overall discussion of the models presented and areas to develop in the future is given in Section 2.7.

The cell cycle

A single cell will grow and divide into two daughter cells during a process known as the cell cycle. The cell cycle consists of four consecutive phases that typically take between eighteen to twenty-four hours to complete[1]. The first phase is known as the G_1 phase (Gap 1 phase). This phase begins immediately after the parent cell has divided into two daughter cells and is a period of growth where the cell increases in size. This typically takes approximately ten hours and is followed by the G_1 checkpoint, which confirms the cell is ready for DNA synthesis. Once the checkpoint is satisfied the cell enters the S (Synthesis) phase. The S phase is where the cell's DNA is replicated to form two identical sets, which will separate to form two daughter cells. This generally takes between five and six hours. The G_2 (Gap 2) phase follows the S phase and like the G_1 phase is a period of cell growth (approximately three to four hours).

[1]Cell cycle times are approximate times for tumour cells. The cell type and local environment of the cell will cause these times to vary.

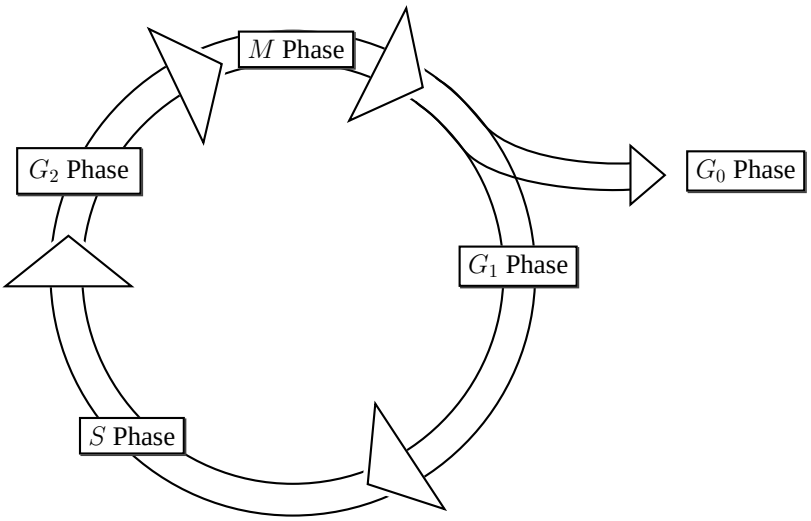

Figure 2.1: A schematic of the cell cycle showing the ordered phases.

By the end of this phase the cell must be large enough to divide into two cells. As in the first growth phase the G_2 phase is completed when the G_2 checkpoint is satisfied and the cell is deemed ready to enter the M (Mitosis) phase. The M phase is where the cell divides into two daughter cells. Firstly the two sets of chromosomes are separated and form two individual strands of DNA. This is followed by the splitting of the cell into two daughter cells. This phase typically takes two hours and completes the cell cycle. Due to cell signalling, a lack of nutrients or other environmental stimuli a cell may leave the cell cycle, typically at the G_1 checkpoint, and enter the G_0 phase. Here cells exist in a quiescent or inactive state where they are alive but not actively proliferating. Cells can exist in this phase until they are required to make new cells once again or until they are given the signal to die (apoptosis). The five phases of the cell cycle are graphically shown in Figure 2.1. For a more in depth review of the cell cycle the author suggests Widnell and Pfenninger [191] or Morgan [121].

All cells are affected by their local micro-environment and the concentration of surrounding nutrients. However a mutation in the DNA of a cancerous cells results in the cell neglecting any signals to stop dividing and will continue on the cell cycle until its surrounding environment prevents it.

The rate at which the cell cycle is completed is dependent on many factors. The most apparent of these is the concentrations of chemical species in the surrounding environment, as this determines how much energy the cell can assemble. Cells gain energy from respiration. This can occur in the presence of oxygen and glucose (aerobic) or purely in the presence of glucose (anaerobic). Therefore the concentration of oxygen and glucose is crucial in determining how much energy the cell can produce. As well as providing energy, respiration creates waste,

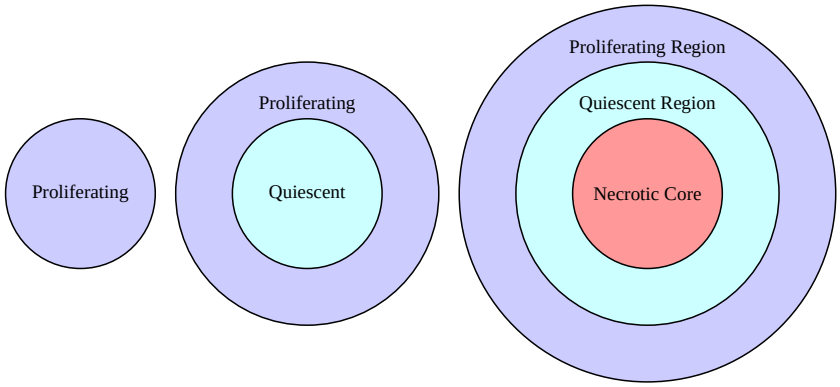

Figure 2.2: Sketch of a growing MCTS broken down into regions based on cell activity.

namely carbon dioxide, lactic acid and hydrogen. These can create a hostile local environment for cells and reduce the rate at which the cell cycle is completed.

2.2 Literature review of cell metabolism

Modelling the growth of a tumour is a highly complicated process. The controlled environment in which *in vitro* tumours are grown simplifies the experimental process, but biology is by no means an exact science and therefore there is still a lack of coherent and systematic data regarding the growth of tumours and the behaviour of cells in different micro-environments. Once the governing processes within a tumour have been established there are still a large number of species that can affect the growth of the tumour and therefore could be modelled. In this study we shall solely consider multicellular tumour spheroids. A MCTS is a small cluster of tumour cells, grown *in vitro* that have been found to create environments for cells that are very similar to those seen *in vivo*, and have therefore been exploited in examining tumour behaviour. As schematically shown in Figure 2.2 a MCTS has a simple structure that once fully developed can be broken down into three regions. The first is the proliferating region. The micro-environment here is conducive for proliferation and thus this region contains cells that are actively undergoing mitosis. Below a certain diameter, the whole tumour is contained within this region. In larger tumours, the proliferating region is found at the periphery and thus is also know as the proliferating rim. As the tumour grows the concentration and conditions within the MCTS change. At a certain size the conditions within the tumour will have changed such that the centre is ill-suited for cell proliferation. At this point the cells will leave the cell cycle, entering the G_0 phase, becoming inactive. Thus this region is know as the quiescent region. If the micro-environment within this region were to change, then these cells could restart the cell cycle and proliferate once more. Thus the quiescent and proliferating region is often collectively known as the viable rim. Further growth and decline in the environmental

conditions at the tumour core will cause the quiescent cells to die. Thus cells at the centre will begin to undergo necrosis, in what is known as the necrotic core. Once a cell is necrotic it will not be able to return to either a quiescent or proliferative state.

In this thesis MCTS are used as a simple system in which to determine the metabolic mechanisms and nutrient distributions within a growing tumour. The growth of a MCTS causes internal concentration gradients in essential nutrients and waste products. Single species models determine the rate of growth by the concentration of the single species. Multi species models show the interaction of multiple species with the tumour, showing how the environment inside a tumour develops and how the interaction of species limits growth. Casciari *et al.* [24] present such a model, focused on effects of metabolic reactions within cells and buffering reactions in the extra cellular space. Despite setting out to include all chemical and biological effects, the model Casciari *et al.* then neglect many chemical reactions and present a model that is critically dependent on the results of experimental data; taken from work by Casciari and Freyer [22, 50]. The aim of this work is to explain the experimental observations of a growing tumour. This will be done by modelling its growth using the chemical energy demands and characteristics of cells in changing conditions rather than relying on empirical fits to experimental data as in [24]. To do this an in depth understanding of metabolic activity for individual and groups of cells is required.

Consumption of nutrients

Cells obtain the energy they require to exist by consuming oxygen, glucose and amino acids which they acquire from their local extracellular environment. Therefore it is essential that a detailed understanding of the characteristics of the nutrient consumption by cells is obtained. There is a large literature available on the cellular consumption of both oxygen and glucose. There are two particular phenomena that are observed, these are known as the Pasteur and Crabtree effect. The Pasteur effect is characterised by cells that have a preference for aerobic respiration and only swith to anaerobic respiration when the local concentration of oxygen becomes limited. Cells governed by the Crabtree effect will have a preference for anaerobic respiration and will only switch to aerobic respiration when the local glucose concentration decreases below a critical level. The Crabtree effect coincides with the large body of work based on the Warburg hypothesis which stated that cancer cells rely on aerobic glycolysis and this alone can provide enough energy for cell proliferation. This has been widely discussed in literature and although it may be the case in some cell lines, it has been proven incorrect in others. Further information on the Pasteur and Crabtree is given in [35, 36, 193], whilst for further details on the Warburg effect and energy metabolism in cancer cells is presented in [66, 181, 185].

Care must be taken when making comparisons between sets of experimental data. Cell lines, spheroid structure and the local environment of a cell are just a selection of factors that can influence nutrient consumption and reaction rates. The cellular consumption of either oxygen or glucose is often derived by considering the MCTS as a whole. This simplifies the experimental procedure and subsequent analysis, but is limited in both its description of how individual cells behave and the behaviour of regions of cells. The reliance on diffusion as the transport mechanism for species within a MCTS will allow consumption by cells to restrict oxygen and glucose from reaching the centre of the spheroid. Therefore the the concentration of nutrients at the centre will be lower than the outer surface. The rate at which oxygen and glucose are consumed will be dependent on the preference of the cell line studied to undergo the Crabtree or Pasteur effect. Cells that are governed by the Pasteur effect will prioritise aerobic respiration and therefore as the size of a MCTS increases it is expected that the average oxygen consumption will decrease. During the same period it is expected that glucose consumption will increase, due to the increase in anaerobic respiration at the centre of the tumour. The onset of quiescent and necrotic regions, will create regions in which the demand for oxygen and glucose is lower. This makes interpretation of consumption rates based on entire MCTS volumes more complicated. The existence of quiescent and necrotic regions may explain the data presented by Freyer and Sutherland, [54], in which they report a linear decrease in both the rate of oxygen and glucose consumption by EMT6/Ro cells as the size of the MCTS increases. The decrease in the glucose consumption rate is unexpected but may suggest that cells belonging to this cell line quickly becoming quiescent in an absence of oxygen. The trend described by Freyer and Sutherland, [54], is verified over various cell lines for oxygen in [22, 57] and for glucose in [22, 183].

Experiments exploring consumption as a function of various species concentrations have also been reported. Freyer and Sutherland, in [54], published data regarding oxygen and glucose consumption, by exponentially growing EMT6/Ro tumour cells grown in monolayer cultures, as a function of oxygen and glucose concentrations. Oxygen consumption is shown to be constant over a range of oxygen concentrations. The consumption rate of glucose is reported to increase when the oxygen concentration decreases. This implies that EMT6/Ro cells are governed by the Pasteur effect and thus the rate of oxygen consumption would only decrease once there is insufficient oxygen available to consume. This full correlation cannot be verified however as data for oxygen consumption at low level concentration is not given. The relationship between the consumption rates of oxygen and glucose under changing glucose concentration is not so transparent. Glucose consumption is constant at varying glucose concentrations and even at low glucose concentrations no significant drop in consumption is seen. The rate of oxygen consumption is observed to rise at low glucose levels, which suggests aerobic respiration is being up regulated at low glucose levels, the Crabtree effect. These results are supported by Casciari [22] and Mueller-Klieser *et al.* [125] for EMT6/Ro cells.

Casciari [22] investigates the relationship between oxygen consumption and concentrations of oxygen, glucose and hydrogen (pH) in EMT6/Ro cells. The rate of oxygen consumption is shown to increase with oxygen concentration and decrease when the environment becomes more acidic. An increase in glucose concentration is shown to decrease the rate of oxygen consumption, and this Crabtree effect is shown to be consistent over a range of oxygen concentrations and pH. This contradicts other results for this cell line, which have predominately shown the characteristics of the Pasteur effect. Looking away from EMT6/Ro cells, to other cell lines, we see similar results. Bibby *et al.*, [12], study Bovine nucleus pulposus cells, reporting that the rate of oxygen consumption decreases as oxygen concentration lowers. Similarly Bibby *et al.* show that as the rate of glucose consumption decreases as glucose concentration drops. In 9L rat tumour cells, [78, 104] and V79 Chinese hamster lung tissue cells, [78], the rate of glucose consumption was shown to decrease as the glucose concentration lowered.

The behaviour of cells in different regions of EMT6/Ro tumour spheroids is considered in Freyer [51]. The viable rim of a MCTS is broken down into radial fractions and oxygen consumption rates for each region are given. This data shows that the cellular consumption rate decreases through a MCTS, from a maximum at the outer surface, into the necrotic core where consumption is negligible. Freyer, [52], confirms these findings, showing quiescent cells consume two to three times less oxygen than cells in the viable rim.

Lactic acid production and pH

Experimental literature tends to focus on the scarcity of nutrients as the reason for restrictive cell proliferation. Unlike most tissue, tumour cells can survive in highly acidic conditions [39]. However high concentrations of waste products still affect spheroid growth and the consumption rates of nutrients. At high oxygen concentration, aerobic respiration produces carbon dioxide and water. When oxygen levels reduce, anaerobic respiration takes over, and lactic acid is produced, as shown experimentally in [119, 120]. This will cause the local pH to decrease. Tannock *et al.* [172] explain how hydrogen is regulated in tumours and show the need for buffering reactions. Casciari [22, 24] presents data regarding EMT6/Ro tumour spheroids, suggesting that when pH drops below pH neutral, oxygen consumption will also drop at low glucose levels. However lactic acid is only expected to be produced when the concentration of oxygen is very low, so there is insufficient data to draw any definite conclusions.

Walenta *et al.* [183] show experimentally that a rise in the rate of glucose consumption increases the production of lactate. Bibby *et al.* [12], report that glucose and oxygen consumption decreases as pH drops and Mokhbi Soukane *et al.*, [120], show that at high lactate concentration, lactate production is low, suggesting the increase in pH is impeding the cells efficiency. Walenta *et al.* [184] observed that lactate concentration was high in necrotic zones. In these

necrotic zones energy production is known to be negligible, [183]. Therefore data suggests that lactate concentration, or equivalently pH, is a factor in determining when cells will become necrotic and as well as the rate of mitosis and onset of quiescence.

It should be noted that anaerobic respiration is not the only source of acid in a tumour. Helmlinger *et al.*, [74], propose bicarbonate as important element to include in determining the pH, as they observe a strong correlation between carbon dioxide production and the pH of their system.

Necrosis, proliferation and spheroid size

It has been observed that when a MCTS has grown sufficiently the centre of the spheroid will become necrotic. This is generally taken to be due to the deprivation of essential nutrients, [93, 171], and/or the local environment being unsuitable to support life, *e.g.* highly acidic. The tumour spheroid can thus be broken down into two distinct regions, the necrotic core and the viable rim. As shown schematically in Figure 2.2, the viable rim consists of cells which are actively proliferating as well as those existing in a quiescent state. Therefore the consumption rates and concentrations of nutrients and waste species, along with cell proliferation rates, will vary throughout the viable rim. Using experimental data from [51, 54] Jiang *et al.* [87] have derived metabolic rates for nutrient consumption and waste production for proliferating, quiescent and necrotic cells. Necrotic cells are inactive, but quiescent cells are reported to consume oxygen and glucose at under half the rate of proliferating cells. Coinciding with this, waste is produced at half the rate in quiescent cells compared to those that are actively proliferating. Freyer and Sutherland [56] investigated the relationship between the concentration of oxygen and glucose with the onset of necrosis in EMT6/Ro MCTS. They show that lowering oxygen and glucose concentrations decreases the outer diameter of the spheroid at which time necrosis is initiated. Notably oxygen is not clearly the dominant factor. Over an oxygen concentration range of 0.28mM to 0.07mM and at a high glucose concentration of 16.5mM, necrosis is first observed when the spheroid size becomes approximately five hundred microns in diameter. However a reduction in glucose concentration greatly reduces the critical size for initiation of a necrotic region, implying anaerobic respiration may be making up the deficit created by a lack of oxygen in the early cases.

Freyer and Sutherland [56] present data regarding the thickness of the viable rim for varying conditions and spheroid sizes. Care must be taken on interpretation of Figure 3 in [56] due to an error in labelling. The results, summarised in Table 2.1, show that for high glucose concentration the influence of oxygen is negligible. At high glucose concentration the viable rim size remains of constant thickness, in the order of 250μm. As glucose concentration drops, the viable rim size decreases. At low concentrations of oxygen and glucose the thickness of

the viable rim also decreases as the spheroid grows in size.

Mueller-Klieser [124] propose that the viable rim contains three zones. Firstly the outer peripheral, which will be well oxygenated and contains proliferating cells. Then a intermediate zone, that is also well oxygenated, but not to the same extent as the outer peripheral and thus quiescent. Thirdly a inner, hypoxic and therefore quiescent zone which may or may not become necrotic. This is consistent with data in Freyer [51] which publishes data for fractions radiating out from the centre. Freyer reports that in EMT6/Ro spheroids, the viable rim will be 223μm wide and within this region oxygen consumption rates, percentage of cells proliferating and average cell volume will all decrease as the distance from the spheroid periphery increases. A similar three zone model pre-dating [51] and [124] is presented by Tannock, [171] in which growth fractions and data on the position of cells in the cell cycle are given. Kunz *et al.* [93] publish data for a range of cell lines (Rat1, M1, Rat1-T1 and MR1) showing the the oxygen consumption rate through out different sized spheres. Not only does this data show the relative consumption rates in different zones, but gives the radial thickness of the hypoxic region and thus a guide to the thickness of the viable rim.

Between different cell lines the thickness of the viable rim and the way cells react to hypoxia differs. Mueller-Klieser, [124], reports that WiDr and MR1 spheroids can grow to significantly larger volumes before necrosis is observed. Mueller-Klieser introduces in [123] and expands in [124] the idea that spheroid cell lines can be distributed into one of three categories. Firstly spheroids that immediately become necrotic when the surrounding conditions becomes hypoxic. Secondly spheroids which can withstand hypoxia for a length of time before becoming necrotic; due to this resilience the viable rim will be larger in these spheroids. And lastly spheroids that see necrosis and then hypoxia. EMT6/Ro spheroids are an example of this latter behaviour. They are vulnerable to low oxygen concentrations and require a minimum concentration to survive. The viable rim for this case is relatively small.

In [55], Freyer and Sutherland look at the effects oxygen and glucose concentration have on the state of cells in the cell cycle and relate this to the size of the viable rim. The data shows that the percentage of cells in the S phase decreases with a decrease in either oxygen or glucose concentration, or with an increase in spheroid diameter. The latter is verified by Freyer *et al.* in [53]. The thickness of the viable rim is also shown to shrink as oxygen and glucose concentrations decrease, as well as during spheroid growth. Freyer and Sutherland fit formulas for the thickness of the proliferating layer as well as the growth fraction as functions of the spheroid diameter and percentage of cells in the S phase. The relationship between tumour conditions and the position of cells in the cell cycle is explored further in [55]. Data shows that as either spheroid diameter increases, or the concentration of either oxygen or glucose is reduced then the percentage of G1 cells will increase. Under the extreme conditions of low oxygen and glucose concentration and large spheroid diameter the fraction of G1 cells

Glucose concentration mol m^{-3}	Oxygen concentration, mol m^{-3} 0.07 Spheroid diameter μm	0.07 Viable rim thickness μm	0.28 Spheroid diameter μm	0.28 Viable rim thickness μm
0.8	375	60	344	109
	406	66	381	99
	541	47	566	99
	590	52	609	115
			793	117
			842	105
			1014	58
1.7	357	60	320	101
	498	78	369	93
	602	70	602	128
			652	120
			799	124
			848	130
			1045	85
5.5	363	66	467	202
	566	159	609	217
	627	144	609	186
	750	151	842	206
	824	126	1156	202
			1340	188
16.5	541	140	529	264
	590	264	615	252
	590	243	842	243
	799	249	891	249
	891	260	1094	221
			1402	237

Table 2.1: Data from Figure 3 in [56] showing the thickness of the viable rim for EMT6/Ro tumour spheroid grown in medium with various concentrations of oxygen, glucose. Oxygen and glucose concentrations specified for the surrounding medium

approaches one. S phase cells are also shown to decrease towards the centre of a spheroid, [52, 55]. This implies that for large tumours and at low nutrient concentrations, cells are mainly quiescent or necrotic with a relatively small number of cells proliferating at the spheroid periphery.

ATP production

The conditions in which cells become quiescent, undertake apoptosis or are forced to undergo necrosis vary. Hypoxia is generally taken to be a main factor influencing the state of cells, [171], but Mueller-Klieser stated explicitly that 'cell cycle arrest in multicellular spheroids is not a consequence of hypoxia or nutrient depletion' in [124] and therefore other factors must be involved. These may include the pH of the local environment, mechanical stresses applied to the cells or the loss of suppressor genes [39].

Hlatky *et al.*, [78], modelled necrosis based on the possible amount of energy, adenosine triphosphate (ATP), that cells could produce. Therefore in the absence of any extracellular influences, cells have a desired energy requirement from their surroundings. If this requirement is met then the cell will complete the cell cycle at a desired rate. If resources are not available to meet the energy requirement the cells will either stop proliferating, become quiescent or even die. Hlatky *et al.* [78] found that V79 cells from Chinese hamster lung tissue will become necrotic if the amount of ATP produced drops to half the level it was at under optimal conditions. This seems a logical way to model cell metabolism as it takes into account a variety of different factors. It still implies that cells will either be mitotic, quiescent or necrotic depending on the concentration of oxygen in its surrounding environment. However providing there is an adequate concentration of glucose it will allow anaerobic respiration to meet the rate of ATP production required for a cell to continue being mitotic or quiescent. Data regarding the concentration of glucose at the centre of a spheroid for a range of spheroid diameters is presented by Walenta *et al.* [183]. For MR1 and Rat1-T1 cells the glucose concentration at the centre of the spheroid is shown to decrease as spheroid size increases. However, the concentration never falls to zero. This implies that for these cell lines the rate of ATP production must be strictly greater than zero for a cell to survive.

Walenta *et al.*, [183], investigate ATP production and present data on the ATP distribution throughout a MCTS. A distinct reduction in ATP production was observed between the outer rim and the spheroid centre, as well as at spheroid centres over a range of increasing sphere diameters. In regions of proliferating cells ATP distribution was constant. From the work done in [183] we can conclude there is a direct link between cell death and ATP production as well as differing cell behaviour at differing ATP concentrations. Walenta *et al.* [183] and Richter *et al.*, [147] both state that apoptosis is an energy requiring process. Therefore a cell's ability

to produce ATP is an important influence in determining if the cell will die by apoptosis of necrosis. Richter *et al.* propose a cell stays alive whilst the ATP level is above an intermediate point. Whilst below this level, apoptosis occurs providing there remains enough ATP. If the ATP level drops below a critical level then the cells will die due to necrosis.

From a modelling prospective, including ATP requirement will allow the behaviour of glucose and oxygen to be strongly interdependent. It will allow the cell state and spheroid growth to be dependent on the requirements of ATP alone, rather than on individual species. The concepts and ideas will now be used to construct a multispecies mathematical model of a growing MCTS.

2.3 Review of Casciari's multispecies model

Casciari *et al.* [24] present a multispecies model of avascular tumour growth that accommodates the chemical species involved in aerobic and anaerobic respiration as well as those needed for buffering ionic species. These are oxygen (ox), glucose (gl), carbon dioxide (cd), lactate (la), hydrogen (hy), bicarbonate (bi), chlorine (ch) and sodium (so). As in [20, 21, 37, 65, 68, 87, 161, 186, 188] the concentration of a species is modelled using the diffusion-reaction equation. Casciari *et al.* choose to include the effects of charge migration. There are limitations of the model presented in [24] as well as doubts over the accuracy of the results presented. In particular these relate to the metabolite production terms and the expression for spheroid growth.

Using the chemical equations for aerobic respiration, anaerobic respiration and the relevant buffering reactions Casciari *et al.* write down a system of production terms. The rates of reaction for respiration are unknown and so Casciari *et al.* derive expressions for the consumption of oxygen and glucose by assuming Michaelis Menten kinetics and fitting to data given in [22][2]. These fitted expressions for oxygen and glucose are functions of the local concentration of oxygen, glucose and hydrogen and are subsequently used in the derivation of the production terms for the remaining species. The consumption rates of oxygen and glucose used by Casciari *et al.* are,

$$P_{ox} = -\rho_c \left(A_a + \frac{B_a}{C_{gl} C_{hy}^m} \right) \left(\frac{C_{ox}}{C_{ox} + k_{ma}} \right), \tag{2.1}$$

$$P_{gl} = -\rho_c \left(A_b + \frac{B_b}{C_{ox}} \right) \left(\frac{1}{C_{hy}^n} \right) \left(\frac{C_{gl}}{C_{gl} + k_{mb}} \right), \tag{2.2}$$

[2]Full details of the fitting process are given in [22], whilst the terms used in [24] are a simplified version of that shown in [22].

where C_{ox}, C_{gl} and C_{hy} are the local concentrations of oxygen, glucose and hydrogen respectively and A_a, B_a, A_b, B_b, m, n, k_{ma} and k_{mb} are constants that have been fitted to data given in [24]. Originally the production of each species is derived in the intracellular and extracellular space separately. Casciari *et al.* then simplify these expressions to give productions terms independent of being inside or outside the cells. In simplifying the original expressions certain effects of respiration are removed. The production terms used by Casciari *et al.* for carbon dioxide, lactic acid and hydrogen ions are,

$$P_{cd} = -k_f C_{cd} + k_r C_{bi} C_{hy}, \tag{2.3}$$

$$P_{la} = -2\left(P_{gl} - \frac{1}{6}P_{ox}\right), \tag{2.4}$$

$$P_{hy} = k_f C_{cd} - k_r C_{bi} C_{hy} - 2\left(P_{gl} - \frac{1}{6}P_{ox}\right) - P_{ox}, \tag{2.5}$$

where k_f and k_r are the forward and reverse reaction rates for the hydrogen buffering reaction and C_{bi} is the concentration of bicarbonate. The buffering regulates the acidity/alkaline of the tumour and is achieved by adding bicarbonate to the system. The production term used for bicarbonate was,

$$P_{bi} = k_f C_{cd} - k_r C_{bi} C_{hy} - P_{ox}. \tag{2.6}$$

Although it is noted that these are simplifications of the original expressions, there are still several irregularities in these production terms. Carbon dioxide is a product of aerobic respiration, yet there is no dependence on the consumption of oxygen in equation (2.3). Hydrogen is solely produced during anaerobic respiration yet there is an extra $-P_{ox}$ term included in equation (2.5). The production of bicarbonate should be determined by a mass balance of the buffering equation and thus a function of the concentration of hydrogen, carbon dioxide and bicarbonate. However equation (2.6) states that the production is produced at a rate that is influenced by the rate of oxygen consumption.

When either the concentration of oxygen or glucose fall below a critical level the expressions for production of oxygen and glucose were replaced by,

$$P_{ox} = -\rho_c\left(\phi_a - \beta_a C_{gl}^2\right)\frac{C_{ox}^2}{C_{ox}^2 + \zeta_a}\left(\frac{C_{gl}^2}{C_{gl}^2 + \zeta_b}\right), \tag{2.7}$$

$$P_{gl} = -\rho_c\left(\phi_b - \beta_b C_{ox}^2\right)\left(\frac{C_{gl}^2}{C_{gl}^2 + \zeta_b}\right). \tag{2.8}$$

in which ϕ_a, ϕ_b, β_a, β_b, ζ_a and ζ_b are constants defined in [24]. These new expressions neglect the effects of pH and assume that all species involved in respiration will behave with glucose Michaelis Menten kinetics. The reasons behind the production rates of oxygen and glucose

taking this form were never explained in either [24] or [22]. Thus we can only conclude that they are empirical.

Casciari *et al.* model the growth of a spheroid until the onset of necrosis. Experimental data for the doubling time of cells, found in [22] are used to fit an expression for the growth of the spheroid in which necrosis is not accounted for and in which cells in the absence of oxygen or glucose become quiescent. The expression given for growth in [24] assumes Michaelis-Menten behaviour due to oxygen and glucose and assumes cells are shed at a rate proportional to the surface area. The effects of pH are included, where the exponent is once again used as a fitting parameter. The final expression used by Casciari *et al.* in [24] is,

$$G\left(r,t\right) \;=\; K_o\, G1\left(\frac{C_{ox}}{C_{ox}+G2}\right)\left(\frac{C_{gl}}{C_{gl}+G3}\right)\left(\frac{1}{C_{hy}}\right)^{n_g}, \tag{2.9}$$

where G is the rate of growth of the spheroid, K_o is a growth constant for cells and $G1$, $G2$, $G3$ and n_g are constants that have been fitted to data. Although the expression may reflect the experimental data whilst oxygen and glucose are high, it gives little insight into what influences growth and the effects of low oxygen and glucose in different regions of the spheroid.

An absence of a complete set of parameters and data makes recreating the predictions of the model presented in [24] impossible. Similarly the model presented has a Neumann boundary condition to reflect the flux of species across the surface of the tumour. Other than for oxygen the results presented show no effects from this and imply a Dirichlet boundary condition was used in the numerical calculations in [24].

The results also highlight inaccuracies in the model, in that oxygen consumption has ceased at the tumour core, resulting in a central region absent of glucose but not hypoxic. This contradicts experimental data in [124, 125, 126]. These points must be addressed in any future multispecies model.

2.4 Tumour modelling: Full model

Using the ideas discussed in sections 2.2 and 2.3 we shall now present an alternative model of the microenvironment and growth of an *in vitro* MCTS. This model will consider a MCTS consisting of cells from the EMT6/Ro cell line and thus it will be assumed that the dominant metabolic pathway is respiration governed by the Pasteur effect. Therefore the chemical species considered in this model are oxygen (ox), glucose (gl), carbon dioxide (cd), hydrogen (hy) and lactate (la). Bicarbonate is added to the *in vitro* experiments as a buffer to regulate the pH of the tumour, preventing the tumour from becoming too acidic or alkaline [74, 172]. A high

concentration of chlorine (ch) and sodium (so) within the extracellular fluid will be assumed. Chlorine and sodium are spectator ions, that are not involved produced in any reactions, but are required as electron buffers so that the electrical charge in the tumour remains neutral.

The concentration, C_i, of each chemical species i in the tumour microenvironment is governed by conservation of mass. It shall be assumed that the tumour grows with spherical symmetry and therefore letting r represent radial distance from the origin and t time, the concentration of each species will be governed by,

$$\frac{\partial C_i}{\partial t} + \frac{1}{r^2}\frac{\partial}{\partial r}\left(r^2 N_i\right) = P_i, \tag{2.10}$$

where N_i is the flux $\left(\text{mol m}^{-2}\text{s}^{-1}\right)$ of species i in the outward radial direction and P_i is the production rate per unit volume. The production rates of each species are discussed in Section 2.4.5.

The transport mechanisms that govern the flux of each species will be advection, diffusion and charge migration. Advective transport will take place in the fluid surrounding the cells and is due to the spheroid growing. In this model we shall not consider the velocity of cells and the fluid separately, but instead implement an average velocity of the two, denoted by U and derived in Section 2.4.3. A detailed discussion of the appropriate expression for diffusion using homogenization techniques is given in Chapter 4. However in this model diffusion shall be given by Fick's law; the diffusion coefficients, D_i, for individual species are discussed in Section 2.4.1. Charge migration is included as a transport mechanism due to the high concentration of ionic species and thus presence of an electric field. As described by Newman and Thomas-Alyea [132] the electric field, $-\nabla\Phi$ can be multiplied by the charge per mole on a species to derive the force per mole. The average velocity of a species in the electrolyte when acted upon by a force of one Newton per mole is called the mobility. The force per mole multiplied by the mobility gives the migration velocity and this multiplied by the concentration of the chemical species gives the net flux due to charge migration. Thus the total flux for each species is given by,

$$N_i = C_i U - D_i \frac{\partial C_i}{\partial r} - z_i \mu_i F C_i \frac{\partial \Phi}{\partial r}, \tag{2.11}$$

in which z_i is the charge of species i, F is Faraday's constant and Φ is the electric potential respectively. As in [24, 64, 153] the mobility, μ_i, is taken to be related to diffusivity by the Nernst-Einstein equation,

$$\mu_i = \frac{D_i}{R_g T}, \tag{2.12}$$

where R_g is the ideal gas constant and T is the temperature in degrees kelvin.

Species	Concentration, C_{∞_i} mol m^{-3}	Ref.	Diffusivity, D_i m^2 s^{-1}	Ref.	Nsc [24]
Oxygen	0.21	[24]	$1.65{\cdot}10^{-9}$	[87]	3.061
Glucose	5.5	[24]	$1.1\ {\cdot}10^{-10}$	[23]	3.455
Carbon dioxide	1.295	[22]			3.108
Lactate	0				3.345
Hydrogen	$10^{-4.25}$	[24]			2.682
Bicarbonate	26.2	[164]			3.218
Chloride	122.6	[164]			3.124
Sodium	143.4	[164]			3.266

Table 2.2: Initial concentrations, diffusion coefficients and Sherwood coefficients for the chemical species. The Sherwood numbers N_{sh_i}, denote the rate of transfer of a species across the spheroid surface and are a function of the spheroid radius S such that $N_{sh_i} = 1{+}Nsc{\cdot}10^4{\cdot}S^{1.099}$.

2.4.1 Diffusion coefficients

Not all of the diffusion coefficients for chemical species within a cellular region are known. Thus we must use known data to derived diffusion coefficients for the remaining species. In [170], Swabb *et al.* determine an empirical relationship between a species molecular weight and its diffusion coefficient. This relationship can be used to derive an unknown diffusion coefficient using the species molecular weight and the molecular weight and diffusion coefficient of a species with a similar molecular size. This is done by using the empirical equation,

$$D_i \;=\; D_j \left(\frac{MW_j}{MW_i}\right)^{\frac{3}{4}}, \tag{2.13}$$

where D_j and MW_j are the diffusion coefficient and molecular weight of a known species and D_i and MW_i are diffusion coefficient and molecular weight of the unknown species.

Oxygen, carbon dioxide, bicarbonate and hydrogen are of a similar molecular size and are all capable of diffusing across a cell membrane. Glucose, lactate, chloride and sodium are also of a similar molecular size to each other and are unable to diffuse across a cell membrane. Therefore taking diffusion coefficients of oxygen and glucose from the literature, given in Table 2.2, equation (2.13) can be used to calculate the diffusion coefficients for the remaining species. A schematic of the chemical species diffusing into the MCTS is shown in Figure 2.3.

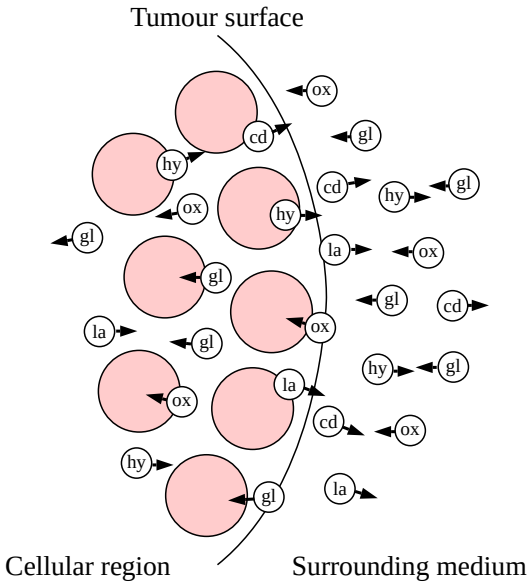

Figure 2.3: Schematic of the diffusion of nutrients and waste products. Nutrients diffuse into the tumour from the surrounding medium and are consumed by the cells, whilst waste products are synthesized inside the tumour and diffuse out.

2.4.2 Charge migration

Transport due to charge migration is dependent on the gradient of the electric potential. This can be derived by studying the conditions within the tumour spheroid. In the extracellular medium the electric field can be modelled using Maxwell's equations. We assume that the medium is homogeneous, isotropic and that the time scales in which Maxwell's equations occur are significantly smaller than those in which a tumour reacts. By using the dielectric constant for cells given in [91], we calculate the Debye length to be of order 10^{-9}m, which is much smaller than the other lengths scales associated with the tumour model. Therefore, as described by Newman and Thomas-Alyea in [132], a small deviation from electro-neutrality would require a large electric force, the size of which is unrealistic in a tumour spheroid. Therefore the tumour can be considered to be charge neutral at any point and we impose,

$$\sum_{i=1}^{n} z_i \, C_i \; = \; 0. \tag{2.14}$$

Charge can not be created nor destroyed, therefore,

$$\sum_{i=1}^{n} z_i \, P_i \; = \; 0. \tag{2.15}$$

Multiplying equation (2.10) by the corresponding charge of the species, z_i, and summing over all components gives,

$$\frac{\partial}{\partial t}\left(\sum_{i=1}^{n} z_i\, C_i\right) + \frac{1}{r^2}\,\frac{\partial}{\partial r}\left(r^2 \sum_{i=1}^{n} z_i\, N_i\right) = \sum_{i=1}^{n} z_i\, P_i. \tag{2.16}$$

Substituting equations (2.14) and (2.15) into equation (2.16) gives,

$$\frac{1}{r^2}\,\frac{\partial}{\partial r}\left(r^2 \sum_{i=1}^{n} z_i\, N_i\right) = 0. \tag{2.17}$$

This must hold throughout the MCTS, therefore to be satisfied at the origin,

$$\sum_{i=1}^{n} z_i\, N_i = 0, \tag{2.18}$$

which imposes that there is no net current through the tumour.

Substituting equations (2.11) and (2.12) into equation (2.18) gives,

$$U \sum_{i=1}^{n} z_i\, C_i - \sum_{i=1}^{n} z_i\, D_i \frac{\partial C_i}{\partial r} - \frac{F}{R_g T}\,\frac{\partial \Phi}{\partial r} \sum_{i=1}^{n} z_i\, D_i\, C_i = 0. \tag{2.19}$$

Rearranging equation (2.19) and imposing equation (2.14) gives an equation for the electrical potential gradient,

$$\frac{\partial \Phi}{\partial r} = -\frac{R_g T}{F}\left(\frac{\sum_{k=1}^{n} z_k\, D_k\, \frac{\partial C_k}{\partial r}}{\sum_{k=1}^{n} z_k^2\, D_k\, C_k}\right). \tag{2.20}$$

Equation (2.14) is a linear combination of the equations governing conservation of ionic species. Thus we cal replace the equation for conservation of sodium by equation (2.14).

2.4.3 Conservation of cells

Within the spheroid we require that cells are conserved. Thus if ρ is the density of cells we impose,

$$\frac{\partial \rho}{\partial t} + \frac{1}{r^2}\,\frac{\partial}{\partial r}\left(r^2\, \rho\, U\right) = \rho\, g, \tag{2.21}$$

where g is the net rate of proliferation. In the absence of any additional forces and neglecting the change in cell sizes discussed in Section 2.2, it will be assumed that cells will spread out such that the cell density will remain constant, thus

$$\frac{1}{r^2}\,\frac{\partial}{\partial r}\left(r^2\, U\right) = g, \tag{2.22}$$

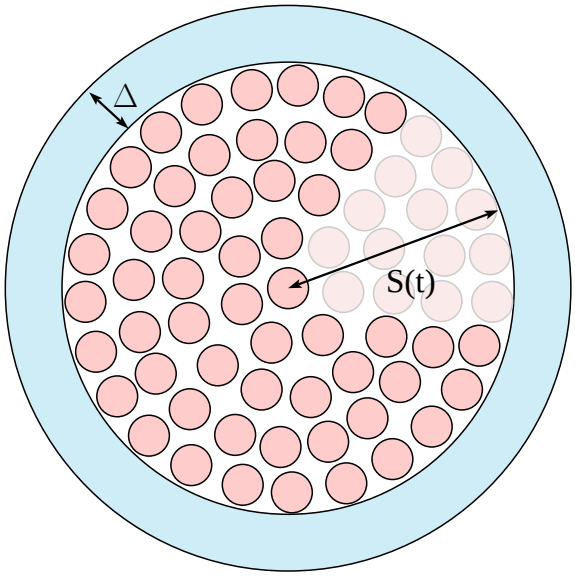

Figure 2.4: A schematic of the boundary layer that surrounds the tumour spheroid. The size of the tumour is denoted by $S(t)$, whilst the boundary layer is of size Δ.

The net rate of proliferation will be determined by the local concentration of metabolic species and will be discussed in Section 2.4.6.

2.4.4 Initial and boundary conditions

To complete the model we require initial and boundary conditions for equation (2.10), governing the concentration of each species and for equation (2.22), governing the velocity of the fluid.

Initially the concentration of each species will be set equal to that found in a typical culture medium used for growing *in vitro* tumours, denoted by C_{∞_i}. The medium considered will be Basal Medium Eagle and initial concentrations of each species are given in Table 2.2. The initial size of the spheroid will be taken to be that of a single cell.

The spherical shape of the tumour implies that the centre is stationary and thus there is zero cell velocity at the centre. Spherical symmetry also demands that there is no flux of species at the centre.

MCTS are commonly grown in medium that is replaced at regular intervals; commonly one to two days. The frequency that the medium is replaced and the degree of mixing that the culture system experiences will have a large effect on the transfer of nutrients from the outer medium into the tumour spheroid. We shall therefore consider a region surrounding the

tumour, through which the nutrients will be able to diffuse. The thickness of this region will be denoted by Δ and the concentration at the outer surface will be constant, denoted by C_{∞_i}. The advantage of this approach is that by changing the size of Δ we can study the effects of mixing. Infinite Δ would suggest that the MCTS is grown in a stationary fluid that is not replaced during the experiment. Whilst taking the limit as Δ tends to zero would simulate a MCTS grown in a well mixed outer medium. A schematic of this setup is given in Figure 2.4.

In the region surrounding the tumour we shall consider nutrient transport to be only the result of diffusion. The lack of waste production means we shall simplify the transport equation in the outer region by neglecting the effects of charge migration. The absence of cells in the boundary layer will have an effect on the diffusion coefficients of the nutrients, thus the diffusions coefficient in the boundary layer will be denoted by $D_{i_{out}}$. For species that can diffuse through a cell membrane, as discussed in Section 2.4.1, $D_{i_{out}}$ will equal D_i. For those that can not $D_{i_{out}}$ will be derived by dividing the diffusion coefficients used inside the tumour by the volume fraction of cells inside the tumour. To leading order the concentration of each species inside the boundary layer can be modelled by,

$$\frac{1}{r^2}\frac{\partial}{\partial r}\left(r^2 D_{i_{out}}\frac{\partial C_i}{\partial r}\right) = 0 \quad \text{for } r \in (S\,,\, S+\Delta)\,. \tag{2.23}$$

Equation (2.23) can be solved with continuity of species concentration and continuity of flux at the surface of the tumour and $C_i = C_{\infty_i}$ at $r = S + \Delta$, where C_{∞_i} is the concentration of species i in the original culture medium. This results in a flux condition at the tumour surface such that,

$$r^2 N_i = D_{i_{out}}\,\frac{S\,(S+\Delta)}{\Delta}\,(C_i - C_{\infty_i}) \quad \text{at } r = S(t), \tag{2.24}$$

An alternative interpretation to the boundary layer model, as proposed above, is that it simulates the resistance of nutrients as they cross from the external medium into the tumour spheroid. Values of these mass transfer coefficients, Sherwood numbers, are derived and given in [24]. As a first approximation we shall implement these mass transfer coefficients such that,

$$r^2 N_i = D_{i_{out}}\,S\,N_{sh_i}\,(C_i - C_{\infty_i}) \quad \text{at } r = S(t), \tag{2.25}$$

where N_{sh_i} is the Sherwood number for species i. Later in the chapter we shall review this approximation and discuss the effects of a well mixed and stationary boundary fluid. The values for C_{∞_i} and N_{sh_i} for each species are given in Table 2.2.

The effects of cell shedding from the tumour surface will be neglected, as discussed in [96, 187], thus the outer surface of the tumour will move with the cells on the surface and hence the kinematic condition is,

$$\frac{dS}{dt} = U \quad \text{at } r = S(t), \tag{2.26}$$

where U is defined by equation (2.22).

2.4.5 Production terms

We shall now derive the production rates for each chemical species using the ideas discussed in Section 2.2. As stated at the start of Section 2.4, this model shall consider a MCTS in which respiration governed by the Pasteur effect is taken to be the dominant metabolic pathway. Therefore the chemical reactions for aerobic and anaerobic respiration must be considered. Along with respiration the buffering of hydrogen to regulate the pH within the MCTS is included and thus the relevant chemical reactions for this must also be studied. However we shall firstly look at how cells utilise their local environment to generate the energy they require by means of respiration.

Metabolic reactions

Cells that are characterised by the Pasteur effect will aim to meet their energy needs by aerobic respiration. However if their is an insufficient supply of oxygen in their local environment, cells will turn to anaerobic respiration. Therefore this model must accommodate aerobic respiration, anaerobic respiration and a transfer between the two when the concentration of oxygen within a cells local environment falls below a critical level. The energy created by respiration is defined in terms of the concentration of ATP. The chemical equations for aerobic and anaerobic respiration, including ATP production, are,

$$\mathrm{C_6H_{12}O_6} + 6\mathrm{O_2} + 38\,\mathrm{ADP} \xrightarrow{R_{aero}} 6\mathrm{H_2O} + 6\mathrm{CO_2} + 38\,\mathrm{ATP}, \tag{2.27}$$

$$\mathrm{C_6H_{12}O_6} + 2\,\mathrm{ADP} \xrightarrow{R_{an}} 2\mathrm{C_3H_5O_3^-} + 2\mathrm{H^+} + 2\,\mathrm{ATP}, \tag{2.28}$$

where R_{aero} and R_{an} are the maximum rates of reaction for aerobic and anaerobic respiration. ADP is a nucleotide required for ATP synthesis and is assumed to be in plentiful supply.

Using equations (2.27) and (2.28) we can infer that the maximum rate of production for oxygen and glucose, denoted by P_{ox}^{max} and P_{gl}^{max}, due to respiration are,

$$P_{ox}^{max} = -6\,R_{aero}\,C_{gl}\,C_{ox}^6, \tag{2.29}$$

$$P_{gl}^{max} = -R_{aero}\,C_{gl}\,C_{ox}^6 - R_{an}\,C_{gl}. \tag{2.30}$$

The maximum rates for oxygen and glucose consumption, R_{ox} and R_{gl} are given by Freyer and Sutherland [54]. From these the reaction rates R_{aero} and R_{an} can be deduced. However the resulting maximum production rates are highly dependent on the concentration of oxygen

due to the large exponent in equation (2.29). This results in oxygen consumption becoming negligible well before the oxygen concentration becomes as low as is seen experimentally. Therefore, by assuming Michaelis-Menten kinetics, we shall replace the expressions given in equations (2.29) and (2.30) by,

$$P_{ox}^{max} = \rho R_{ox} \frac{C_{ox}}{C_{ox} + k_{ox}} \quad \text{and} \quad P_{gl}^{max} = \rho R_{gl} \frac{C_{gl}}{C_{gl} + k_{gl}}, \tag{2.31}$$

where ρ is the density of cells and the Michaelis constant k_{ox} is set as the concentration of oxygen defined as hypoxia. The Michaelis constants k_{ox} and k_{gl} are discussed further in Section 2.4.8.

We shall assume a cell will only create the energy that it needs. Thus the effective rates for respiration will be dependent on whether the cell is either proliferative, quiescent or necrotic. We shall assume that cells can derive the concentrations of oxygen and glucose in their local environment and thus determine the maximum amount of ATP that can be produced. The maximum production rate of ATP, P_{atp}^{max}, is simply a linear combination of the maximum that can be produced during aerobic and anaerobic respiration and can be represented by,

$$P_{atp}^{max} = -\frac{38}{6} P_{ox}^{max} - 2 P_{gl}^{max}. \tag{2.32}$$

In a plentiful supply of oxygen and glucose cells will aim to produce a high level of ATP, thus enabling the cell to undergo mitosis. As the concentration of oxygen or glucose restricts ATP production the cell will be forced to down regulate its rate of ATP production and in turn become quiescent and then necrotic. Therefore the desired production of ATP is dependent on the cells local environment and the production rates of oxygen and glucose, P_{ox} and P_{gl}. We shall denote the rate of ATP production demanded by mitotic cells shall by $Q_q + Q_m$, for quiescent cells by Q_q and we shall assume that cells undergoing necrosis demand no ATP.

The potential rate of ATP production thus determines the demanded rate of ATP production P_{atp}. If the maximum rate of ATP production, P_{atp}^{max} is greater than the required rate for mitosis, $Q_q + Q_m$, then the cells will produce ATP at this rate. If this rate can not be met, but the maximum ATP production rate is greater than required rate for a cell to stay quiescent, Q_q, then the ATP production rate will equal Q_q. Below this the ATP production rate is inadequate for a cell to stay quiescence and thus cell will become necrotic, demanding no ATP to be produced. Mathematically this sets P_{atp} such that,

$$P_{atp} = \begin{cases} Q_m + Q_q & \text{if} \quad Q_m + Qq < P_{atp}^{max}, \\ Q_q & \text{if} \quad Q_q < P_{atp}^{max} < Q_m + Q_q, \\ 0 & \text{if} \quad P_{atp}^{max} < Q_q. \end{cases} \tag{2.33}$$

If aerobic respiration can meet the desired ATP production rate required by cells, oxygen will be consumed at the appropriate rate. However if the rate of aerobic respiration is insufficient to meet the ATP demand then anaerobic respiration will meet the surplus and oxygen will be consumed at the maximum rate that is possible. Thus oxygen production will be given by,

$$P_{ox} = -\min\left(\frac{6}{38}\,P_{atp}\,,\,P_{ox}^{max}\right). \tag{2.34}$$

ATP is produced due to the consumption of oxygen and glucose and thus the production rate must be met such that,

$$P_{atp} \;=\; -\frac{38}{6}P_{ox} \;-\; 2\left(P_{gl} \;-\; \frac{1}{6}\,P_{ox}\right), \tag{2.35}$$

where P_{atp} has been determined by a mass balance of equations (2.27) and (2.28). P_{atp} is already defined by equation (2.33), therefore we rearrange equation (2.35) to determine the glucose production. This gives,

$$P_{gl} \;=\; \frac{1}{6}\,P_{ox} \;-\; \frac{1}{2}\left(P_{atp} \;+\; \frac{38}{6}\,P_{ox}\right). \tag{2.36}$$

There is no need to set glucose production as the minimum of the demanded rate and possible rate as this is accommodated for in equation (2.33). Using equations (2.27) and (2.28) the contribution of respiration to the production of carbon dioxide, lactate and hydrogen can be derived in terms of oxygen and glucose production such that,

$$P_{cd} \;=\; -\,P_{ox}, \tag{2.37}$$

$$P_{la} \;=\; -2\left(P_{gl} - \frac{1}{6}P_{ox}\right), \tag{2.38}$$

$$P_{hy} \;=\; -2\left(P_{gl} - \frac{1}{6}P_{ox}\right). \tag{2.39}$$

Buffering reactions

We shall now consider the buffering reactions. Although there are many different chemicals that buffer the pH in MCTSs, carbon dioxide and bicarbonate are taken to be the most effective. For a buffer to have maximal capacity, *i.e.* be most effective, the acidity dissociation constant should be as close as possible to the pH of the system. To verify that these species

[3]The consumption rates of oxygen and glucose given by Freyer and Sutherland [54] are $8.3 \cdot 10^{-17}$ and $5.2 \cdot 10^{-16}$ respectively. The values R_{ox} and R_{gl}, given in Table 2.3, have been multiplied by $(1 + k_{ox}/C_{\infty_{ox}})$ and $\left(1 + k_{gl}/C_{\infty_{gl}}\right)$ so that the initial oxygen and glucose production rates agree with [54].

Parameter		Value	Units	Ref.
ATP production mitosis	$Q_q + Q_m$	$8.58 \cdot 10^{-16}$	mol cell^{-1} s^{-1}	[54]
Cell density	ρ	$2.01 \cdot 10^{14}$	cell m^{-3}	[24]
Buffering reaction rate	k_f	0.145	s^{-1}	[63]
Buffering reaction rate	k_r	$1.73 \cdot 10^{2}$	mol^{-1} m^3 s^{-1}	[63]
Glucose consumption rate	R_{gl} [3]	$7.69 \cdot 10^{-16}$	mol cell^{-1} s^{-1}	[54]
Michaelis constant oxygen	k_{ox}	$1.32 \cdot 10^{-2}$	mol m^{-3}	[79]
Oxygen consumption rate	R_{ox}	$8.82 \cdot 10^{-17}$	mol cell^{-1} s^{-1}	[54]
Rate of mitosis	K_M	$1.48 \cdot 10^{-5}$	s^{-1}	[97]
Temperature	T	310	kelvin	

Table 2.3: Table of parameters given in the literature for the full model.

are the appropriate buffers for this system, the interaction of carbon dioxide, hydrogen and bicarbonate will be explained in more depth.

The pH of an aqueous solution is strictly the concentration of hydronium, H_3O^+, rather than hydrogen ions, H^+. Therefore the full chemical buffering equation of hydrogen by carbon dioxide and bicarbonate, HCO_3^-, including the intermediate steps involving carbonic acid, H_2CO_3, is,

$$CO_2 + 2\,H_2O \underset{k_{-1}}{\overset{k_1}{\rightleftharpoons}} H_2CO_3 + H_2O \underset{k_{-2}}{\overset{k_2}{\rightleftharpoons}} H_3O^+ + HCO_3^-\,, \tag{2.40}$$

where k_1 and k_{-1} are the hydration and dehydration rates and k_2 and k_{-2} are the forward and reverse ionization rates. To simplify the analysis the solution shall be taken to be well mixed and thus spatial variations can be neglected. Using square brackets to represent the overall concentration of a species, the dimensional mass balance equations for this reaction are,

$$\frac{d\,[CO_2]}{dt} \;=\; k_{-1}\,[H_2CO_3]\,[H_2O] \;-\; k_1\,[H_2O]^2\,[CO_2]\,, \tag{2.41}$$

$$\frac{d\left[H_3O^+\right]}{dt} \;=\; k_2\,[H_2CO_3]\,[H_2O] \;-\; k_{-2}\left[H_3O^+\right]\left[HCO_3^-\right]. \tag{2.42}$$

To highlight the rates at which each reaction takes place equations (2.41) and (2.42) are nondimensionalised. The concentration of water is significantly larger than that of the other reactants. It is therefore convention to take the concentration of water to be constant and include it in the hydration rate, such that,

$$[H_2O] \;=\; \overline{H_2O} \quad \text{and} \quad \overline{k_1} \;=\; k_1\left(\overline{H_2O}\right)^2. \tag{2.43}$$

where an over bar represents a constants a constant concentration and a hat will represent a nondimensional variable. Time is scaled using the dehydration rate k_{-1}, as this is believed to

be the slower reaction. Thus,

$$t \;=\; \left(\overline{k_1}\right)^{-1}\,\widehat{t}. \tag{2.44}$$

The remaining species are scaled using typical concentrations found in medium surrounding cells;

$$[\mathrm{CO_2}] \;=\; \overline{\mathrm{CO_2}}\,\left[\widehat{\mathrm{CO_2}}\right], \quad [\mathrm{H_2CO_3}] \;=\; \overline{\mathrm{H_2CO_3}}\,\left[\widehat{\mathrm{H_2CO_3}}\right], \tag{2.45}$$

$$\left[\mathrm{H_3O^+}\right] \;=\; \overline{\mathrm{H_3O}}\,\left[\widehat{\mathrm{H_3O^+}}\right], \quad \left[\mathrm{HCO_3}^-\right] \;=\; \overline{\mathrm{HCO_3}}\,\left[\widehat{\mathrm{HCO_3}^-}\right]. \tag{2.46}$$

Thus the non dimensional equations, without the hats, are,

$$\overline{k_1}\,\overline{\mathrm{CO_2}}\,\frac{\partial\,[\mathrm{CO_2}]}{\partial t} \;=\; k_{-1}\overline{\mathrm{H_2OH_2CO_3}}\,[\mathrm{H_2CO_3}] - \overline{k_1}\,\overline{\mathrm{CO_2}}\,[\mathrm{CO_2}]\,, \tag{2.47}$$

$$\overline{k_1}\,\overline{\mathrm{H_3O}}\,\frac{\partial\left[\mathrm{H_3O^+}\right]}{\partial t} \;=\; k_2\overline{\mathrm{H_2CO_3H_2O}}\,[\mathrm{H_2CO_3}] - k_{-2}\overline{\mathrm{H_3O}}\,\overline{\mathrm{HCO_3}}\,\left[\mathrm{H_3O^+}\right]\left[\mathrm{HCO_3^-}\right]. \tag{2.48}$$

The hydration and dehydration rates, $\overline{k_1}$ and k_{-1}, along with the ratio of the forward and reverse ionisation rates, k_2:k_{-2}, are given by Garg and Maren [63]. Garg and Maren, [63], also state that the dissociation of carbonic acid to hydrogen and bicarbonate is much faster than the hydration of carbon dioxide, thus ,

$$k_{-2} >> k_2 >> \overline{k_1}. \tag{2.49}$$

The time derivative in equation (2.48) is therefore taken to be negligible. The resulting equation,

$$\overline{\mathrm{H_2CO_3}}\,[\mathrm{H_2CO_3}] \;=\; \frac{k_{-2}}{k_2}\,\overline{\mathrm{H_3O}}\,\overline{\mathrm{HCO_3}}\,\left[\mathrm{H_3O^+}\right]\left[\mathrm{HCO_3^-}\right], \tag{2.50}$$

can then be substituted into equation (2.47) to give,

$$\overline{k_1}\,\overline{\mathrm{CO_2}}\,\frac{\partial\,[\mathrm{CO_2}]}{\partial t} \;=\; \frac{k_{-1}k_{-2}}{k_2}\,\overline{\mathrm{H_3O}}\,\overline{\mathrm{HCO_3}}\,\left[\mathrm{H_3O^+}\right]\left[\mathrm{HCO_3^-}\right] \;-\; \overline{k_1}\,\overline{\mathrm{CO_2}}\,[\mathrm{CO_2}]\,. \tag{2.51}$$

This implies that the effective reaction can be written as

$$\mathrm{CO_2} + 2\,\mathrm{H_2O} \underset{k_r}{\overset{k_f}{\rightleftharpoons}} \mathrm{H_3O^+} + \mathrm{HCO_3^-}, \tag{2.52}$$

where by the forward and reverse reaction rates are defined by,

$$k_f \;=\; k_1 \quad \text{and} \quad k_r \;=\; \frac{k_{-1}k_{-2}}{k_2}. \tag{2.53}$$

Numerical values for these expressions can be found using data in [63] and are given in Table 2.3.

The acid dissociation constant, K_a, is a measure of the relative strength of an acid and is calculated as the ratio of concentration of the products to the concentration of the original acid. Therefore the dissociation constant of carbonic acid is,

$$K_a = \frac{\left[HCO_3^-\right]\left[H_3O^+\right]}{[H_2CO_3]}. \tag{2.54}$$

A buffer is most effective when its pK_a is equal to the pH of the system, where

$$pK_a = -\log_{10}(K_a). \tag{2.55}$$

The pK_a of carbonic acid is given by David [40] to be 6.35. The pH of a tumour is know to be in the range 6.9 - 7, [131, 172], therefore carbon dioxide and bicarbonate will act as efficient buffers in this system.

Expressions for the production of carbon dioxide, bicarbonate and hydrogen[4] as a consequence of the buffering reaction in equation (2.52) can now be derived. These are,

$$P_{cd} = -k_f C_{cd} + k_r C_{bi} C_{hy}, \tag{2.56}$$

$$P_{hy} = k_f C_{cd} - k_r C_{bi} C_{hy}, \tag{2.57}$$

$$P_{bi} = k_f C_{cd} - k_r C_{bi} C_{hy}. \tag{2.58}$$

Chlorine and sodium are both spectator ions and so are not involved in any reactions.

The full system of production terms are given by,

$$P_{ox} = -\min\left(\frac{6}{38}P_{atp}\,,\,P_{ox}^{max}\right), \tag{2.59}$$

$$P_{gl} = \frac{1}{6}P_{ox} - \frac{1}{2}\left(P_{atp} + \frac{6}{38}P_{ox}\right), \tag{2.60}$$

$$P_{cd} = -P_{ox} + k_r C_{bi} C_{hy} - k_f C_{cd}, \tag{2.61}$$

$$P_{la} = -2\left(P_{gl} - \frac{1}{6}P_{ox}\right), \tag{2.62}$$

$$P_{hy} = -2\left(P_{gl} - \frac{1}{6}P_{ox}\right) - k_r C_{bi} C_{hy} + k_f C_{cd}, \tag{2.63}$$

$$P_{bi} = k_f C_{cd} - k_r C_{bi} C_{hy}, \tag{2.64}$$

$$P_{ch} = 0. \tag{2.65}$$

[4]For simplicity, in the remainder of this chapter the local pH of the tumour will be referred to as $\log_{10}$ of the concentration of hydrogen rather than hydronium.

The production terms stated above have been derived from the chemical reactions for aerobic respiration, anaerobic respiration and the buffering of hydrogen. Unlike those presented by Casciari in [24] and summarised in equations (2.1) to (2.6) of Section 2.3, no reactions have been neglected, nor have the production terms been simply fitted to data. It is hoped that the more transparent nature of these terms will provide a better understanding of how the conditions within a MCTS develop whilst modelling the data as well as those given in [24].

2.4.6 Growth

We shall now consider how the net rate of proliferation affects the growth of the tumour spheroid. Mechanical forces will be neglected in this model for growth as will the effects of cell shedding. Thus we shall only consider growth to be a function of the concentration of the chemical species within the tumour spheroid.

As described in Section 2.4.5 when a cell's local environment does not restrict its production of ATP, the cell will consume oxygen and glucose at a given rate and use the energy produced to undergo mitosis. Once the local oxygen and glucose concentrations fall below a critical level, cells will reduce their requirement for ATP and become quiescent. As oxygen and glucose concentrations reduce further cells will become necrotic. Therefore the net rate of proliferation must reflect the production of ATP within these regions. In the mitotic region, the maximum rate of mitosis will be denoted by K_M. Although in this region the concentration of oxygen and glucose will be high there will be gradients in both concentrations and this is likely to affect the rate of mitosis. This will be reflected in the proliferation rate by multiplying the maximum rate of mitosis by Michaelis Menten expressions for both oxygen and glucose. In the quiescent region cells are inactive. Therefore there is no proliferation nor necrosis and there will be no growth within this region. In the necrotic region we shall assume that the death rate of cells can be taken to be constant, K_{Ne}. These conditions impose that,

$$g = \begin{cases} K_M \frac{C_{ox}}{C_{ox}+k_{ox}} \frac{C_{gl}}{C_{gl}+k_{gl}} & \text{if} \quad Q_m + Qq < P_{atp}^{max}, \\ 0 & \text{if} \quad Q_q < P_{atp}^{max} < Q_m + Q_q, \\ -K_{Ne} & \text{if} \quad P_{atp}^{max} < Q_q, \end{cases} \tag{2.66}$$

where the Michaelis constant k_{ox} is as introduced in Section 2.4.5 and k_{gl} is fitted to data, as discussed in Section 2.4.8. We assumed in Section 2.4.3 that the cell density, ρ, in the tumour will be constant. Therefore in the necrotic region, where growth is negative, dying cells will be replaced by cells, pushed in from the outer regions. The transport of the debris left by necrotic cells out of the tumour will not be considered in this model.

Casciari *et al.* in [24] include the adverse effect of waste production on proliferation. However

the manner in which they do so is complicated and thus the relationship between proliferation and the concentration of hydrogen is hard to establish from their model. At this stage it is not clear how large the relative effects of waste production are on the net rate of proliferation and the rate of necrosis. Thus for simplicity they have been neglected in this model and this decision will be reviewed in Section 2.5.

2.4.7 Summary of modelling equations

The full system of modelling are,

$$\frac{\partial C_i}{\partial t} + \frac{1}{r^2}\frac{\partial}{\partial r}\left(r^2\left(C_i U - D_i\left(\frac{\partial C_i}{\partial r} + \frac{z_i\,F\,C_i}{R_g\,T}\frac{\partial \Phi}{\partial r}\right)\right)\right) = P_i, \tag{2.67}$$

$$\frac{\partial \Phi}{\partial r} = -\frac{R_g\,T}{F}\left(\frac{\sum_{k=1}^{n} z_k\,D_k\,\frac{\partial C_k}{\partial r}}{\sum_{k=1}^{n} z_k^2\,D_k\,C_k}\right), \tag{2.68}$$

$$\sum_{i=1}^{n} z_i\,C_i = 0, \tag{2.69}$$

$$\frac{1}{r^2}\frac{\partial}{\partial r}\left(r^2\,U\right) = g. \tag{2.70}$$

where the production terms are given by,

$$P_{ox} = -\min\left(\frac{6}{38}\,P_{atp}\,,\,P_{ox}^{max}\right), \tag{2.71}$$

$$P_{gl} = \frac{1}{6}P_{ox} - \frac{1}{2}\left(P_{atp} + \frac{6}{38}P_{ox}\right), \tag{2.72}$$

$$P_{cd} = -P_{ox} + k_r C_{bi} C_{hy} - k_f C_{cd}, \tag{2.73}$$

$$P_{la} = -2\left(P_{gl} - \frac{1}{6}P_{ox}\right), \tag{2.74}$$

$$P_{hy} = -2\left(P_{gl} - \frac{1}{6}P_{ox}\right) - k_r C_{bi} C_{hy} + k_f C_{cd}, \tag{2.75}$$

$$P_{bi} = k_f C_{cd} - k_r C_{bi} C_{hy}, \tag{2.76}$$

$$P_{ch} = 0, \tag{2.77}$$

with,

$$P_{atp} = \begin{cases} Q_m + Q_q & \text{if} \quad Q_m + Qq < P_{atp}^{max}, \\ Q_q & \text{if} \quad Q_q < P_{atp}^{max} < Q_m + Q_q, \\ 0 & \text{if} \quad P_{atp}^{max} < Q_q, \end{cases} \tag{2.78}$$

$$P_{atp}^{max} = -\frac{38}{6} P_{ox}^{max} - 2 P_{gl}^{max}, \tag{2.79}$$

$$P_{ox}^{max} = \rho R_{ox} \frac{C_{ox}}{C_{ox} + k_{ox}}, \tag{2.80}$$

$$P_{gl}^{max} = \rho R_{gl} \frac{C_{gl}}{C_{gl} + k_{gl}}. \tag{2.81}$$

and,

$$g = \begin{cases} K_M \frac{C_{ox}}{C_{ox}+k_{ox}} \frac{C_{gl}}{C_{gl}+k_{gl}} & \text{if} \quad Q_m + Qq < P_{atp}^{max}, \\ 0 & \text{if} \quad Q_q < P_{atp}^{max} < Q_m + Q_q, \\ -K_{Ne} & \text{if} \quad P_{atp}^{max} < Q_q. \end{cases} \tag{2.82}$$

At the centre of the sphere, $r = 0$,

$$r^2 C_i U - D_i \frac{\partial C_i}{\partial r} - z_i \mu_i F C_i = 0, \tag{2.83}$$

$$U = 0. \tag{2.84}$$

On the outer boundary, at $r = S(t)$,

$$r^2 C_i U - D_i \frac{\partial C_i}{\partial r} - z_i \mu_i F C_i = N_{sh_i} D_{i_{out}} (C_i - C_{\infty_i}) S, \tag{2.85}$$

$$U = \frac{dS}{dt}. \tag{2.86}$$

The initial concentrations of each species is C_{∞_i} and the initial size is 15μm. Values for C_{∞_i}, D_i and N_{sh_i} are given in Table 2.2. Whilst the remaining known parameters are given in Table 2.3. The derivation of the unknown parameters is given in Section 2.4.8 and the values of these parameters are stated in Table 2.4.

2.4.8 Parameters and data fitting

The model summarised in Section 2.4.7 has so far been constructed without fitting any expressions to experimental data. This is an important aspect of the model and a key difference to that presented by Casciari *et al.* [24]. Casciari *et al.* [24] relied heavily on experimental data

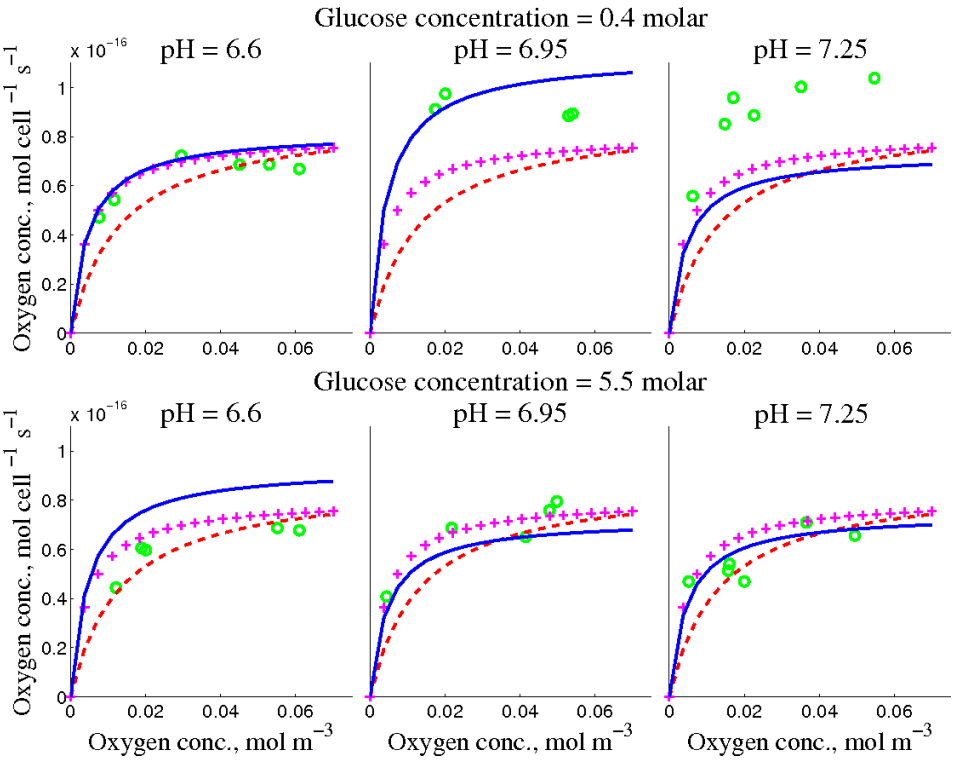

Figure 2.5: Comparison of possible expressions to represent the consumption rate of oxygen. P_{ox}^{max} (- - -) is shown alongside the expression used by Casciari *et al.* [24] (—), a Michaelis Menten expression specifically fitted to the data (+) and experimental data (o) [22].

and in doing so make it challenging to interpret which processes cause which aspects of the results. However there are three parameters in this model that can not be derived from the literature alone. These are the ATP production rate for quiescent cells, Q_q, the glucose Michaelis Menten constant, k_{gl} and the rate of necrosis K_{Ne}. All other parameters have been taken from the literature and are given in Table 2.2 and Table 2.3. The total energy requirement for cells undergo mitosis, $Q_q + Q_m$, was set using data from Table 5 of Freyer and Sutherland [54] regarding the consumption rates of oxygen and glucose of single EMT6/Ro exponential cells[5].

The Michaelis constant k_{ox}, used in describing the consumption of oxygen, has been defined to be the concentration of oxygen at which an environment is defined hypoxic. This choice can be justified by comparing the results using the expression for P_{ox}^{max} determined in this work, equation (2.31), with experimental data for the consumption of oxygen and alternative expressions that could be used. Casciari [22] presents experimental data for the consumption rates of oxygen by EMT6/Ro tumour cells at a a range of oxygen, glucose and hydrogen concentrations. The data presented in [22] alongside the expression, P_{ox}, used in this work are

[5]Consumption rates of unfed plateau cells are also given in [54]. This could be used to fix the energy level of quiescence. However the results of doing so show a central region that is not hypoxic and thus disagrees with experimental data given in [50, 126].

Parameter		Value	Units
ATP production quiescence	Q_q	$2.81 \cdot 10^{-16}$	mol cell^{-1} s^{-1}
Michaelis constant glucose	k_{gl}	2.63	mol m^{-3}
Necrosis rate	K_{Ne}	$1.72 \cdot 10^{-6}$	s^{-1}

Table 2.4: Fitted parameters for the full model.

shown in Figure 2.5. The expression used by Casciari *et al.* in [24] is also included along with a Michaelis Menten expression in which both the consumption rate and Michaelis constant were fitted to the experimental data. Casciari *et al.* include the oxygen concentration as well as the glucose concentration and pH in their description of oxygen consumption, equation (2.1). However neither this nor the fitted Michaelis Menten expression show any better agreement to the experimental data over the range of concentrations given than that used in this model. Therefore it would not aid clarity nor understanding to use a more complicated expression than is necessary and thus equation (2.31) is used to model oxygen consumption.

The three parameters that were not defined by the literature were found by solving the model and comparing the diameter of the spheroid to data regarding the size of EMT6/Ro spheroids during early stages of growth; taken from Landry *et al.* [97]. The model was solved and the data was fitted using MATLAB [174], further details of the numeric code used to solve the model are given in Section 2.4.9. MATLAB's inbuilt function, 'fminsearchbnd' [94],was implemented to fit Q_q, k_{gl} and K_{Ne} to the data in [97]. This function uses the Nelder Mead algorithm to minimise a function in a multidimensional space. For further reading on the Nelder Mead algorithm see [130] or [194]. The values of the fitted parameters are given in Table 2.4 and the resulting fit is shown in Figure 2.6 along with the experimental data. All fixed parameter values are given in Table 2.3.

2.4.9 Results and discussion of full model

The full system of modelling equations given in Section 2.4.7 was solved numerically in MATLAB. The moving boundary was accommodated by transforming the expanding domain, $r \in [0, S(t)]$ to a stationary domain, $\eta \in [0, 1]$ by the transformation $r = \eta S(t)$. The resultant equations, rearranged into conservation form, were spatially discretised using a centrally spaced finite difference method before being discretised in time using the backward Euler method. This system of equations was then solved at each time step by Newtons method using Broyden's method to update the Jacobian. For further reading on Broyden's method see [17] or [1]. Analysis of the error of the numerical scheme implemented is given in Appendix B.

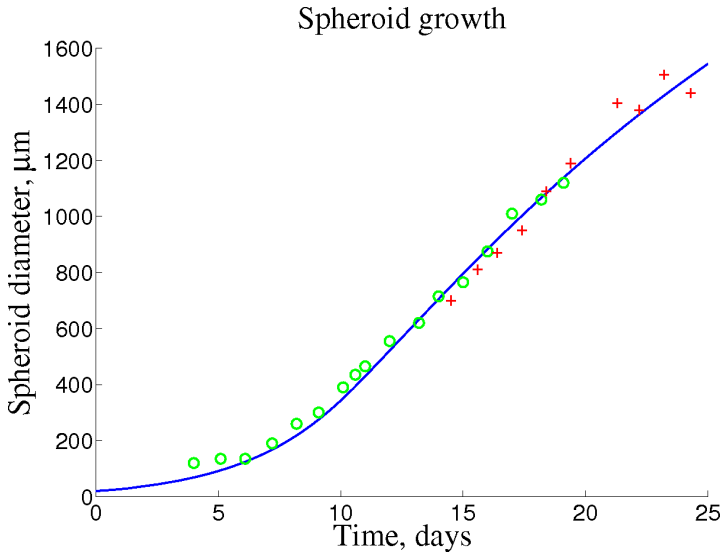

Figure 2.6: Growth derived by solving the full tumour model (—) and fitting to experimental data (o, +) [97].

When solving the model care needs to be taken in two particular areas. These are the singularity at the origin in equation (2.10) and the piecewise nature of the expressions for the ATP demand and growth; equations (2.33) and (2.66). The singularity in equation (2.10) at the centre was dealt with in the following way. Equation (2.10) was first transformed to the stationary domain and rearranged into conservation form, such that,

$$\frac{\partial S C_i}{\partial \tau} + \frac{\partial}{\partial \eta}\left(-\dot{S}\eta C_i\right) + \frac{1}{\eta^2}\frac{\partial}{\partial \eta}\left(\eta^2 N_i\right) = S P_i. \tag{2.87}$$

L'Hopitals rule was then imposed at $\eta = 0$. The governing equation for the conservation of a chemical species i at the centre, can then be given by,

$$\frac{\partial S C_i}{\partial \tau} + \frac{\partial}{\partial \eta}\left(-\dot{S}\eta C_i\right) + 3\frac{\partial N_i}{\partial \eta} = S P_i \quad \text{at } \eta = 0. \tag{2.88}$$

The finite difference discretization described above was then implemented.

The piecewise nature of equations (2.33) and (2.66) causes convergence problems when solving the model numerically. Thus a continuous approximations of these functions were implemented. These were such that,

$$P_{atp} = Sw_1 Q_m + Sw_2 Q_q \tag{2.89}$$

and

$$g = Sw_1 K_M \frac{C_{ox}}{C_{ox} + k_{ox}} \frac{C_{gl}}{C_{gl} + k_{gl}} - Sw_2 K_{NE}, \tag{2.90}$$

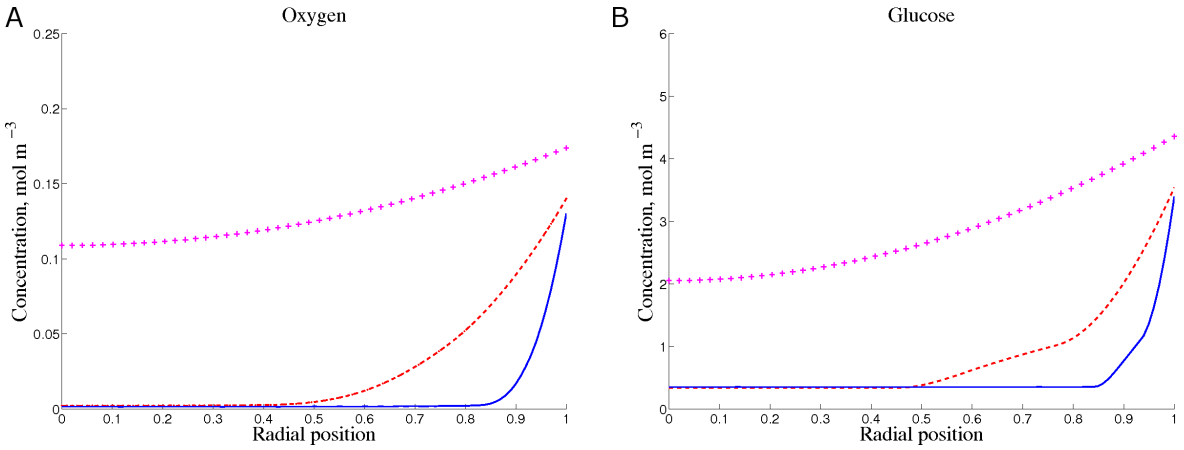

Figure 2.7: The concentration of oxygen (**A**) and glucose (**B**) through tumour spheroids of radii $200\mu m$ (+), $500\mu m$ (- - -) and at the final size of $1435\mu m$ (—).

where,

$$Sw_1 = \frac{1}{2}\left(1 + \tanh\left(\lambda\left(P_{atp}^{max} - Q_m - Q_q\right)\right)\right) \tag{2.91}$$

and

$$Sw_2 = \frac{1}{2}\left(1 + \tanh\left(\lambda\left(P_{atp}^{max} - Q_q\right)\right)\right). \tag{2.92}$$

Increasing the coefficient λ gives a better representation to the discrete case but increases the likelihood of numerical difficulties. A value of $\lambda = 500$ was used in this work.

Results of the model presented are shown in figures 2.7 through to 2.11, in which concentration profiles are shown at radii of 200μm, 500μm and the final radius of approximately 1400μm. In figures 2.7 to 2.11 the radial distance has been nondimensionalised using the radius of the tumour spheroid, S. Figure 2.7 shows the concentration profiles of oxygen and glucose. At a radius of 200μm the MCTS is small enough for both oxygen and glucose to diffuse throughout the entire tumour. The surface concentration of both species are lower than in the medium surrounding the tumour due to the flux condition imposed on the outer boundary. The demand for ATP is sufficiently high that it can not be met by aerobic respiration alone, thus anaerobic respiration makes up the deficit. As the concentration of oxygen reduces the demand for anaerobic respiration increases and thus the rate of glucose consumption increases, shown in Figure 2.8. Thus during the initial growth phase the concentration of glucose is reduced further than that of oxygen.

It can be seen in Figure 2.9 that shortly after the tumour has grown beyond a radius of 200μm the centre of the MCTS runs out of sufficient resources to continue undergoing mitosis. This is due to diffusion providing an inadequate transport mechanism for oxygen and glucose over this distance. The centre becomes quiescent and demands less ATP to be produced. At this stage, shown in Figure 2.8, the centre is yet to become hypoxic. Thus aerobic respiration

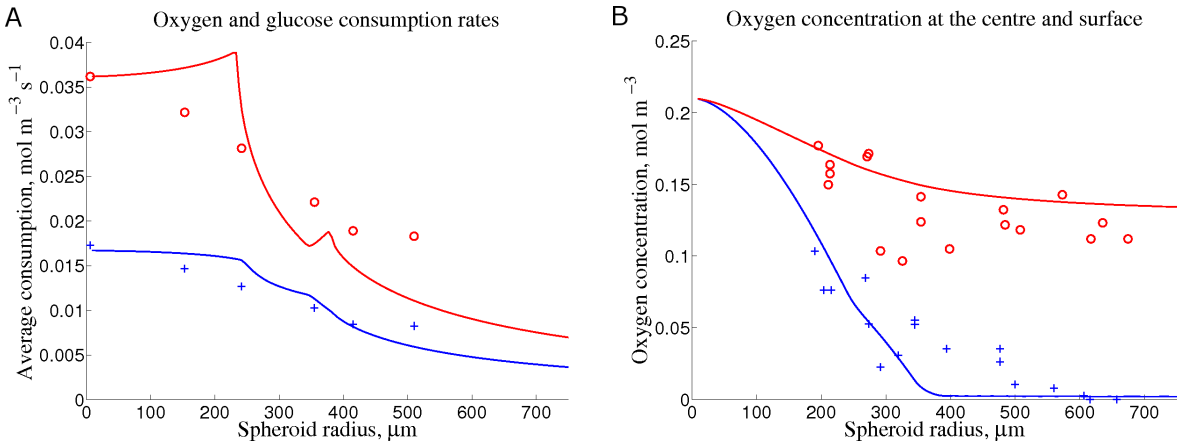

Figure 2.8: **A**: The average consumption rates of the spheroid for oxygen (—) and glucose (—) compared against experimental data (+, o) [54]. **B**: The concentration of oxygen at the centre (—) and surface (—) of a tumour compared against experimental data (+, o) [122].

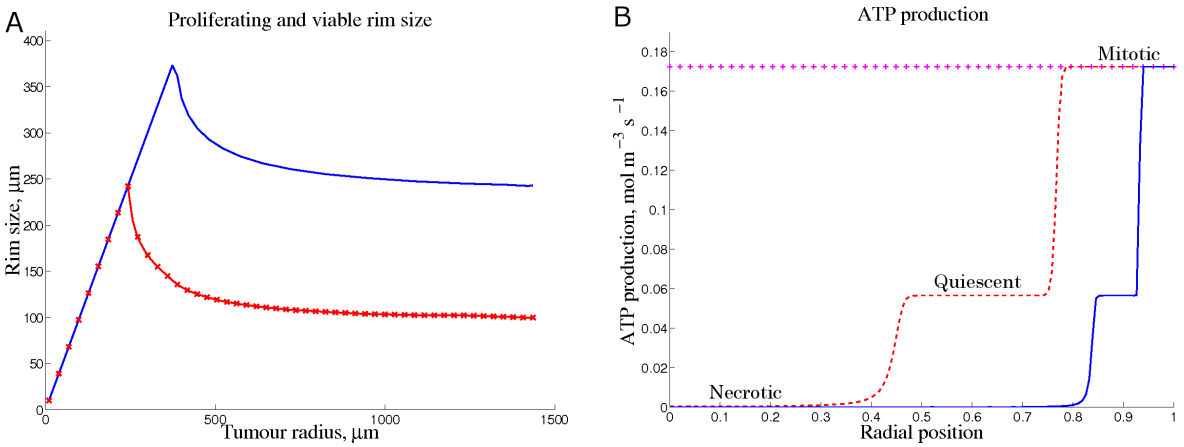

Figure 2.9: **A**: The size of the proliferating (—×—) and viable (—), rims. **B**: The concentration of ATP through tumour spheroids of radii $200\mu m$ (+), $500\mu m$ (- - -) and at the final size of $1435\mu m$ (—).

continues to contribute to the reduced ATP demand and is once again used in preference to anaerobic respiration. This causes a heavily reduced demand for glucose at the tumour centre, such that the centre becomes hypoxic before the concentration of glucose becomes critical. As the spheroid continues to grow and the oxygen concentration lowers anaerobic respiration once again tries to meet the deficit, however the low concentration of glucose results in this becoming insufficient too and thus the centre becomes necrotic shortly after it became hypoxic[6]. The MCTS continues to grow until the negative growth effects from necrotic core balance that of the proliferating rim.

[6]Figures 2.8 and 2.9 show the radius of the tumour at the onset of quiescence, hypoxia and necrosis to be approximately 240μm, 350μm and 375μm respectively.

To verify this model the results have been compared to a range of experimental data. Figure 2.8**A** shows the average oxygen and glucose for cells in a MCTS. Both the oxygen and glucose curves are in a good comparison to the experimental data. In the model the demand for glucose is determined by the requirement of ATP by cells and in particular the demand for ATP using anaerobic respiration. This is reflected in the consumption of glucose by the two peaks which correspond with the onset of quiescence and necrosis. Initially the concentration of oxygen and glucose is high throughout the tumour. As the tumour grows there comes a size whereby the diffusion rate of oxygen is not high enough to meet consumption and so the concentration of oxygen in the centre drops. In this region the production of ATP by aerobic respiration will be reduced. The rate of anaerobic respiration with increase to meet the ATP demand and consequently the consumption rate of glucose will increase. This explains the initial increase in the glucose consumption rate in Figure 2.8**A**. As the tumour grows further it will eventually reach a size whereby the glucose supply is restricted in the centre such that the cells can not produce enough ATP to undergo mitosis and will become quiescent. At this point the demand for both oxygen and glucose at the centre will drop significant. This is shown in Figure 2.8**A** by the first peak in the glucose curve. The newly formed quiescent region can initially meet a proportion of its ATP demand by aerobic respiration. Consumption and growth of the tumour will once again reduce the concentration of oxygen in the centre and cause an increase in the rate of anaerobic respiration until the glucose concentration becomes sufficiently low that necrosis is initiated. This is shown in Figure 2.8**A** by the second peak in the glucose curve. After the onset of necrosis the tumour will continue to grow until it reaches it equilibrium size. During this time the proportion of the tumour that is necrotic will increase and thus the average consumption rates of oxygen and glucose will decrease.

The concentration of oxygen at both the tumour centre and surface is shown in Figure 2.8**B**. The data is distributed over a wide range of values, however the results of the model show a good fit. The concentration of oxygen at the surface is in part affected by the Sherwood number used in the flux boundary condition. The experimental data indicates that a lower Sherwood number could be used to more accurately model the surface conditions. The predicted oxygen concentration at the centre is lower than that seen experimentally for spheroids of radius greater than 350μm. This suggests that preference for aerobic respiration may not be as strong in quiescent cells. Although there is obvious room for improvement the model performs well in comparison to the results presented by Casciari *et al.* in [24].

The model presented in the section was designed to show the effects of metabolism on the growth of a MCTS and also show the effects of quiescence and necrosis. This has been successfully done and is highlighted in Figures 2.7 and 2.9. Figure 2.9**B** shows the size of the proliferating and viable rim as the tumour spheroid grows. The viable rim is of a EMT6/Ro MCTS is given by Freyer and Sutherland [54, 56] to be in the region of 200μm for large spheroids. This is slightly lower than that seen in the results presented however indicates that

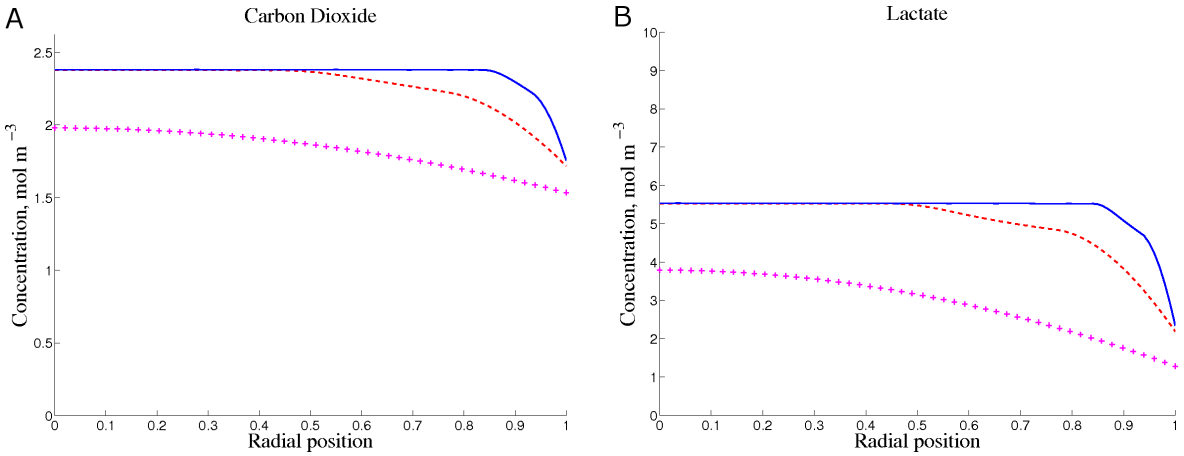

Figure 2.10: The concentration of carbon dioxide (**A**) and lactate (**B**) through tumour spheroids of radii 200μm (+), 500μm (- - -) and at the final size of 1435μm (—).

the region of growth and transport mechanisms show good correlation with what is taking place experimentally. Although the concentrations of waste products were derived the model did not allow them to affect growth or ATP demand. The concentration profiles of carbon dioxide and lactate are shown in Figure 2.10, whilst pH and the gradient in electric potential are shown in Figure 2.11. The small range in values of the concentration profiles for carbon dioxide, lactate and pH suggests that the effects of waste would be small. The increase in carbon dioxide is negligible and although the increase in lactate is more substantial the effects of the buffering reaction result in only a small variation in pH. The spikes in the results for pH given in Figure 2.11 coincide with outer edges of the necrotic and quiescent regions and are caused by an increase in anaerobic respiration prior to a cell change from being mitotic to quiescent to necrotic. The largest values of the electric potential gradient are found at the surface relative which coincides with where the largest gradients in species concentration are. These gradients in concentration are due to the waste materials that are being produced inside the tumour diffusing out into the surrounding medium. However even at the surface the gradients in electric potential are still small.

The model predicts that the tumour would grow to a diameter of 2870μm. This can be compared to data in Freyer [50] which suggests the size of a tumour grown under the conditions set out in this model should be 2759μm. Although the model shows good comparison to this data it does suggest that the growth term may need reviewing. Compared to experimental literature [50, 124] the radius at which necrosis is seen is also high. This highlights the need for a deeper understanding of the causes of necrosis which in turn will be implemented in the expression for growth. It maybe that the mechanical forces that build up during the growth of the spheroid affect the onset of necrosis. Alternatively a review of the different environments that cause apoptosis rather than necrosis may be required.

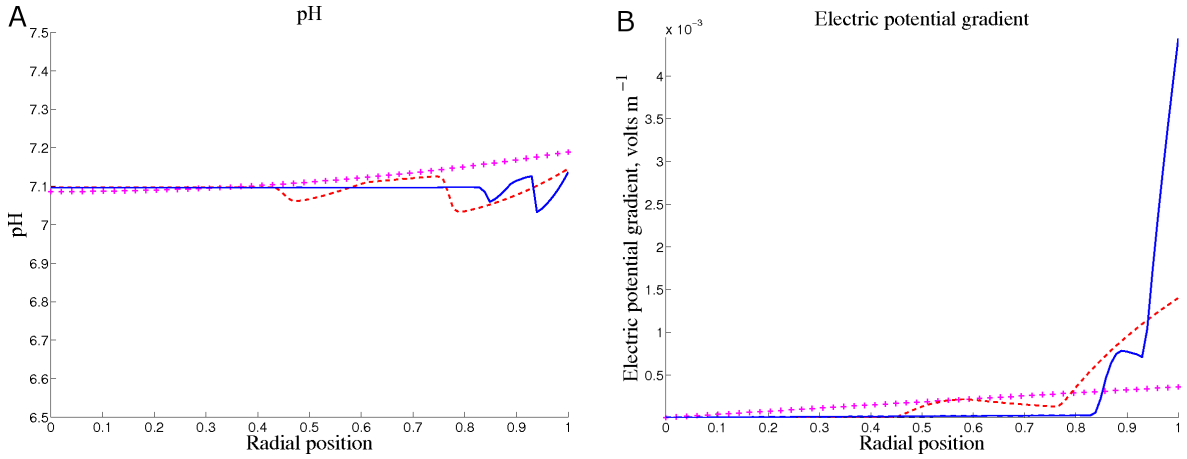

Figure 2.11: The pH (**A**) and electric potential gradient (**B**) through tumour spheroids of radii $200\mu m$ (+), $500\mu m$ (- - -) and at the final size of $1435\mu m$ (—).

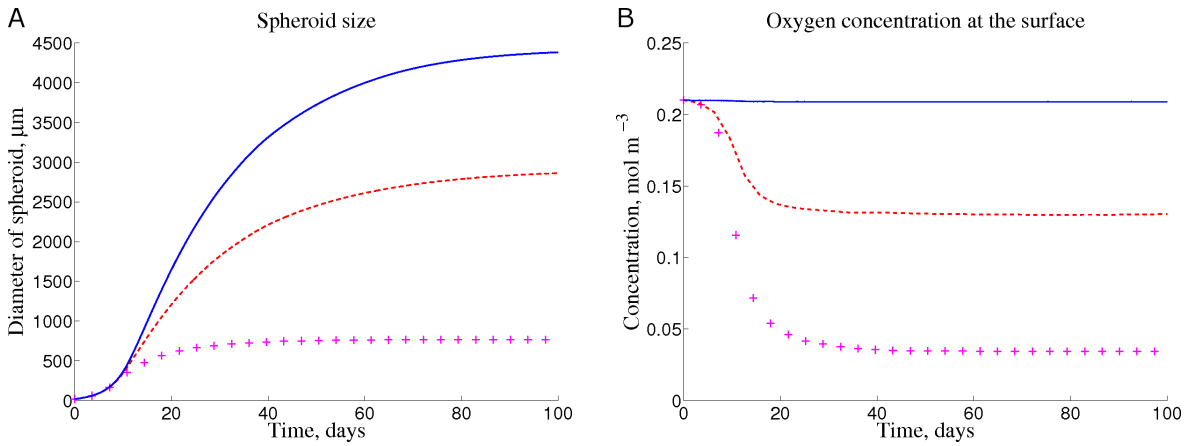

Figure 2.12: The diameter of spheroid (**A**) and concentration of oxygen at the spheroid surface (**B**), predicted for Sherwood numbers of $N_{sh_i} \cdot 10^{-2}$ (+), N_{sh_i} (- - -) and $N_{sh_i} \cdot 10^{2}$ (—).

2.5 Tumour modelling: Simple model

The aim of this work was to construct a mathematical model that accurately replicates the growth of an *in vitro* MCTS. The model aims to show how the chemical species within the tumour affect the spheroid growth and highlight which individual species or collection of species have the largest influence. This would enable a simplified model to be created that can be used in further modelling and investigations into tumour growth. The model presented in Section 2.4 accommodates a wide range of aspects regarding metabolism and cell states and agrees well with experimental data for EMT6/Ro cells. By changing parameter values the model could be easily adjusted to model the growth of other cell lines. Equally if an alternative cell line was governed by different metabolic processes, such as the Crabtree effect rather than the Pasteur effect, then the production rates could be easily changed to accommodate this. However in this

study, whilst continuing to study the EMT6/Ro cell line, we shall now construct a simplified model of that given in Section 2.4 which will continue to accurately model the growth but focus solely on the dominating factors.

2.5.1 Analysis of full model and derivation of simplified model

We will establish which mechanisms have the largest effect within the MCTS by nondimensional analysis of the model presented in Section 2.4.7. The details of this are given in Appendix A. The nondimensional form of equation (2.67) is,

$$\alpha_i \frac{\partial \hat{C}_i}{\partial t} + \frac{1}{\hat{r}^2} \frac{\partial}{\partial \hat{r}} \left(\hat{r}^2 \left(\alpha_i \hat{C}_i \hat{U} - \left(\frac{\partial \hat{C}_i}{\partial \hat{r}} + z_i \beta_i C_i \frac{\partial \hat{\Phi}}{\partial \hat{r}} \right) \right) \right) = \gamma \hat{P}_i, \tag{2.93}$$

where α_i, β_i and γ_i are nondimensional constants given in Table A.1. For a chemical species C_i, α_i is of the order 10^{-3} or lower. Therefore, along with the time derivative, transport due to advection can be neglected. The effects of charge migration are shown to be small as β_i is of the order 10^{-3}. Thus charge migration can be neglected and species transport can be considered in terms of diffusion alone. With the exception of hydrogen and chlorine the leading expression in each production term is of the same order as diffusion. Chlorine is not produced in this model and thus there is no production. Even though the diffusion coefficient for hydrogen is relatively large, the production of hydrogen is shown to be three orders of magnitude greater than the effects of diffusion. This helps to explain the distribution of hydrogen presented in Figure 2.11 and suggests that transport can be neglected when considering the distribution of hydrogen. Therefore a suitable model for each chemical species would be,

$$-\frac{1}{r^2} \frac{\partial}{\partial r} \left(r^2 D_i \frac{\partial C_i}{\partial r} \right) = P_i, \tag{2.94}$$

and hydrogen can be further simplified to,

$$P_{hy} = 0. \tag{2.95}$$

We shall now consider which species are required to model the growth of MCTS. Figure 2.11**A** shows the pH for various sizes of tumour spheroid. Initially the pH of the tumour was 7.25. Due to the cell line preference for aerobic respiration and the efficiency of the buffering reaction there was little variation in pH during subsequent growth. Throughout the course of the simulation the pH resided between 7 and 7.25. The concentrations of carbon dioxide and lactate also show relatively small variations during the experiment. Thus the decision to neglect the adverse effects of waste production on growth is shown to be valid. Therefore a simplified model can neglect carbon dioxide, lactate and pH as well as the chemical and ionic

buffers. Thus the reduced model is,

$$-\frac{1}{r^2}\frac{\partial}{\partial r}\left(r^2\, D_{ox}\,\frac{\partial C_{ox}}{\partial r}\right) \;=\; P_{ox}, \tag{2.96}$$

$$-\frac{1}{r^2}\frac{\partial}{\partial r}\left(r^2\, D_{gl}\,\frac{\partial C_{gl}}{\partial r}\right) \;=\; P_{gl}, \tag{2.97}$$

$$\frac{1}{r^2}\frac{\partial}{\partial r}\left(r^2\, U\right) \;=\; g. \tag{2.98}$$

where P_{ox}, P_{gl} and g are defined below. The initial concentrations of oxygen and glucose are equal to that found in the medium. At the spheroid centre we impose no flux and the averaged velocity is zero. At the outer surface the flux condition as described in Section 2.4.4 will be implemented such that,

$$r^2\left(-D_i\,\frac{\partial C_i}{\partial r}\right) \;=\; D_{i_{out}}\left(C_i - C_{\infty_i}\right) S \quad \text{at } r \;=\; S(t). \tag{2.99}$$

2.5.2 Metabolic reactions

We shall now consider the consumption of oxygen and glucose and review the previous expressions implemented for P_{ox} and P_{gl}. The expressions laid out in Section 2.4 for P_{ox}, P_{gl} and g are independent of waste products and buffering and thus can be imposed in the model directly above. By the nondimensional analysis of the full model, these production terms will yield similar results to that given in Section 2.4.9. However the discrete nature of those terms make solving the resulting equations complicated. Simpler expressions can be derived by once again assuming Michaelis Menten kinetics. The results shown in Figure 2.7 show that oxygen is consumed until the concentration is zero. Glucose consumption stops whilst there is still glucose present within the cell's local microenvironment. We shall therefore assume that oxygen and glucose are both required for mitosis and that a low concentration of glucose will trigger necrosis. The demanded rate of ATP production will therefore be given by,

$$P_{atp} \;=\; Q_q\,\frac{C_{gl}}{C_{gl}+k_{ne}} \;+\; Q_m\,\frac{C_{ox}}{C_{ox}+k_{ox}}\,\frac{C_{gl}}{C_{gl}+k_{gl}}, \tag{2.100}$$

where k_{ne} is a newly introduced Michaelis constant that describes when cells change from being quiescent to necrotic due to the local glucose concentration. Equivalently k_{ox} and k_{gl} determine when cells will change from being mitotic to quiescent due to the local oxygen and glucose concentrations. Equation (2.100) can be directly implemented into the previous equation for oxygen production,

$$P_{ox} \;=\; -\min\left(\frac{6}{38}\,P_{atp}\,,\,P_{ox}^{max}\right). \tag{2.101}$$

Substituting this new expression for ATP production, equation (2.100), into the previous expression for glucose production, equation (2.60), implies that in the absence of oxygen the consumption rate of glucose is unbounded. This is a physically inaccurate anomaly that must be dealt with. In Section 2.4.5, the maximum possible glucose consumption was represented by,

$$P_{gl}^{max} \;=\; \rho\, R_{gl}\, \frac{C_{gl}}{C_{gl} + k_{gl}}. \tag{2.102}$$

This will be replaced by,

$$P_{gl}^{max} \;=\; \rho\, R_{gl}\, \frac{C_{gl}}{C_{gl} + k_{ne}}, \tag{2.103}$$

to include glucose consumption at very low concentrations. Therefore to prevent unbounded glucose consumption the previous expression for glucose production will be replaced with,

$$P_{gl} \;=\; \frac{1}{6} P_{ox} \;-\; \min\left(\frac{1}{2}\left(P_{atp} + \frac{6}{38} P_{ox}\right),\, P_{gl}^{max}\right). \tag{2.104}$$

2.5.3 Growth

In light of the updated expressions for the ATP and glucose production rates, we shall review the expression given in Section 2.4.6 for the growth rate g. Mechanical forces and cell shedding will once again be neglected, whilst the rate of ATP produced due to mitosis is now a function of Michaelis Menten for oxygen and glucose. ATP production is dependent on the concentrations of oxygen and glucose and the values of k_{ox} and k_{gl}. The glucose concentration and value of k_{ne} will then define whether a cell is quiescent or necrotic. Therefore the ATP production will be proportional to the rate of mitosis and similarly the proportion of cells consuming ATP solely for quiescence will imply the rate of necrosis. This can be reflected in an expression for growth by,

$$g \;=\; K_M \frac{C_{ox}}{C_{ox} + k_{ox}}\, \frac{C_{gl}}{C_{gl} + k_{gl}} \;-\; K_{Ne}\left(1 - \frac{C_{gl}}{C_{gl} + k_{ne}}\right). \tag{2.105}$$

[7] The consumption rates of oxygen and glucose given by Freyer and Sutherland [54] have been multiplied by $(1 + k_{ox}/C_{\infty_{ox}})$ and $(1 + k_{gl}/C_{\infty_{gl}})$ so that the production rates are not affected by the Michaelis Menten expressions. The rates of ATP production for mitotic and quiescent cells have been adjusted similarly.

Parameter		Value	Units	Ref.
ATP production mitosis	$Q_q + Q_m$	$1.08 \cdot 10^{-15}$	mol cell^{-1} s^{-1}	[54]
ATP production quiescence	Q_q	$5.92 \cdot 10^{-16}$	mol cell^{-1} s^{-1}	[54]
Cell density	ρ	$2.01 \cdot 10^{14}$	cell m^{-3}	[24]
Glucose consumption rate	R_{gl} [7]	$7.94 \cdot 10^{-16}$	mol cell^{-1} s^{-1}	[54]
Michaelis constant oxygen	k_{ox}	$1.32 \cdot 10^{-2}$	mol m^{-3}	[79]
Oxygen consumption rate	R_{ox}	$8.82 \cdot 10^{-17}$	mol cell^{-1} s^{-1}	[54]
Rate of mitosis	K_M	$1.48 \cdot 10^{-5}$	s^{-1}	[97]

Table 2.5: Table of parameters given by the literature for the simple model.

2.5.4 Summary equations for the simplified model

The modelling equations are,

$$-\frac{1}{r^2}\frac{\partial}{\partial r}\left(r^2\, D_{ox}\,\frac{\partial C_{ox}}{\partial r}\right) \;=\; P_{ox}, \tag{2.106}$$

$$-\frac{1}{r^2}\frac{\partial}{\partial r}\left(r^2\, D_{gl}\,\frac{\partial C_{gl}}{\partial r}\right) \;=\; P_{gl}, \tag{2.107}$$

$$\frac{1}{r^2}\frac{\partial}{\partial r}\left(r^2\, U\right) \;=\; K_M \frac{C_{ox}}{C_{ox}+k_{ox}}\,\frac{C_{gl}}{C_{gl}+k_{gl}} \;-\; K_{Ne}\left(1-\frac{C_{gl}}{C_{gl}+k_{ne}}\right). \tag{2.108}$$

where the production terms are given by,

$$P_{ox} \;=\; -\min\left(\frac{6}{38}\,P_{atp}\,,\,P_{ox}^{max}\right), \tag{2.109}$$

$$P_{gl} \;=\; \frac{1}{6}P_{ox} \;-\; \min\left(\frac{1}{2}\left(P_{atp}+\frac{6}{38}P_{ox}\right)\,,\,P_{gl}^{max}\right), \tag{2.110}$$

$$P_{atp} \;=\; Q_q\,\frac{C_{gl}}{C_{gl}+k_{ne}} \;+\; Q_m\,\frac{C_{ox}}{C_{ox}+k_{ox}}\,\frac{C_{gl}}{C_{gl}+k_{gl}}. \tag{2.111}$$

The system of equations are completed by boundary conditions; at the centre of the sphere, $r = 0$,

$$r^2\, D_{ox}\,\frac{\partial C_{ox}}{\partial r} \;=\; 0, \tag{2.112}$$

$$r^2\, D_{gl}\,\frac{\partial C_{gl}}{\partial r} \;=\; 0, \tag{2.113}$$

$$U \;=\; 0. \tag{2.114}$$

Parameter		Value	Units
Michaelis constant glucose	k_{gl}	2.90	mol m^{-3}
Michaelis constant necrosis	k_{ne}	0.34	mol m^{-3}
Necrosis rate	K_{Ne}	$1.92 \cdot 10^{-6}$	s^{-1}

Table 2.6: Fitted parameters for the simple model.

On the outer boundary, at $r = S(t)$,

$$r^2 D_{ox} \frac{\partial C_{ox}}{\partial r} = N_{sh_{ox}} D_{ox_{out}} (C_{ox} - C_{\infty_{ox}}) S, \tag{2.115}$$

$$r^2 D_{gl} \frac{\partial C_{gl}}{\partial r} = N_{sh_{gl}} D_{gl_{out}} \left(C_{gl} - C_{\infty_{gl}}\right) S, \tag{2.116}$$

$$U = \frac{dS}{dt}. \tag{2.117}$$

Initially at $t = 0$, the tumour has the radius of a cell, 15μm. The values of N_{sh_i} and C_{∞_i} are given in Table 2.2.

2.5.5 Parameters and fitting

We aim to compare the simplified model laid out in Section 2.5.4 to the experimental data and modelling predictions described in Section 2.4. To enable as accurate comparison as possible the same parameters that were taken from the literature and used in Section 2.4 will once again be used in this alternative model. The values derived by fitting will be re-derived using the same process as laid out in Section 2.4.8. Once again the unknown parameters were derived by comparing the modelling predictions for the diameter of the spheroid to data regarding the size of EMT6/Ro spheroids during early stages of growth [97]. The initial fit to this data resulted in a tumour with an unrealistically small maximum size. Hence a maximum size of a tumour, taken from Freyer [50], was also used. The parameters that were fitted to the data were, the rate of necrosis, K_{Ne} and glucose Michaelis constants k_{gl} and k_{ne}. The rate of ATP production for quiescence was not included in the fitting process for this model, but was derived from oxygen and glucose consumption rates for exponential and unfed EMT6/Ro cells given in Freyer and Sutherland [54]. The values of the parameters taken from literature are given in Table 2.5. The values of the fitted parameters are given in Table 2.6, and the modelling predictions for spheroid growth compared to the experimental data is shown in Figure 2.13. The fitted final diameter was 2783μm compared to 2759μm given in [50].

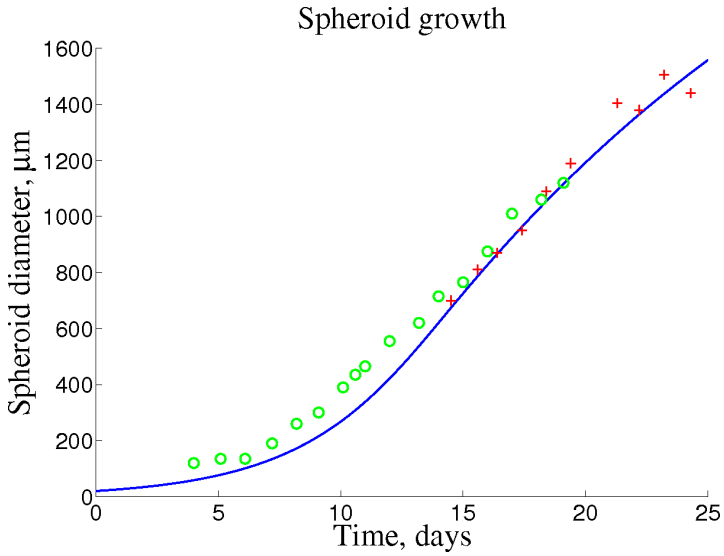

Figure 2.13: Growth derived by solving the simplified model (—) and fitting to experimental data (o, +) [97].

2.6 Results and discussion of simple model

This simplified model was solved numerically using the method described in Section 2.4.9. The moving boundary was once again dealt with by transforming the expanding domain, $r \in [0, S(t)]$ to a stationary domain, $\eta \in [0, 1]$ by the transformation $r = \eta S(t)$ and $t = \tau$. The transformed model that governs the concentration of oxygen and glucose is,

$$-\frac{1}{S^2\eta^2}\frac{\partial}{\partial\eta}\left(\eta^2 D_i \frac{\partial C_i}{\partial\eta}\right) = P_i. \tag{2.118}$$

The model was then solved as a system of boundary value problems.

The oxygen and glucose profiles are shown in Figure 2.14. The oxygen profile is similar to that derived by the full model, however the new expression for P_{atp} does not cease ATP production until the resources are unavailable for ATP production to be possible. Therefore the centre of the tumour has become absent of both oxygen and glucose.

The production of ATP, shown in Figure 2.15, shows the mitotic, quiescent and necrotic rims less clearly than in the full model. This is due to the continuous definition of ATP production used in this model. However, the region in Figure 2.15**A** in which ATP production is greater than zero indicates the viable rim and the region in Figure 2.15**B** where the gradient of the velocity is positive gives the proliferating rim. Thus for a fully grown tumour the viable rim is approximately 280μm and the proliferating rim is approximately 180μm wide. These widths are lower but comparable with the full model.

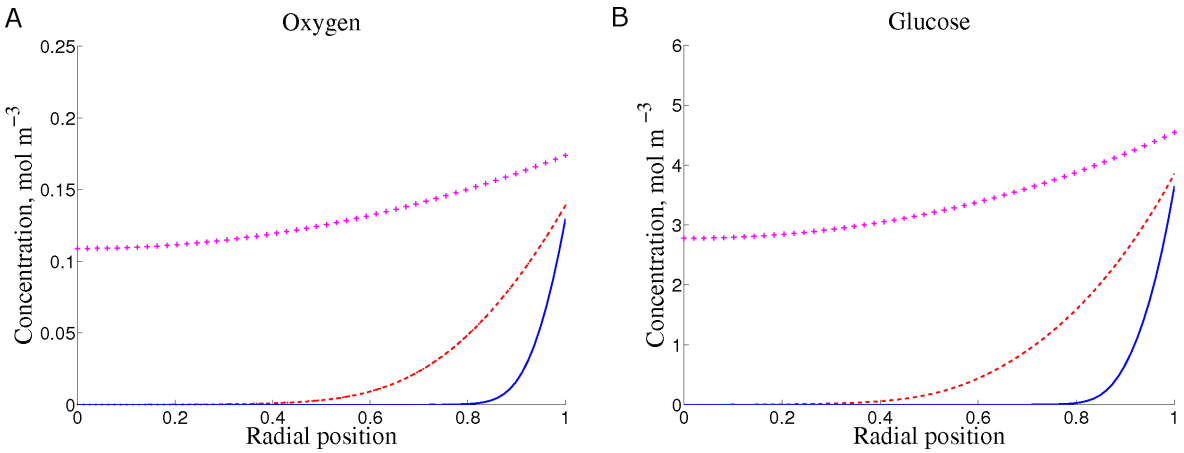

Figure 2.14: The concentration of oxygen (**A**) and glucose (**B**) through tumour spheroids of radii 200μm (+), 500μm (- - -) and at the final size of 1392μm (—).

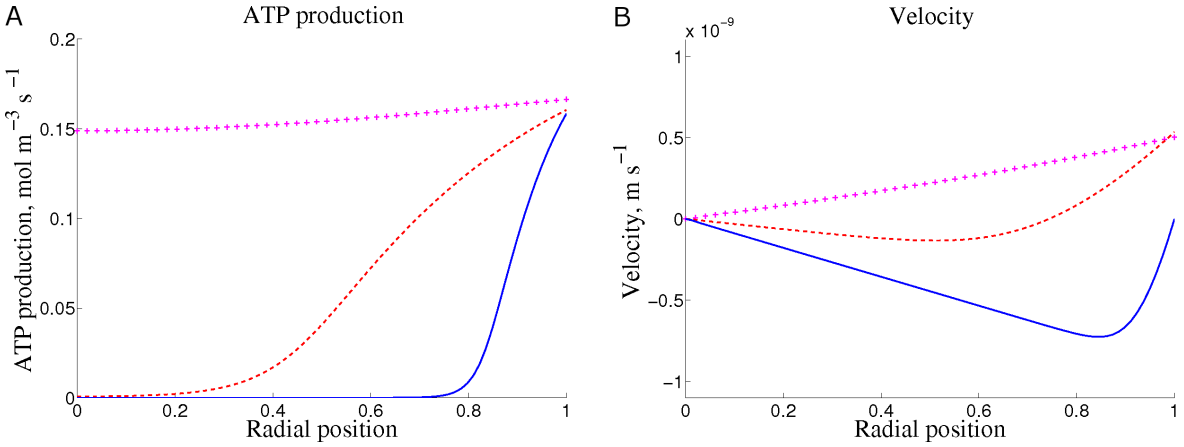

Figure 2.15: The concentration of ATP (**A**) and averaged velocity (**B**) through the tumour spheroid, at radii of 200μm (+), 500μm (- - -) and at the final size of 1392μm (—).

The simplified model presented in this section again shows good comparison to experimental data as shown in Figure 2.16. Glucose consumption is lower than the data suggests at all sizes. For small spheroid sizes this could be helped by using a smaller Michaelis constant, k_{gl}. However this would have a knock on effect for the rate of growth and eventually maximum size. Oxygen consumption at the tumour centre and surface are similar to that presented by the full model and thus compare well with the experimental data. This was expected as the expression for oxygen production is the same in both the full and simplified models. Only effects from the growth rate could have affected the concentrations.

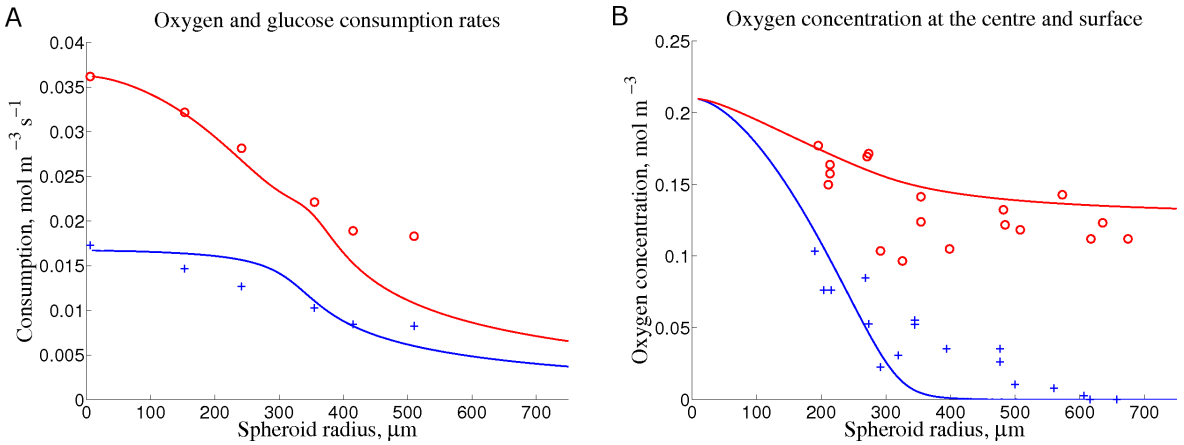

Figure 2.16: **A**: The average consumption rates of the spheroid for oxygen (—) and glucose (—) compared against experimental data (+ , o) [54]. **B**: The concentration of oxygen at the centre (—) and surface (—) of a tumour compared against experimental data (+, o) [122].

2.7 Discussion

In this chapter we have studied the growth of a MCTS, with particular focus on the energy requirements of cells in different phases of the cell cycle. The growth of tumour spheroids have been modelled by incorporating a range of chemical species. Alongside modelling the distribution of nutrients, waste materials and buffering chemicals, a structure has also been laid down to study the effects of regions of cell proliferation, quiescence and necrosis. These cell states were determined by the available chemical energy that could be obtained from the cells surrounding environment. This work has shown it is possible to construct a model of the effects of aerobic respiration, anaerobic respiration and ATP demand, whilst not relying on the fitting of experimental data to accomplish this. Together with oxygen and glucose, the initial 'full' model included the waste products that are a consequence of respiration; carbon dioxide, lactic acid and hydrogen. The concentrations of these waste products were shown to have little to no effect on the size of the growth of the tumour spheroid. Similarly the effects of charge migration on the transport of ions were shown to be negligible in comparison to diffusion. The most influential factors on the growth of tumours was shown to be the concentration of oxygen and glucose. In particular in relation to the switch over from aerobic to anaerobic respiration, as this determined the onset of quiescence and eventually necrosis.

It was shown that the full model could be simplified to a model of tumour growth that only required the concentrations of oxygen and glucose. The model could not be simplified further to a single species model as this failed to fit the experimental data. The simplified model showed equally good comparison to the experimental data and continued to explain the effects of cell mitosis, quiescence, necrosis and respiration. The limitations of the simple model were that it failed to distinctly highlight the different regions of mitosis, quiescence and necrosis

as well as the full model. Both models ignored the potential mechanical effects of stress and strain on growth. These effects could greatly alter the state of a cell and advance the onset of quiescence and necrosis and will be considered further in Chapter 3.

Both the models presented in this chapter have shown it is insufficient to model the growth of a MCTS by solely modelling the distribution of oxygen or a single nutrient. The chemical factor that limits the growth of a tumour spheroid has been shown to be glucose. However oxygen must also be included to restrict mitosis and thus define the onset of quiescence. Deriving the concentration of oxygen is also necessary to determine the rate of glucose consumption and the onset of necrosis. The models presented have been shown to be good representations of a growing EMT6/Ro MCTS when compared to experimental data and other mathematical models such as [24]. Unlike other models we have been able to represent aerobic respiration and anaerobic representation alongside mitotic, quiescent and necrotic regions, whilst giving a framework that could be adapted to model the growth of other cell lines and include other effects such as mechanical forces.

Chapter 3

Mechanical forces within a growing MCTS

3.1 Introduction

In Chapter 2 the effects of the cell cycle and cell metabolism on the the growth of a MCTS were explored. The model presented neglected the mechanical forces that are developed during growth and the effects they may have on the tumour spheroid. In this chapter we shall review that decision by studying the development of stresses and strains that are generated within a growing tumour.

A morphoelastic model based on that presented by Hall [71], will be applied to the tumour model presented in Section 2.5, to study the radial and circumferential forces that develop during the growth of a tumour spheroid. This growth model neglects changes in the cell cycle and changes in metabolism that may occur due to cell stresses. However the effects of proliferation, quiescence and necrosis on the development of forces can be seen and will be discussed alongside an explanation of how the tumour grows in relation to these forces. The results of this morphoelastic model will be compared to experimental data regarding the magnitude of stresses calculated from spheroid cultures. The predicted stress field will then be used to determine the shape that arises from a tumour spheroid when it is sliced in half.

This chapter will begin by reviewing previous techniques and work presented on modelling the mechanical forces within a growing tissue construct. This will be achieved by viewing the problem from both a mathematical modelling and experimental view point. The morphoelastic model will then be presented in Section 3.3, including a discussion of the modelling equations and assumptions they are based upon. The model will then be simplified in Section 3.4 by studying the equations in the incompressible limit. The direction of growth of a cell is

dependent on how sensitive the cell is to its local stress field. The effects of this will be examined in Section 3.5. The development of stresses and strains within a growing MCTS will then be studied. This will be achieved by looking at three limits; when the direction of growth has no dependence on the local stress field, when the direction of growth is moderately sensitive to the local stress field and when the direction of growth in highly sensitive to the local stress field. The results of this sensitivity analysis will then be presented and discussed in Section 3.6. These results will be compared against experimental data and the growth model presented in Chapter 2, in which mechanical effects on growth were neglected, will be reviewed. The results of the morphoelastic model will then be used to study the deformation of a tumour spheroid that is sliced in half. The model governing this deformation will be given in Section 3.7 and the results will be presented in Section 3.8.

3.2 Literature review

We shall now give a brief outline of the literature regarding studies into the mechanical forces that build up inside tissue structures. In particular the evolution of stresses and strains within growing tumour spheroids will be considered, as well as their role in defining the overall volume of a tumour and the size of any necrotic regions. Both mathematical models and experimental findings will be discussed.

Many of the recent studies of tumour mechanics have been influenced by the experiment work of Helmilinger *et al.*, [73]. These *in vitro* experiments have studied the effects of mechanical stresses on the growth of a tumour spheroid. Helmlinger *et al.* [73] and Koike *et al.* [92] have both shown the equilibrium spheroid size and the rate of growth were inhibited by increased stiffness of the surrounding medium. Helmlinger *et al.* showed that this stiffness also affected the tumour on a cellular level. Higher levels of stress decreased the percentage of cells undergoing both proliferation and apoptosis, although this effect was also shown to be dependent on the size of the spheroid. More recent work by Cheng *et al.* [28] has shown that a cell's position within the cell cycle is not exclusively determined by the local concentration of nutrients. High levels of stress were shown to reduce the rate of proliferation and promote necrosis.

Various approaches have been taken to model the evolution of forces within growing tissue. Jones *et al.* [88] study the effect of non-uniform growth on mechanical stresses within avascular tumours grown under various conditions. The model presented studies the tumour as a continuous material, such that the properties of local volumes of the tumour are considered rather than individual cells. The effects of stress are not included in the equation for growth, thus there is no preferential direction of growth of the tumour in response to the stress field. The results of this model show that near the surface of the tumour, where the concentration

of nutrients is high and the rate of proliferation is unimpeded, the cells will be under compression. Equivalently, far away from the periphery, in regions of low nutrient concentration and a high net cell death rate, the cells will be under tension. The model presented by Jones *et al.* is developed by Araujo and McElwain [9] who implement anisotropic growth into their model, in which proliferation occurs in the direction of least stress. Similarly the directional preference of necrosis is such that the necrotic cells are replaced by cells moving in the direction of greatest stress.

The properties of necrotic cores in avascular tumours was the particular focus of a series of papers by Please and co-workers. In these papers tumours were modelled as a two phase inviscid fluid, consisting of cells and an extracellular fluid, water. The model presented by Please *et al.* [145], modelled the internal environment of a tumour by modelling cell proliferation as the conversion of water into cells. Equivalently the death of a cell resulted in the cell being converted back into water. The pressure in the extracellular fluid compacts the cells. The results of this work saw necrosis occurring when the pressure in the fluid surrounding the cells was greater than the pressure acting between the cells, causing the cells to be ripped apart. This work was then extended in [146] for tumour spheroids, in which surface tension was included such that a steady state solution was determined. Landman and Please, [95] revise the model presented in [145] and [146], with the aim of gaining a better understanding of the effects of tensile forces. The resultant model assumes the tumour consists of a region of densely packed viable cells under compression and a region of predominantly dead cells at a lower density, in which the remaining living cells are isolated. Results are shown for a range of surface tensions and the effects regarding the eventual size of the tumour spheroid are presented. Under zero surface tension it is shown that the growth of the tumour will be unbounded. Following Landman and Please, [95], Chen *et al.* [27] extended the model by incorporating the mechanical effects from the surrounding environment. Chen *et al.* show that the onset of necrosis, along with the equilibrium size of the tumour, is determined by the stiffness of the external environment.

MacArthur and Please, [110], present a model building on the ideas present by Jones *et al.* [88] and Please and co-workers [95, 145, 146]. This model studies the development of stress within a Maxwell type visco-elastic MCTS. The results of the model show that differing rates of proliferation within the tumour, driven by gradients in nutrients, lead to a non-uniform stress distribution, in particular large hoop stresses. The model also shows the importance of including viscosity into the system, without which a steady state stress profile is not reached.

Many recent studies into the mechanical forces evolving within soft tissue growth base their work on that presented by Rodriguez *et al.* [149]. Rodriguez *et al.* present a generalised continuum model of finite volumetric growth of an elastic tissue. The growth of the soft tissue is decomposed into the evolution of the material under zero stress and the relating elastic deformation. These ideas were then developed into a study of the stability of growing elastic

materials by Ben Amar and Goriely in [10]. The work done in [10] was further developed into a general theory of morphoelasticity by Goriely and Ben Amar, [67], which models the net effect of small incremental growth steps. Ambrosi and Mollica, [4] apply the ideas presented in [149] to model the growth of a tumour inside a a rigid cylinder and to a MCTS. The results for the MCTS show the spheroid to be in hoop compression near the surface whilst the centre is in tension. This is due to the non uniform distribution of nutrients and consequently non uniform growth. Similar to the work by Chen *et al.* [27], Ambrosi and Mollica, [5] then develop the model presented in [4] to model the growth of a tumour spheroid as a solid, considering the growth to be in both free suspension and surrounded by a poroelastic medium. Further models of tissue growth incorporating the ideas of Rodriguez *et al.*, [149], are presented in [2, 3, 71, 107].

Further information and reviews of the mechanical forces and modelling of soft biological tissue are given in [34] and [82].

3.3 Morophoelasticity model

We wish to study the mechanical forces that develop in a growing tumour spheroid. The time scale in which the extracellular fluid flows is much smaller than the time scale for growth of the tumour. Pressure gradients in the interstitial fluid will thus be small, such that the fluid pressure is assumed constant. Therefore we shall neglect the effects of the fluid surrounding the cells and consider a tumour as a continuous elastic solid. The stresses and strains that develop during growth will be modelled using the continuum morphoelastic model developed by Hall, [71]. This approach is based on that presented by Rodriguez *et al.*, [149] and developed by Goriely and Ben Amar, [67]. The model presented by Hall develops the work of Goriely and Ben Amar, [67] further by including a more generalised expression for growth, with time given as a continuous variable. A summary of the modelling equations is given below. For a full derivation of the model, and comparison to previous work see Hall [71].

The model presented by Hall [71] is valid for small strains, where strain is defined by relating the current distance, to the desired distance between two points, *i.e.* under no stress; this imposes that zero strain will imply zero stress. Assuming that the strains were small, the full infinitesimal Eulerian strain tensor, $\boldsymbol{e}$, was derived in [71]. In this study we are considering the forces that arise during the growth of a tumour spheroid. Thus we shall assume spherical symmetry and neglect the effects of shear. Therefore the strain tensor derived by Hall in [71] can be simplified to,

$$\frac{De_{ij}}{Dt} + \frac{1}{2}\, e_{kk}\, (L_{ij} + L_{ji}) = \frac{1}{2}\, (L_{ij} + L_{ji}) - G_{ij}, \tag{3.1}$$

where e is the strain tensor, G is the growth tensor and L the velocity gradient tensor defined as,

$$L_{ij} = \frac{\partial U_i}{\partial x_j}, \tag{3.2}$$

such that U is the velocity of the tissue. Although complex, equation (3.1) can be derived from linear elasticity and simply states the rate of change of strain, following a particle, accounting for changes in orientation, is equal to the difference between how the particle does grow and how the particle would like to go.

We shall assume that the tumour is made up of a linearly elastic material, therefore the stress, σ, strain relationship is defined by,

$$\sigma_{ij} = \lambda \delta_{ij} e_{kk} + 2 \mu e_{ij}, \tag{3.3}$$

where λ is Lamé's first coefficient and μ is the shear modulus. Body and inertial forces shall be neglected such that,

$$\frac{\partial \sigma_{ij}}{\partial x_j} = 0. \tag{3.4}$$

The growth tensor is defined by Hall [71] to be,

$$G_{ij} = \frac{g}{3} \delta_{ij} + \kappa \left(\sigma_{ij} - \frac{1}{3} \delta_{ij} \sigma_{kk} \right), \tag{3.5}$$

where g is the net rate of growth and κ describes the sensitivity of direction of growth in response to stress. The size of κ does not influence the total growth of the tumour as the sum over all components of the growth tensor equals net growth g. This equation allows the growth of the material to be anisotropic, such that by increasing κ the direction of growth of the tumour is made more sensitive to the local stress field and will grow to minimise the stress field. However this growth tensor allows for rearrangement of the tissue when the net rate of growth is zero, *i.e.* when the tissue is effectively quiescent. In this work we shall modify the equation for growth presented by Hall [71], maintaining the previous directional growth preferences, but also imposing that once growth has ceased the tissue will remain in a constant state. This will be achieved by implementing,

$$G_{ij} = g \left(\frac{1}{3} \delta_{ij} + \kappa \left(\sigma_{ij} - \frac{1}{3} \delta_{ij} \sigma_{kk} \right) \right). \tag{3.6}$$

The net rate of growth, g, is given by the properties of the growing material and is defined by a separate equation. The net rate of growth determines the rate of proliferation, necrosis and the transition between mitosis, quiescence and necrosis. Thus our choice of g is crucial in deriving the mechanical forces that develop during growth. In this study we shall use the net growth rate that was derived in the tumour model presented in Section 2.5. This will be

explained further in Section 3.6.

As in the models presented in Chapter 2 we shall consider a tumour that is spherically symmetric. Thus converting to spherical coordinates we have that the physical components are,

$$e_{rr} = e_r, \quad e_{\theta\theta} = e_\theta, \quad e_{\phi\phi} = e_\theta, \tag{3.7}$$

$$\sigma_{rr} = \sigma_r, \quad \sigma_{\theta\theta} = \sigma_\theta, \quad \sigma_{\phi\phi} = \sigma_\theta, \tag{3.8}$$

$$G_{rr} = G_r, \quad G_{\theta\theta} = G_\theta, \quad G_{\phi\phi} = G_\theta, \tag{3.9}$$

with the remaining off-diagonal elements being zero and where subscript r and θ represent the radial and circumferential components. Using [166] we can derive the velocity gradient in terms of the radial velocity U such that,

$$\boldsymbol{L} = \operatorname{diag}\left(\frac{\partial U}{\partial r}, \frac{U}{r}, \frac{U}{r}\right), \tag{3.10}$$

The morphoelastic model is now given by,

$$\frac{De_r}{Dt} + (e_r + 2\,e_\theta)\,\frac{\partial U}{\partial r} = \frac{\partial U}{\partial r} - G_r, \tag{3.11}$$

$$\frac{De_\theta}{Dt} + (e_r + 2\,e_\theta)\,\frac{U}{r} = \frac{U}{r} - G_\theta, \tag{3.12}$$

$$\sigma_r = \lambda\,(e_r + 2\,e_\theta) + 2\,\mu\,e_r, \tag{3.13}$$

$$\sigma_\theta = \lambda\,(e_r + 2\,e_\theta) + 2\,\mu\,e_\theta, \tag{3.14}$$

$$\frac{\partial \sigma_r}{\partial r} + \frac{2}{r}\,(\sigma_r - \sigma_\theta) = 0, \tag{3.15}$$

and growth is such that,

$$G_r = \frac{g}{3}\,(1 + 2\,\kappa\,(\sigma_r - \sigma_\theta)), \tag{3.16}$$

$$G_\theta = \frac{g}{3}\,(1 + \kappa\,(\sigma_\theta - \sigma_r)). \tag{3.17}$$

The divergence of a rank 2 tensor in spherical coordinates was taken from [166]. Net growth is derived by summing the growth in all three directions, *i.e.* the sum of the radial growth and twice the circumferential growth therefore,

$$g = G_r + 2\,G_\theta. \tag{3.18}$$

Following the method set out by Hall in [71], the radial strain and circumferential stress can

be replaced such that,

$$e_r = e_T - 2\,e_\theta \quad \text{and} \quad \sigma_\theta = \sigma_r - \beta, \tag{3.19}$$

where e_T is the total strain and β is the difference between radial and circumferential stress. Equations (3.11) to (3.17) can now be simplified such that,

$$\frac{De_T}{Dt} + e_T\left(\frac{\partial U}{\partial r} + 2\,\frac{U}{r}\right) = \frac{\partial U}{\partial r} + 2\,\frac{U}{r} - g, \tag{3.20}$$

$$\frac{De_\theta}{Dt} + e_T\,\frac{U}{r} = \frac{U}{r} - \frac{g}{3}\,(1 - \kappa\,\beta)\,, \tag{3.21}$$

$$\sigma_r = (\lambda + 2\,\mu)\,e_T - 4\,\mu\,e_\theta, \tag{3.22}$$

$$\beta = 2\,\mu\,(e_T - 3\,e_\theta)\,, \tag{3.23}$$

$$\frac{\partial \sigma_r}{\partial r} + \frac{2}{r}\,\beta = 0. \tag{3.24}$$

Initial and boundary conditions

The model is completed by specifying appropriate initial and boundary condition. We assume that the tumour will initially have no internal stresses and will be in equilibrium with its surrounding environment, such that,

$$e_r = 0 \quad \text{and} \quad e_\theta = 0, \quad \text{at } t = 0. \tag{3.25}$$

Spherical symmetry imposes that the centre is a stationary point under zero strain such that,

$$U = 0, \quad e_r = 0 \quad \text{and} \quad e_\theta = 0, \quad \text{at } r = 0. \tag{3.26}$$

At the outer boundary, $S(t)$, it will be assumed there is a constant normal stress being applied by the surrounding environment. This stress will be denoted by p_0 and therefore,

$$\sigma_r = -p_0, \quad \text{at } r = S(t). \tag{3.27}$$

3.4 Incompressible limit

Both cells and the extracellular matrix inside a tumour are comprised mainly of water. Water is incompressible with a Poisson's ratio of approximately one half, therefore we can assume the cells, the surrounding matrix and the extracellular water are all incompressible. However the extracellular water is free to move and thus the tumour is in fact a compressible material.

This is verified in literature in which Poisson's ratio's as low as 0.35, [89], have been given for soft tissue. However, to aid understanding of the individual components we wish to keep the growth model and mechanics model separate. Therefore we will consider a tumour which is incompressible and for which Poisson's ratio is one half. In making this approximation we hope to simplify the model and identify the dominant relationships within the system.

To aid analysis of the morphoelasticity model presented in equations (3.20) to (3.24), we shall nondimensionalise the system by defining the replacement variables,

$$r = r_0\,\hat{r}, \quad t = t_0\,\hat{t}, \quad g = t_0^{-1}\,\hat{g}, \quad U = \frac{r_0}{t_0}\,\hat{U}, \tag{3.28}$$

$$\sigma_r = \mu\,\hat{\sigma_r}, \quad \beta = \mu\,\hat{\beta}, \tag{3.29}$$

where r_0 and t_0 are typical length and time scales of our system. Lamé's first coefficient, λ and the shear modulus, μ, are related to the Young's Modulus, E, and Poisson's ratio, ν, by,

$$\lambda = \frac{E\,\nu}{(1\,+\,\nu)\,(1\,-\,2\,\nu)} \quad \text{and} \quad \mu = \frac{E}{2\,(1\,+\,\nu)}. \tag{3.30}$$

The forces that build up during growth will cause strains in the radial and circumferential directions. However the magnitude of the total strain will be dependent on the incompressibility of the material and consequently Poissons ratio. Therefore we shall scale the total strain such that,

$$e_T = \frac{\mu}{\lambda}\,\hat{e_T} \tag{3.31}$$

where,

$$\frac{\mu}{\lambda} = \frac{1\,-\,2\,\nu}{2\nu}. \tag{3.32}$$

The resulting rescaled system of equations is,

$$\frac{\mu}{\lambda}\left(\frac{D\hat{e_T}}{D\hat{t}} + \hat{e_T}\left(\frac{\partial\hat{U}}{\partial\hat{r}} + 2\,\frac{\hat{U}}{\hat{r}}\right)\right) = \frac{\partial\hat{U}}{\partial\hat{r}} + 2\,\frac{\hat{U}}{\hat{r}} - \hat{g}, \tag{3.33}$$

$$\frac{De_\theta}{D\hat{t}} + \frac{\mu}{\lambda}\,\hat{e_T}\,\frac{\hat{U}}{\hat{r}} = \frac{\hat{U}}{\hat{r}} - \frac{\hat{g}}{3}\left(1 - \kappa\,\mu\,\hat{\beta}\right), \tag{3.34}$$

$$\hat{\sigma_r} = \left(1 + 2\,\frac{\mu}{\lambda}\right)\,\hat{e_T} - 4\,e_\theta, \tag{3.35}$$

$$\hat{\beta} = 2\,\left(\frac{\mu}{\lambda}\,\hat{e_T} - 3\,e_\theta\right), \tag{3.36}$$

$$\frac{\partial\hat{\sigma_r}}{\partial\hat{r}} + \frac{2}{\hat{r}}\,\hat{\beta} = 0. \tag{3.37}$$

The above system of equations are now in terms of two numbers, $\kappa\,\mu$ and $\frac{\mu}{\lambda}$. The sensitivity

of growth to the local stress field will determine $\kappa\,\mu$ and this is discussed further in Section 3.5. considering Poisson's ratio is close to a half we find that $\frac{\mu}{\lambda}$ is small. We therefore take a regular expansion of the above system of equations and deduce that to leading order the system can be approximate by[1],

$$\frac{\partial \hat{U}}{\partial \hat{r}} + 2\,\frac{\hat{U}}{\hat{r}} = \hat{g}, \tag{3.38}$$

$$\frac{De_\theta}{D\hat{t}} = \frac{\hat{U}}{\hat{r}} - \frac{\hat{g}}{3}\left(1 - \kappa\,\mu\,\hat{\beta}\right), \tag{3.39}$$

$$\hat{\sigma_r} = \hat{e_T} - 4\,e_\theta, \tag{3.40}$$

$$\hat{\beta} = -6\,e_\theta, \tag{3.41}$$

$$\frac{\partial \hat{\sigma_r}}{\partial \hat{r}} + \frac{2}{\hat{r}}\,\hat{\beta} = 0. \tag{3.42}$$

There is now only one unknown constant in this problem, κ. This governs the sensitivity of growth in response to stress. The effects of different sizes of κ can take shall now be discussed.

3.5 Sensitivity analysis

Under the assumptions of small strain and an incompressible tumour, the model of morphoelasticity proposed by Hall, [71], has been simplified to a system of equations in which the direction of growth in relation to sensitivity to stress is the only undefined parameter. Therefore, before solving the system, we shall study the different cases in which $\kappa\mu$ is small, order one and large; these relate to insensitive growth, moderately sensitive growth and highly sensitive growth in response to differences between radial and circumferential stress. Firstly it is useful to note that equation (3.41) implies that the circumferential strains and the nondimensional parameter $\hat{\beta}$ are of the same order. In this model strains are assumed to be small, therefore neither e_θ and $\hat{\beta}$ can be large.

Insensitive growth, $\kappa\mu << 1$

For a tumour in which cells do no change their preferred direction of growth due to differences in the size of the radial and circumferential stress, $\kappa\mu$ will be small. Therefore the leading

[1]Note that an equivalent interpretation of equation (3.38) is that the divergence of the velocity equals growth to leading order. In Chapter 2 this was derived by considering the conservation of cells within the tumour in which the density remained constant, incompressible.

order balance of equation (3.39), for $\kappa\mu << 1$, will be,

$$\frac{De_\theta}{D\hat{t}} = \frac{\hat{U}}{\hat{r}} - \frac{\hat{g}}{3}. \tag{3.43}$$

The growth of the tumour will not depend on the build up of internal stress; daughter cells will align at random, independent of the local stress field and thus will grow isotropically and hence significant stresses will be created. This is similar to the limit considered by Jones *et al.* [88].

Moderately sensitive growth, $\kappa\mu = \mathcal{O}(1)$

A tumour in which $\kappa\mu$ is order one will be said to be experiencing moderately sensitive growth. In this case, when a cell undergoes mitosis, the resulting daughter cells will be added so that they partially align with the direction of minimum compression or maximum tension, thus moderating the stress within the tumour. The sensitivity in this regime is not small enough to be neglected, nor large enough to dominate over the material derivative of circumferential strain. Thus there is a balance between all terms in equation (3.39).

Highly sensitive growth, $\kappa\mu >> 1$

The final case is when growth is highly sensitive to stress, such that $\kappa\mu$ is large. For an appropriately large value of $\kappa\mu$, the growth due to directional preferences is much greater than the contribution from the material derivative of circumferential strain. Thus the circumferential strain term can be neglected and equation (3.39) can be replaced by,

$$-\frac{\hat{g}}{3}\,\kappa\,\mu\,\hat{\beta} = \frac{\hat{U}}{\hat{r}} - \frac{\hat{g}}{3}. \tag{3.44}$$

In this regime growth will reduce the stress, by adding each newly formed daughter cell in the direction of maximum tension or minimum stress.

Further analysis of this equation shows that this this will only hold whilst the entire tumour is growing. This can be seen by rearranging equation (3.44) for $\hat{\beta}$,

$$\hat{\beta} = \frac{1}{\kappa\mu}\left(1 - \frac{3\hat{U}}{\hat{r}\hat{g}}\right). \tag{3.45}$$

Before necrosis, zero net growth will occur simultaneously with zero velocity and a zero gradient in the velocity at the centre of the spheroid. At the onset of necrosis, the points at which the tumour has zero velocity will no longer coincide with zero growth. Thus there will be a

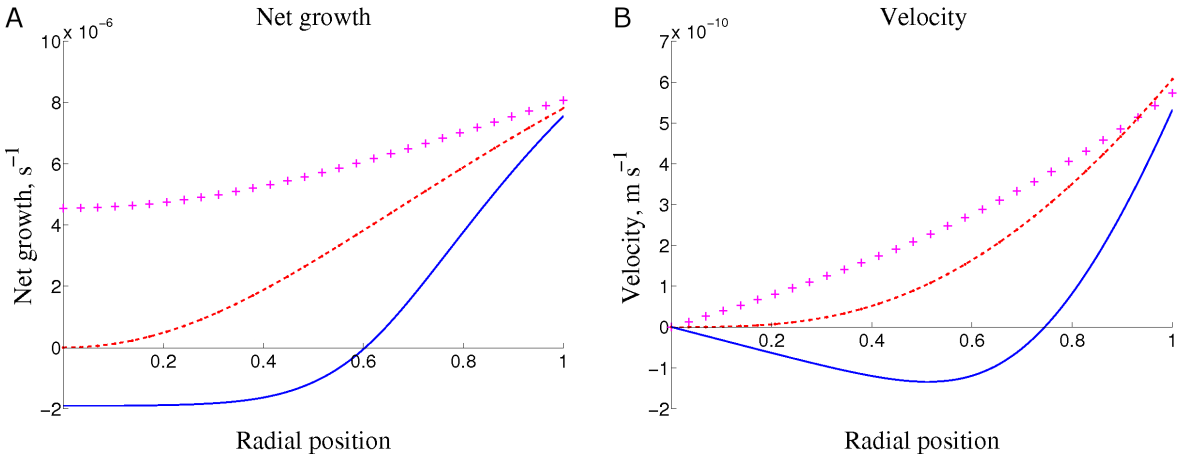

Figure 3.1: The rate of growth (**A**), and velocity (**B**) through a tumour spheroid of radii $250\mu m$ (+), $339\mu m$ (- - -) and $500\mu m$ (—).

singularity in equation (3.45) and $\hat{\beta}$ will become infinitely large. We have previously neglected the contribution from the material derivative of circumferential strain. However necrosis will produce large gradients in strain on a very short time scale and thus result in a change to the leading order balance of equation (3.39). Therefore up until the point in time when necrosis first occurs equation (3.44) is valid. But thereafter we must implement equation (3.39). There is clearly a singular perturbation problem that arises in this limit, however this is beyond the scope of this thesis.

3.6 Results

We shall now implement the morphoelasticity model as laid out in Section 3.3 to the model of a growing MCTS as presented in Section 2.5. The model presented in Section 2.5 is a spherically symmetric model of an avascular tumour grown in free suspension such that,

$$p_0 = 0. \tag{3.46}$$

The net growth rate was said to be dependent on both oxygen and glucose and defined by,

$$g = K_M \frac{C_{ox}}{C_{ox} + k_{ox}} \frac{C_{gl}}{C_{gl} + k_{gl}} - K_{Ne} \left(1 - \frac{C_{gl}}{C_{gl} + k_{ne}}\right). \tag{3.47}$$

In the incompressible limit that we are considering, equations (2.98) and (3.38) are equivalent. Therefore, because net growth and the concentration profiles of oxygen and glucose do not depend on the stresses or strains of the tumour, the growth model and the morphoelasticity problem decouple the model for tumour growth can be solved using the method as described

Sensitivity	κ
Insensitive growth	$\mu^{-1} \cdot 10^{-3}$
Moderately sensitive growth	μ^{-1}
Highly sensitive growth	$\mu^{-1} \cdot 10^{3}$

Table 3.1: Values of sensitivity to growth parameter κ.

in Section 2.6. The results of the tumour model give both g and U, thus the morphoelastic model can be solved in isolation. Although not visible in the graphical results of the tumour model shown in Figure 2.15, there are minor oscillations in the results for the growth velocity, especially close to the centre. These inaccuracies caused numerical problems when trying to use this data as input into the morphoelastic model. Various possible methods were explored to gain the greater accuracy required to ensure a stable numerical solution. Eventually the previous implementation of the trapezium rule to integrate the growth term in equation (2.108) was replaced by a four point Gauss quadrature method. The resulting solutions of net growth and the velocity are given in Figure 3.1.

The resulting equations of the morphoelastic model were solved numerically in MATLAB [174]. Thus far the model has assumed incompressibility and in doing so that Poisson's ratio is a half. However this is impractical when trying to solve numerically, as, for example, this would lead to an infinite value of λ. Therefore the implemented values of Poisson's ratio and Young's modulus were 0.499999 and $1.23 \cdot 10^4$ [109] respectively. Equation (3.39) was rewritten in terms of e_θ by imposing equation (3.41). The resulting first order hyperbolic equation was then solved using the method of characteristics. The characteristic equations and the corresponding family of ODEs were then integrated using the trapezium rule. The resulting solution for e_θ then enables $\hat{\beta}$ to be determined algebraically. The trapezium rule can then be implemented to integrate equation (3.42) and calculate the radial stress, $\hat{\sigma_r}$. The solution for radial stress was then used to derive the final unknown variable, $\hat{e_T}$, by algebraically solving equation (3.40). The values of κ used in each case are given in Table 3.1.

The results of the model in the three limits of sensitivity studied are shown in figures 3.2 to 3.4. The distribution of radial and circumferential stress and strain have been shown at three different sizes of spheroid. These have been chosen to represent a tumour of $250\mu m$, in which all cells are either proliferating or quiescent, *i.e.* growth is positive, a tumour of $339\mu m$, at the onset of necrosis, *i.e.* growth at the centre is less than zero, and a tumour of $500\mu m$, for which there is an established necrotic core. Due to the size of the stresses and strains that develop in a tumour that is highly sensitive to stress, the final results in Figure 3.4 are given for a smaller spheroid, of radius $342\mu m$, than those in figures 3.2 and 3.3. Before we discuss the results of the individual cases with respect to sensitivity of growth, we shall first give a

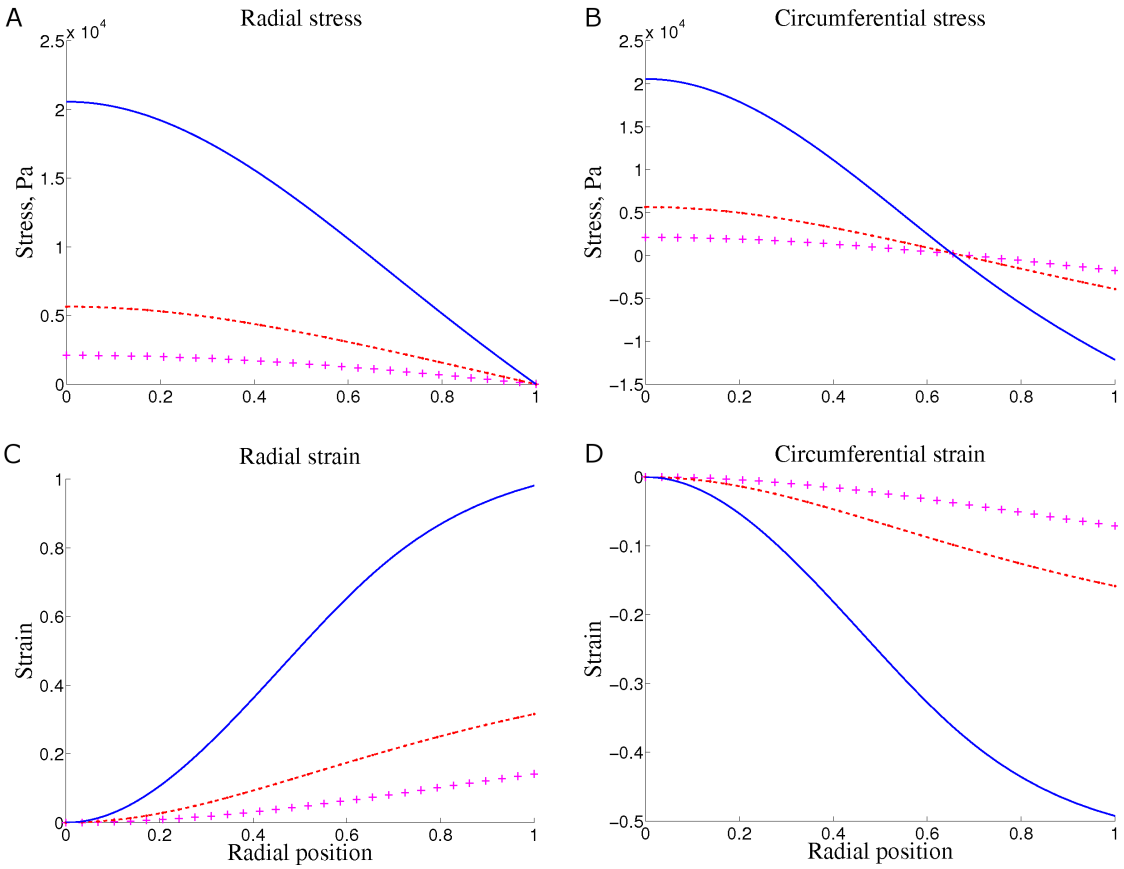

Figure 3.2: The radial stress (**A**), circumferential stress (**B**), radial stain (**C**) and circumferential strain (**D**) through a tumour of radii 250μm (+), 339μm (- - -) and 500μm (—) in which growth is insensitive to stress.

general overview of some of the growth characteristics.

The model presented assumes the growth of the sphere is radially symmetric. The growth rate in the sphere is non-uniform and decreases as the radial distance from the surface increases. Growth is therefore at its maximum on the tumour surface. As the spheroid grows the outer cells 'drag' the cells in the centre of the sphere out. This results in the sphere being under radial tension. This can be represented in two dimensions by imagining two adjacent circular rings of cells. If the two circles are unconstrained, the growth will cause both rings to increase in size, however the ring on the outside will be growing faster and thus the diameter of this ring will be growing at a faster rate than the ring inside it. The two rings must remain adjacent and not separate. Therefore there is a force between them keeping them together and this is why the spheroid is under radial tension. For a spherical tumour this analogy is simply extended to consider adjacent shells in three dimensions. The cells experiencing the maximum tension are those with the most cells trying to pull them outwards, *i.e.* in the centre. The large radial forces pulling the central cells outwards, results in the cells being in

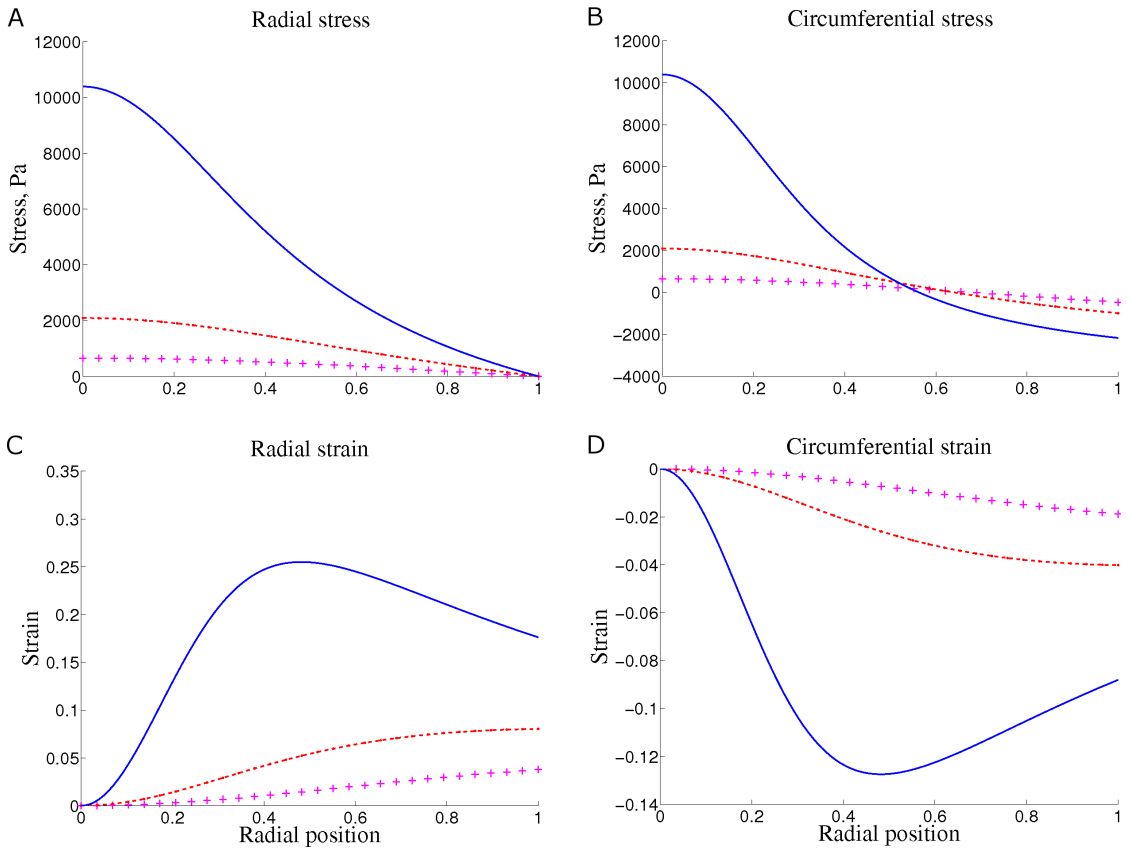

Figure 3.3: The radial stress (**A**), circumferential stress (**B**), radial stain (**C**) and circumferential strain (**D**) through a tumour spheroids of radii $250\mu m$ (+), $339\mu m$ (- - -) and $500\mu m$ (—) in which $\kappa\mu = \mathcal{O}(1)$.

circumferential tension as they attempt to remain attached to their neighbouring cells. In the outer regions of the sphere the difference in growth rate between the cells is small and is close to the maximum growth rate. Therefore the drag effect is less. Close to the surface the cells are growing at a rate equivalent to that of those on the surface. Radial stresses are negligible as these are relieved by the expansion of the outer boundary. Circumferential stresses build up due to growth and thus there is a region close to the tumour surface experiencing large circumferential compressive forces, which, due to radial symmetry can not be relieved.

In many elastic models stress and strain are proportional. However by subtracting equation (3.13) from equation (3.14) we can show that in this growing medium we have that net stress is proportional to net strain, where strain is taken to be the difference between the current distance between two points and the distance between the same two points under zero stress; the desired distance. Cells throughout the tumour are under radial tension due to the 'drag' effect of growth. For cells in the centre this effect is dominant over growth and thus these central cells are also under circumferential tension. Close to the edge the growth rate is almost constant. Therefore the drag effect is small compared to the effects of growth and thus the

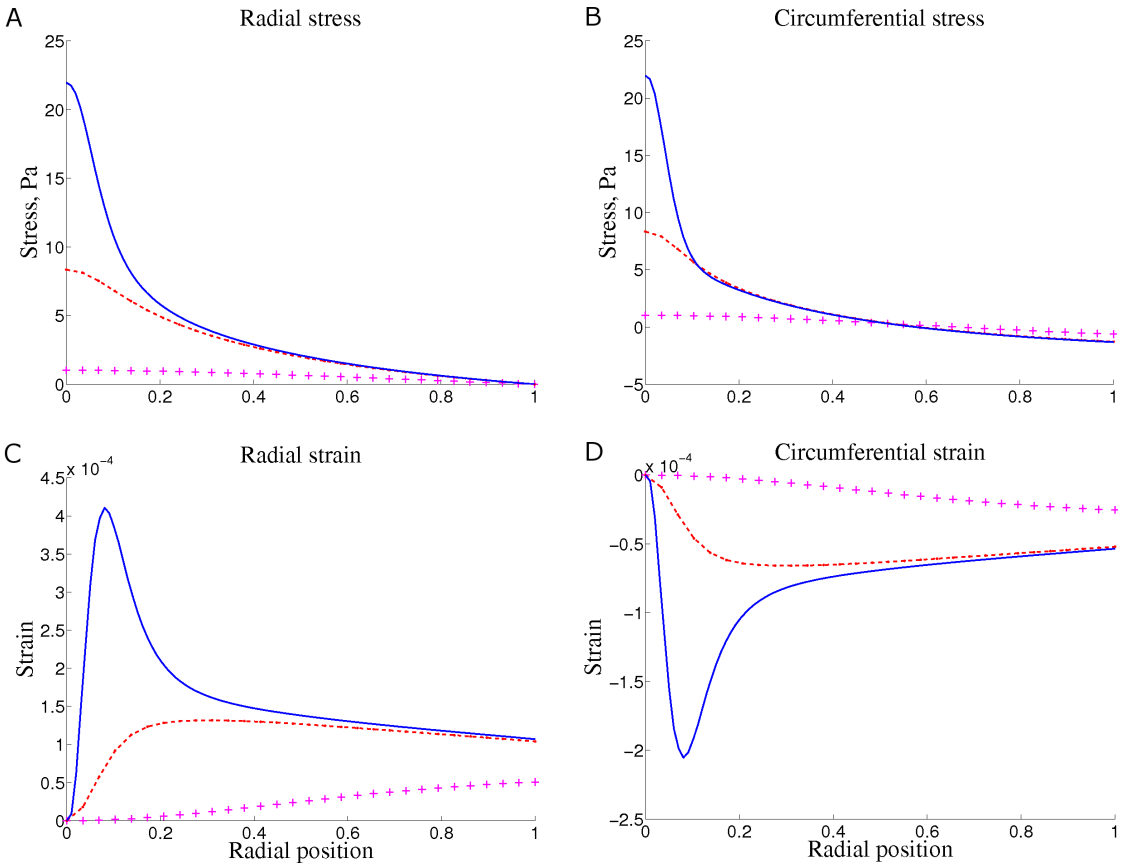

Figure 3.4: The radial stress (**A**), circumferential stress (**B**), radial stain (**C**) and circumferential strain (**D**) through a tumour spheroids of radii $250\mu m$ (+), $339\mu m$ (- - -) and $342\mu m$ (—) in which growth is highly sensitive to stress.

cells are under circumferential compression. Therefore regardless of location the cells are radially longer and circumferentially slimmer than their desired length. Thus the radial strain is positive and circumferential strain is negative, except at the centre, where the spherical properties of the tumour impose that the centre must always have zero circumferential strain.

The effects of necrosis are highly dependent on the sensitivity of growth to stresses. Necrosis can be thought of as acting as negative growth. Although the tumour spheroid is dominated by tension, by proliferating in the direction of maximum tension the cells are regulating this force. Necrosis causes an empty space to develop where the cell is dying. This space can not be left empty and thus cells are pulled in from the surrounding regions to fill it. Therefore necrosis will add to the tension forces within the spheroid, whilst growth will reduce them. The rate at which these forces build up will be dependent on how sensitive the direction of growth is to its surrounding stress field. A tumour whose growth is insensitive to stress will grow isotropically, pushing cells at random in towards the centre to replace the necrotic cells. A tumour whose growth is highly sensitive to stresses will grow anisotropically, preferring to

add daughter cells in the radial direction to relieve the radial tension caused by necrosis. This will have the effect of accelerating the increase in forces in the necrotic region. This can be best seen by studying the distribution of stress in Figure 3.2 for growth insensitive to stress against those in Figure 3.4 where the growth is highly sensitive to stress. The magnitude of the strains in the model where growth is highly sensitive to stress, Figure 3.4, are small but rapidly increasing. In the time take for the diameter of the spheroid to increase by just 3μm, a significant increase in stress can be seen.

This study has considered cells to be incompressible, therefore the size of the mechanical forces that develop during growth are dependent on the size of the sensitivity of growth parameter κ. As the value of κ increases the magnitude of the internal forces and strain decreases. Coinciding with this, the time scale on which these stresses and strains develop also decreases. Experimental work by Helmlinger *et al.* [73] compute the size of the stress induced by the tumour on its surrounding medium. Although no direct comparisons can be made, we can confirm that the magnitude of the stresses seen experimentally for a tumour of radius 200μm are similar to those modelled for moderately sensitive growth.

The aim of this model was to establish whether it was necessary to include effects of mechanical forces when modelling the growth of a MCTS. The conclusions from this work are dependent on how sensitive growth is to differences in circumferential and radial stress. Even in small tumours, insensitive growth produces large forces in both the circumferential and radial directions. These produce large strains and would therefore have a large, damaging affect on the tumour's growth and the cells within the spheroid. However, tumours are unlikely to grow isotropically to stress and thus this regime is unrealistic of what would be seen *in vitro*. The results of moderately sensitive growth before necrosis showed stresses with magnitude comparable to that found calculated from experimental work by Helmlinger *et al.* [73]. However the increase in stress due to the onset of necrosis produced forces higher than that seen *in vivo*. This would have damaging effects of the individual cells and cause the collapse of any potential vascular system. The closest representation of *in vivo* studies is modelled using highly sensitive growth. The results of highly sensitive growth show that for early growth, when there is no necrotic region, the stresses and strains are very small and thus can be neglected in a growth model. However the onset of necrosis causes the stress and strain to dramatically increase and thus can no longer be ignored. In this model the cell density must remain constant and thus the stresses rapidly increased. In *in vitro* growth the cells would detach themselves from their neighbours and thus the cell density would drop and become a region largely containing water and cell debris [163]. It can therefore be concluded that for moderate to highly sensitive growth, the growth of a spheroid can be modelled without the need for necessarily considering mechanical forces. However once necrosis has been initiated, they must be included and will potentially be a dominant mechanism.

3.7 Application to a sliced tumour

As with all modelling it is necessary to compare the theoretical results to those found experimentally. For the morphoelastic model of a tumour presented in this thesis, this shall be achieved by studying the deformation of a tumour spheroid that has been sliced in half, in view of comparing the theoretical results to those seen during *in vitro* experiments [150]. By slicing the tumour in half we break the internal forces that were previously in equilibrium. The tumour will therefore deform to relieve the internal stresses and regain an equilibrium state. In this work we only consider this as a theoretical study, the comparison to experimental results is beyond the scope of this thesis.

The growth of the tumour spheroid shall be modelled using the growth model presented in Section 2.5 and the mechanical forces will be derived using the model presented in Section 3.3. Once again we shall assume that the tumour is incompressible so that the growth and mechanical models can be solved separately. Both moderately and highly sensitive growth could be used as models for the tumours directional preference of growth. In this example we shall arbitrarily chose the tumour's growth to be moderately sensitive to stress and thus we consider $\kappa\mu$ to be order 1. The stress profile will be derived for a tumour with radius 500μm. The tumour shall be sliced through the centre into a perfect hemisphere. The parameters values required for this model will be the same as used in the morphoelastic model presented in Section 3.6.

We shall assume the tumour spheroid consists of a linearly elastic material, thus,

$$\sigma_{ij} \;=\; \lambda\,\delta_{ij}\,e_{kk} \;+\; 2\,\mu\,e_{ij}, \tag{3.48}$$

and once again body forces will be neglected such that,

$$\frac{\partial \sigma_{ij}}{\partial x_j} \;=\; 0. \tag{3.49}$$

Lastly we shall approximate strain using Cauchy's infinitesimal strain tensor,

$$e_{ij} \;=\; \frac{1}{2}\left(\frac{\partial u_i}{\partial x_j} + \frac{\partial u_j}{\partial x_i}\right), \tag{3.50}$$

where u is the displacement. By solving these three equations the deformation of the tumour given a known stress field can be derived.

We wish to study the deformation of a tumour spheroid with a known stress field, in which the stress along a given surface has been relieved. This will be done by considering the force that would be necessary to keep the sliced tumour in its pre-deformed hemispherical shape. The force required for this is equal and opposite to the forces on the sliced surface. Therefore

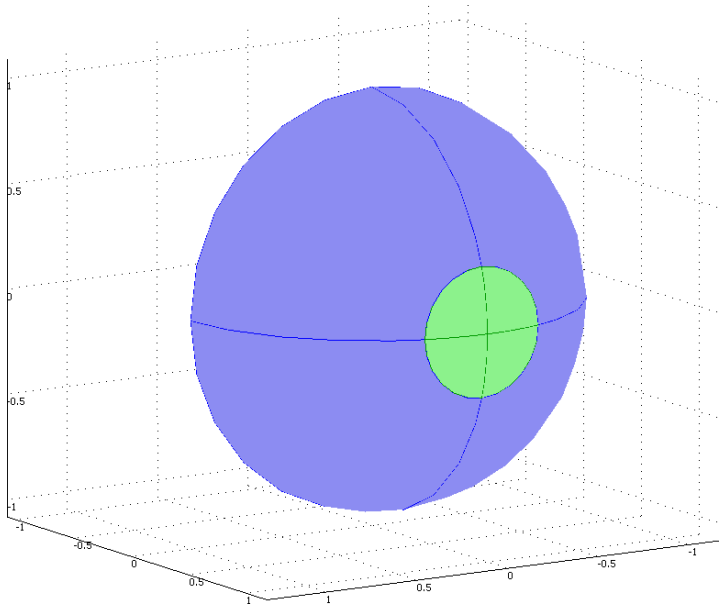

Figure 3.5: Geometry used for COMSOL simulation of sliced MCTS.

by applying this force to the flat surface of an unstressed hemisphere, of equal radius as the original tumour, we can derive the deformation that would take place by cutting a tumour in half.

3.8 Results

The results from the morphoelastic model, computed using MATLAB [174] and presented in Figure 3.6, for highly sensitive growth were first converted into a Cartesian coordinate system. The stress normal to the sliced surface was then imported into COMSOL Multiphysics [32], where it was applied to the boundary of the flat surface of a stress free hemisphere. Although the forces applied to the flat surface are radially symmetric, numerical differences resulted in solutions in which the hemisphere would spin or move laterally in space. Therefore an additional condition to hold the sphere stationary in space whilst allowing the surface to deform was added. This was achieved by constructing the hemisphere in two parts; the main volume and a circular region on the surface of the sphere, directly opposite the sliced surface. This small circular shell was pinned such that it could not move in any of the coordinate axes. The circular shell is small and relatively far away from the sliced surface and therefore this additional condition will have little effect on the results of the deformation of the tumour. The hemisphere and pinned circular shell are shown in Figure 3.5.

The results of the simulation derived in COMSOL [32] are shown in Figure 3.6. By slicing the tumour spheroid in two the forces that had previously kept the tumour in spherical symmetry

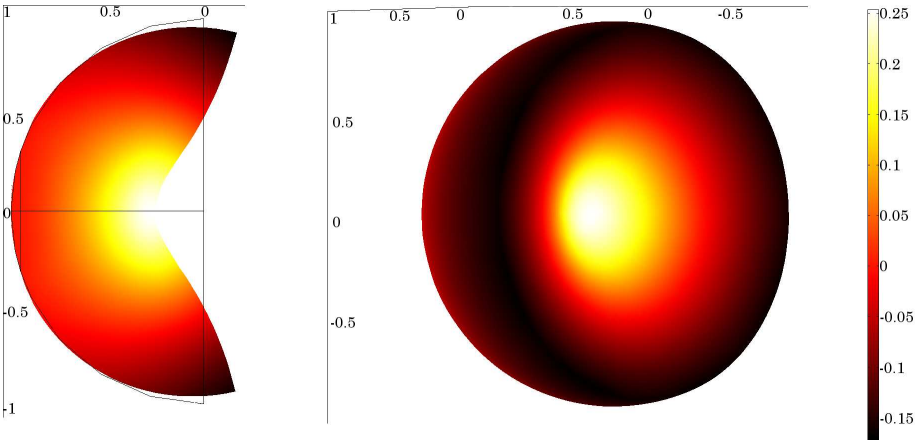

Figure 3.6: Nondimensional deformation of a sliced tumour spheroid with radius 500μm. The darkest regions indicate areas of greatest expansion, whilst the lightest region indicates greatest contraction.

were broken. Thus the hemispherical tumour deformed to its new equilibrium state. The tumour had been in radial tension due to growth. Upon relieving the forces, the tumour contracted, shown by a smaller distance between the centre of the flat surface and the outer curved surface. Prior to slicing the tumour was in circumferential tension in the centre and in compression close to the surface, where the rate of proliferation rate high. Thus, when sliced, the tension forces were relieved by the centre of the tumour contracting inwards and the compression forces relieved by expanding outwards near the surface. These deformations were calculated using the results of the morphoelastic model in the moderately sensitive limit at a tumour radius of 500μm. The forces at this time produced significant deformations, as graphically shown in the results given in Figure 3.6. As the necrotic core becomes larger the forces inside the tumour pulling it inward increase. This would have resulted in large deformations if the tumour were to be sliced in half.

This model highlights the importance of mechanical forces when modelling the growth of the a tumour spheroid and in particular the need to include the effects of stress once the tumour has become necrotic.

3.9 Discussion

A morphoelastic model of stress and strain was implemented and added to an existing growth model, showing that large internal forces may develop. In particular the onset of necrosis creates large tensile forces within the necrotic regions. The effects of how sensitive the growth of the tumour is to differences in the stress were studied and were shown to affect the magnitude of the forces and time scale on which they develop. This model of stresses and strains was

then used to determine the deformations in a sliced tumour, as an alternative way of showing the effects of mechanical forces. Both highlighted the need to include mechanical forces into a model of tumour spheroid growth, in particular when describing necrosis. Further work is required to identify how the stress field will affect growth. This model also considered tumours to be incompressible. Although this maybe a good initial approximation the effects of considering the tissue as a compressible material should be explored in the future to give a more accurate representation of a MCTS.

Chapter 4

Diffusion through a cellular region

4.1 Introduction

In this chapter we will derive continuum macroscopic equations for nutrient transport and consumption within a cellular region, by firstly considering individual cell characteristics on a microscopic scale. The effects of nutrient diffusion and consumption around a single cell will be studied before homogenization techniques are implemented to derive a model for the concentration of nutrients within a large population of cells. The aim of this chapter is to them determine whether the macroscopic equations used in Chapter 2 appropriately modelled diffusion and consumption through a cellular region.

A brief overview of homogenization theory will be given in Section 4.2 before a derivation of the equations for nutrient transport and consumption in a cellular region in Section 4.3. The resulting equations will then be applied to two example geometries in Section 4.4: Firstly an ellipsoid cell, showing how the shape of a cell can affect the transport of nutrients and secondly to a spherical cell, for which the resulting diffusion coefficient will be compared against that derived from *in vitro* experiments. This chapter will end with a brief discussion of the ideas that have been studied and a comparison to the equation for nutrient conservation used in Chapter 2. The methods used in this chapter are similar to the work presented in [29, 142, 152, 162].

4.2 Homogenization theory

Homogenization is a technique which uses the known properties of a regular microscopic setup to derive averaged equations on a macro-scale, by implementing the method of multiple scales.

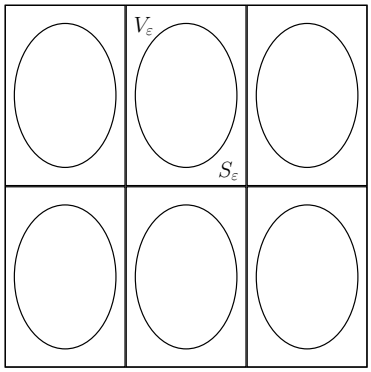

Figure 4.1: Schematic of the periodic array of cells.

The theory assumes that the local structure is periodic in all directions and that there are two distinct length scales in the problem. Tumour biology is a good application for this, as we have assumed the cell density to be constant throughout the spheroid and for the cells to be of constant size. Therefore the tumour spheroid has a uniform structure. There are two obvious length scales; the size of a cell, and the radius of the tumour.

By appropriate rescaling of the variables the global length scale can be scaled to be $\mathcal{O}(1)$, whilst the local length scale can be scaled to be of length ϵ, such that $\epsilon << 1$. By studying the limit as $\epsilon \to 0$ the original local equations can be used to derive global expressions. A multiple scales expansion is then used to equate powers of ϵ and derive a solution. In a well posed problem the local scale 'cell problem' will be derived at $\mathcal{O}(\epsilon)$ and the solvability equation will be derived at $\mathcal{O}\left(\epsilon^2\right)$.

4.3 Diffusion model

We will now use multiple scale homogenization theory to study the transport and consumption of nutrients in a cellular region. We will consider a periodic array of cells contained in bounded regions for which the total volume of the extracellular regions will be donated by V and the volume of each individual extracellular region will be denoted by V_ε. Cells will consume a general chemical species which will have concentration $\bar{C}$. This chemical species will be assumed to diffuse in the extracellular space around the cells and cell consumption will be accounted for by a flux condition on the boundary of each cell, S_ε. The region inside each cell will not be considered. The combination of all cell boundaries will be denoted by S. This setup is schematically shown in Figure 4.1. The governing equations in the extracellular region

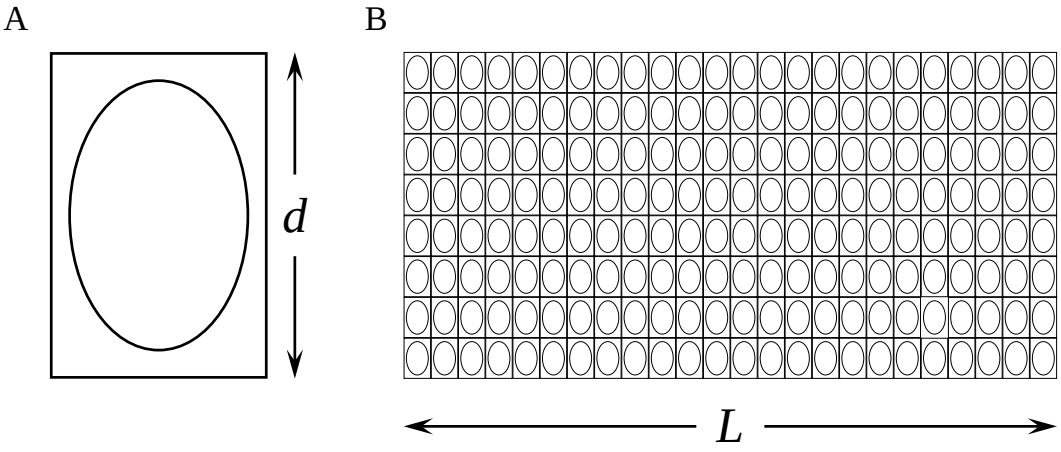

Figure 4.2: Schematic of the microscopic (**A**) and macroscopic (**B**) setup considered.

are,

$$\frac{\partial \bar{C}}{\partial \bar{t}} - D\nabla^2 \bar{C} = 0 \quad \text{in } V, \tag{4.1}$$

$$D\bar{\boldsymbol{\nabla}}\bar{C} \cdot \mathbf{n} = -k\,\bar{C} \quad \text{on } S, \tag{4.2}$$

where D is the diffusion coefficient of the chemical species considered, k is the rate of flux due to consumption and $\mathbf{n}$ is the outward normal. To aid analysis the model will be nondimensionalised. Length will be scaled on the macroscopic scale, L, shown in Figure 4.2. The concentration scaling of our generic species will be scaled with that in the initial surrounding medium, C_0. Time will be scaled to balance diffusion in equation (4.1). The nondimensional scalings are,

$$\bar{\boldsymbol{x}} = L\,\boldsymbol{x}, \qquad \bar{C} = C_0\,C \quad \text{and} \quad \bar{t} = \frac{L^2}{D}\,t. \tag{4.3}$$

The nondimensional system of equations gives,

$$\frac{\partial C}{\partial t} - \nabla^2 C = 0 \quad \text{in } V, \tag{4.4}$$

$$\boldsymbol{\nabla} C \cdot \mathbf{n} = -\left(\frac{kL}{D}\right) C \quad \text{on } S. \tag{4.5}$$

The effective consumption will be replaced such that,

$$\varepsilon^{\gamma}\alpha = \frac{kL}{D}, \tag{4.6}$$

where $\alpha = \mathcal{O}(1)$ and,

$$\varepsilon = \frac{d}{L}, \tag{4.7}$$

in which d is the length of a cell as shown in Figure 4.2. The modelling equations are,

$$\frac{\partial C}{\partial t} - \nabla^2 C = 0 \quad \text{in } V, \tag{4.8}$$

$$\boldsymbol{\nabla} C \cdot \mathbf{n} = -\varepsilon^{\gamma} \alpha C \quad \text{on } S. \tag{4.9}$$

We shall use the method of multiple scales, where the independent global and local length scales $\mathbf{x}$ and $\mathbf{y}$ are related to each other by,

$$\mathbf{x} = \varepsilon \mathbf{y}. \tag{4.10}$$

The expanded equations are,

$$\varepsilon^2 \frac{\partial C}{\partial t} - \left(\nabla_y^2 C + \varepsilon \boldsymbol{\nabla}_y \cdot \boldsymbol{\nabla}_x C + \varepsilon \boldsymbol{\nabla}_x \cdot \boldsymbol{\nabla}_y C + \varepsilon^2 \nabla_x^2 C\right) = 0 \quad \text{in } V_\varepsilon, \tag{4.11}$$

$$(\boldsymbol{\nabla}_y C + \varepsilon \boldsymbol{\nabla}_x C) \cdot \mathbf{n} = -\varepsilon^{\beta} \alpha C \quad \text{on } S_\varepsilon, \tag{4.12}$$

where,

$$\beta = \gamma + 1. \tag{4.13}$$

The variable C can then be expanded in powers of ε, such that,

$$C = C^{(0)}(\mathbf{x}, \mathbf{y}, t) + \varepsilon C^{(1)}(\mathbf{x}, \mathbf{y}, t) + \ldots \tag{4.14}$$

and taken to be periodic in $\mathbf{y}$.

The value of β will specify the order at which the consumption term in equation (4.12) appears. Physically, altering β changes the relative effects of cell consumption and diffusion on the concentration of the chemical species considered. We shall now consider the relevant limiting cases for β.

4.3.1 Case 1: $\beta < 2$

Firstly we shall consider the case where $\beta = 0$, to leading order, $\mathcal{O}\left(\varepsilon^0\right)$, equation (4.11) and (4.12) give,

$$-\nabla_y^2 C^{(0)} = 0 \quad \text{in } V_\varepsilon, \tag{4.15}$$

$$\boldsymbol{\nabla}_y C^{(0)} \cdot \mathbf{n} = -\alpha C^{(0)} \quad \text{on } S_\varepsilon. \tag{4.16}$$

Integrating equation (4.15) and imposing the corresponding boundary condition given in equation (4.16), gives,

$$\iint_{S_\varepsilon} C^{(0)}\, dS_\varepsilon = 0. \tag{4.17}$$

The first order, $\mathcal{O}(\varepsilon)$, system is given by,

$$-\left(\nabla_y^2 C^{(1)} + \boldsymbol{\nabla}_y \cdot \boldsymbol{\nabla}_x C^{(0)} + \boldsymbol{\nabla}_x \cdot \boldsymbol{\nabla}_y C^{(0)}\right) = 0 \quad \text{in } V_\varepsilon, \tag{4.18}$$

$$\left(\boldsymbol{\nabla}_y C^{(1)} + \boldsymbol{\nabla}_x C^{(0)}\right) \cdot \mathbf{n} = 0 \quad \text{on } S_\varepsilon. \tag{4.19}$$

This can be reduced to,

$$\iint_{S_\varepsilon} \boldsymbol{\nabla}_x C^{(0)} \cdot \mathbf{n}\, dS_\varepsilon = 0. \tag{4.20}$$

This implies that $\boldsymbol{\nabla}_x C^{(0)}$ is constant on the local scale and therefore to satisfy periodicity $C^{(0)}$ is also constant on the local scale. Thus equation (4.17) implies,

$$C^{(0)} \iint_{S_\varepsilon} dS_\varepsilon = 0, \tag{4.21}$$

which results in,

$$C^{(0)} = 0. \tag{4.22}$$

When $\beta = 1$, the model to leading order is given by,

$$-\nabla_y^2 C^{(0)} = 0 \quad \text{in } V_\varepsilon, \tag{4.23}$$

$$\boldsymbol{\nabla}_y C^{(0)} \cdot \mathbf{n} = 0 \quad \text{on } S_\varepsilon. \tag{4.24}$$

The solution to this leading order problem is that $C^{(0)}$ is constant on the local scale, *i.e.*

$$C^{(0)} = C^{(0)}(\mathbf{x}, t). \tag{4.25}$$

The first order system is,

$$-\left(\nabla_y^2 C^{(1)} + \boldsymbol{\nabla}_y \cdot \boldsymbol{\nabla}_x C^{(0)} + \boldsymbol{\nabla}_x \cdot \boldsymbol{\nabla}_y C^{(0)}\right) = 0 \quad \text{in } V_\varepsilon, \tag{4.26}$$

$$\left(\boldsymbol{\nabla}_y C^{(1)} + \boldsymbol{\nabla}_x C^{(0)}\right) \cdot \mathbf{n} = -\alpha C^{(0)} \quad \text{on } S_\varepsilon. \tag{4.27}$$

Equation (4.26) can be integrated and then expanded to give,

$$-\iiint_{V_\varepsilon} \left(\nabla_y^2 C^{(1)} + \boldsymbol{\nabla}_y \cdot \boldsymbol{\nabla}_x C^{(0)}\right) dV_\varepsilon - \iiint_{V_\varepsilon} \boldsymbol{\nabla}_x \cdot \boldsymbol{\nabla}_y C^{(0)}\, dV_\varepsilon = 0 \quad \text{in } V_\varepsilon. \tag{4.28}$$

Applying the divergence theorem to equation (4.28) and imposing that $C^{(0)}$ is constant on the

local scale, equation (4.25), gives,

$$-\iint_{S_\varepsilon}\left(\boldsymbol{\nabla}_y C^{(1)} + \boldsymbol{\nabla}_x C^{(0)}\right)\cdot\mathbf{n}\,dS_\varepsilon = 0 \quad \text{in } V_\varepsilon. \tag{4.29}$$

The boundary condition, given in equation (4.27), simplifies equation (4.29), to give,

$$\alpha C^{(0)}\iint_{S_\varepsilon} dS_\varepsilon = 0 \quad \text{in } V_\varepsilon. \tag{4.30}$$

Thus the solution for $C^{(0)}$ is,

$$C^{(0)} = 0, \tag{4.31}$$

which is the same result as derived for when $\beta = 0$.

Physically $C^{(0)} = 0$ describes the situation where by cell consumption is occurring at a rate much greater than that of diffusion, such that diffusion can not meet the consumption needs of the cells. Therefore the cells are rapidly consuming the chemical species around them and thus the concentration of the chemical specials is zero over all space and for all time. In dimensional units $\beta < 2$ describes the situation where by

$$\frac{kL}{D} = \varepsilon^{\beta-1} > \frac{d}{L}\alpha, \tag{4.32}$$

which implies,

$$k > \frac{Dd\alpha}{L^2}. \tag{4.33}$$

Thus consumption will dominate nutrient transport and the species concentration will be zero to leading order.

4.3.2 Case 2: $\beta = 2$

We shall now consider the case where $\beta = 2$. To leading order the model is given by,

$$-\nabla_y^2 C^{(0)} = 0 \quad \text{in } V_\varepsilon, \tag{4.34}$$

$$\boldsymbol{\nabla}_y C^{(0)}\cdot\mathbf{n} = 0 \quad \text{on } S_\varepsilon. \tag{4.35}$$

The only solution to this problem is when C is constant on the local scale, *i.e.*

$$C^{(0)} = C^{(0)}(\mathbf{x}, t). \tag{4.36}$$

To first order,

$$-\left(\nabla_y^2 C^{(1)} + \boldsymbol{\nabla}_y \cdot \boldsymbol{\nabla}_x C^{(0)} + \boldsymbol{\nabla}_x \cdot \boldsymbol{\nabla}_y C^{(0)}\right) = 0 \quad \text{in } V_\varepsilon, \tag{4.37}$$

$$\left(\boldsymbol{\nabla}_y C^{(1)} + \boldsymbol{\nabla}_x C^{(0)}\right) \cdot \mathbf{n} = 0 \quad \text{on } S_\varepsilon. \tag{4.38}$$

By noting that $C^{(0)}$ is only a function of the global scale, this first order system can be simplified to,

$$\nabla_y^2 C^{(1)} = 0 \quad \text{in } V_\varepsilon, \tag{4.39}$$

$$\left(\boldsymbol{\nabla}_y C^{(1)} + \boldsymbol{\nabla}_x C^{(0)}\right) \cdot \mathbf{n} = 0 \quad \text{on } S_\varepsilon. \tag{4.40}$$

To solve the first order problem for $C^{(1)}$, equations (4.39) and (4.40), we exploit the linearity and use separation of variables to assume a solution of the form,

$$C^{(1)} = -\boldsymbol{\nabla}_x C^{(0)}(\boldsymbol{x}, t) \cdot \boldsymbol{\chi}(\boldsymbol{y}), \tag{4.41}$$

where $\boldsymbol{\chi}$ is an unknown vector function, periodic in $\mathbf{y}$, and only a function of the local cell problem. The first order problem can then be written as,

$$\nabla_y^2 \left(\boldsymbol{\nabla}_x C^{(0)} \cdot \boldsymbol{\chi}\right) = 0 \quad \text{in } V_\varepsilon, \tag{4.42}$$

$$\boldsymbol{\nabla}_y \left(\boldsymbol{\nabla}_x C^{(0)} \cdot \boldsymbol{\chi}\right) \cdot \mathbf{n} = \boldsymbol{\nabla}_x C^{(0)} \cdot \mathbf{n} \quad \text{on } S_\varepsilon, \tag{4.43}$$

which, using the Einstein summation convention, can be simplified to,

$$\nabla_y^2 \chi_i = 0 \quad \text{in } V_\varepsilon, \tag{4.44}$$

$$\frac{\partial \chi_i}{\partial y_j} n_j = n_i \quad \text{on } S_\varepsilon. \tag{4.45}$$

This system of equations can then be solved numerically.

The resulting expression for $C^{(1)}$ in terms of $C^{(0)}$ can then be substituted into the second order problem

$$\frac{\partial C^{(0)}}{\partial t} - \left(\nabla_y^2 C^{(2)} + \boldsymbol{\nabla}_y \cdot \boldsymbol{\nabla}_x C^{(1)} + \boldsymbol{\nabla}_x \cdot \boldsymbol{\nabla}_y C^{(1)} + \nabla_x^2 C^{(0)}\right) = 0 \quad \text{in } V_\varepsilon, \tag{4.46}$$

$$\left(\boldsymbol{\nabla}_y C^{(2)} + \boldsymbol{\nabla}_x C^{(1)}\right) \cdot \mathbf{n} = -\alpha\, C^{(0)} \quad \text{on } S_\varepsilon. \tag{4.47}$$

Integrating equation (4.46) gives,

$$\frac{\partial C^{(0)}}{\partial t} |V_\varepsilon| - \iiint_{V_\varepsilon} \nabla_y^2 C^{(2)} + \boldsymbol{\nabla}_y \cdot \boldsymbol{\nabla}_x C^{(1)} + \boldsymbol{\nabla}_x \cdot \boldsymbol{\nabla}_y C^{(1)}\, dV_\varepsilon - \nabla_x^2 C^{(0)} |V_\varepsilon| = 0, \tag{4.48}$$

where $|V_\varepsilon|$ is the volume of the region surrounding the cell. Rewriting in terms of the expression for $C^{(1)}$, defined in equation (4.41), equation (4.48) gives,

$$\frac{\partial C^{(0)}}{\partial t}\,|V_\varepsilon| - \iiint_{V_\varepsilon} \nabla_y^2 C^{(2)} - \boldsymbol{\nabla}_y \cdot \boldsymbol{\nabla}_x \left(\boldsymbol{\nabla}_x C^{(0)} \cdot \boldsymbol{\chi}\right) - \boldsymbol{\nabla}_x \cdot \boldsymbol{\nabla}_y \left(\boldsymbol{\nabla}_x C^{(0)} \cdot \boldsymbol{\chi}\right) dV_\varepsilon - \nabla_x^2 C^{(0)}\,|V_\varepsilon| \;=\; 0, \tag{4.49}$$

with a boundary condition given such that,

$$\left(\boldsymbol{\nabla}_y C^{(2)} \;-\; \boldsymbol{\nabla}_x \left(\boldsymbol{\nabla}_x C^{(0)} \cdot \boldsymbol{\chi}\right)\right) \cdot \mathbf{n} \;=\; -\,\alpha\, C^{(0)}. \tag{4.50}$$

Rearranging equation (4.49) and applying the divergence theorem gives,

$$\begin{aligned} \frac{\partial C^{(0)}}{\partial t}\,|V_\varepsilon| \quad &- \quad \iint_{S_\varepsilon} \left(\boldsymbol{\nabla}_y C^{(2)} \;-\; \boldsymbol{\nabla}_x \left(\boldsymbol{\nabla}_x C^{(0)} \cdot \boldsymbol{\chi}\right)\right) \cdot \mathbf{n}\, dS_\varepsilon \\ &+ \quad \iiint_{V_\varepsilon} \boldsymbol{\nabla}_x \cdot \boldsymbol{\nabla}_y \left(\boldsymbol{\nabla}_x C^{(0)} \cdot \boldsymbol{\chi}\right) dV_\varepsilon \;-\; \nabla_x^2 C^{(0)}\,|V_\varepsilon| \;=\; 0. \end{aligned} \tag{4.51}$$

Implementing the boundary condition, given in equation (4.50), into equation (4.51) results in,

$$\frac{\partial C^{(0)}}{\partial t}\,|V_\varepsilon| \;+\; \alpha\, C^{(0)}\,|S_\varepsilon| \;+\; \iiint_{V_\varepsilon} \boldsymbol{\nabla}_x \cdot \boldsymbol{\nabla}_y \left(\boldsymbol{\nabla}_x C^{(0)} \cdot \boldsymbol{\chi}\right) dV_\varepsilon \;-\; \nabla_x^2 C^{(0)}\,|V_\varepsilon| \;=\; 0. \tag{4.52}$$

where $|S_\varepsilon|$ is the magnitude of surface area of a cell. Rewriting in component form this gives,

$$\frac{\partial C^{(0)}}{\partial t}\,|V_\varepsilon| \;+\; \frac{\partial^2 C^{(0)}}{\partial x_i \partial x_j} \iiint_{V_\varepsilon} \frac{\partial \chi_i}{\partial y_j}\, dV_\varepsilon \;-\; \frac{\partial^2 C^{(0)}}{\partial x_i^2}\,|V_\varepsilon| \;=\; -\alpha\, C^{(0)}\,|S_\varepsilon|\,, \tag{4.53}$$

We introduce the tensor K by defining,

$$\iiint_{V_\varepsilon} \frac{\partial \chi_i}{\partial y_j}\, dV_\varepsilon \;=\; K_{ij} \tag{4.54}$$

which allows equation (4.53) to be written as,

$$\frac{\partial C^{(0)}}{\partial t}\,|V_\varepsilon| \;+\; \left(\frac{\partial^2 C^{(0)}}{\partial x_i \partial x_j} K_{ij} \;-\; \frac{\partial^2 C^{(0)}}{\partial x_i^2}\,|V_\varepsilon|\right) \;=\; -\alpha\, C^{(0)}\,|S_\varepsilon|\,. \tag{4.55}$$

This is the solvability equation for $C^{(0)}$ and can be used to model cell consumption on a macroscopic scale for a given geometric set-up. Therefore, dimensionally, this will occur when the rate of species flux into the cells is the same order as $\frac{Dd\alpha}{L^2}$.

4.3.3 Case 3: $\beta \geq 3$

The solution to the problem for $\beta \geq 3$ is equivalent to the case where $\beta = 2$ up to and including first order terms. At second order the boundary condition changes to be,

$$\left(\boldsymbol{\nabla}_y C^{(2)} + \boldsymbol{\nabla}_x C^{(1)}\right) \cdot \mathbf{n} = 0 \quad \text{on } S_\varepsilon, \tag{4.56}$$

which imposes no flux through the boundary. Therefore the solution to the second order problem is equivalent to setting α to zero in the casee for $\beta = 2$. Thus following the workings in Section 4.3.2 the solvability equation for $C^{(0)}$ is,

$$\frac{\partial C^{(0)}}{\partial t} |V_\varepsilon| + \left(\frac{\partial^2 C^{(0)}}{\partial x_i \partial x_j} K_{ij} - \frac{\partial^2 C^{(0)}}{\partial x_i^2} |V_\varepsilon| \right) = 0, \tag{4.57}$$

where K is the permeability tensor as defined in equation (4.54). For $\beta \geq 3$ the sink term in the boundary condition does not come in until the 'β' order problem. By which point the solvability equation for $C^{(0)}$ has been derived. Thus for $\beta \geq 3$ the chemical species in question will be diffusing through the structure at such a rate that the consumption by cells is negligible.

4.4 Application to tumours

We shall now consider the physical implications of our alternative conservation equation for the case when consumption balances diffusion. Firstly we shall consider the geometric effects by considering a region of ellipsoid cells and show how the shape of a cell can affect the transport of a chemical species. Secondly we will derive the effective diffusion coefficient for a region of spherical cells packed into a region with density equivalent to that of a tumour. The resulting effective diffusion coefficient will then be compared to experimental work.

4.4.1 Example 1: Ellipsoid cells

To show the effects of the geometry of a cellular region on the transport of nutrients, we consider a region of ellipsoid cells. Each cell will have dimensionless radii 2 along the y_1 axis and radius 1 along the y_2 and y_3 axes and shall be contained in a rectangular box with dimensions 6, 4, 4 in the direction y_1, y_2 and y_3 respectively. The consumption rate of the nutrient considered will be said to balance diffusion such that $\beta = 2$. The consumption of the nutrient will be modelled by the flux of nutrients through the surface of each cell and the concentration of the nutrient will be governed by conservation of mass in the surrounding fluid.

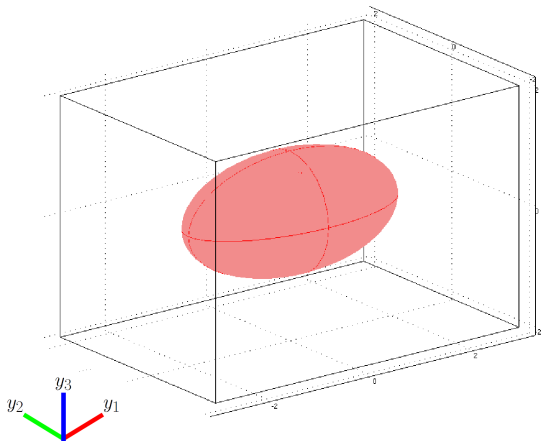

Figure 4.3: Ellipsoid cell contained inside periodic region implemented in COMSOL simulation.

Transport through the cells will not be considered and in the outer region we shall assume the transport to be diffusion dominated. Therefore the system can be modelled by equation (4.1) with the boundary condition as given by equation (4.2). Periodic boundary conditions will be applied to the box such that the flux of the nutrient is continuous across the boundaries of the box. The solvability equation for the leading order problem is therefore as derived in Section 4.3.2,

$$\frac{\partial C}{\partial t}\left|V_\varepsilon\right| + \left(\frac{\partial^2 C}{\partial x_i \partial x_j}K_{ij} - \frac{\partial^2 C}{\partial x_i^2}\left|V_\varepsilon\right|\right) = -\alpha\, C\left|S_\varepsilon\right|, \tag{4.58}$$

given that

$$\iiint_{V_\varepsilon} \frac{\partial \chi_i}{\partial y_j}\, dV_\varepsilon = K_{ij}, \tag{4.59}$$

and

$$\nabla_y^2 \chi_i = 0 \quad \text{in } V_\varepsilon, \tag{4.60}$$

$$\frac{\partial \chi_i}{\partial y_j} n_j = n_i \quad \text{on } S_\varepsilon. \tag{4.61}$$

Equations (4.60) and (4.61) were solved numerically using COMSOL Multiphysics [32] for the physical setup as described above and shown in Figure 4.3. The solutions for χ_1, χ_2 and χ_3 are shown in Figure 4.4. Due to the Neumann boundary condtion imposed on this system there will be no unique solution. Therefore to obtain a single solution an extra condition was imposed which stated that χ on the surfaces normal to the component considered would be equal to zero, *e.g.*

$$\chi_1 = 0 \quad \text{on } y_1 = -3 \text{ and } y_1 = 3. \tag{4.62}$$

The results for χ_i were then used to derived the permeability tensor, K_{ij}. The results of which

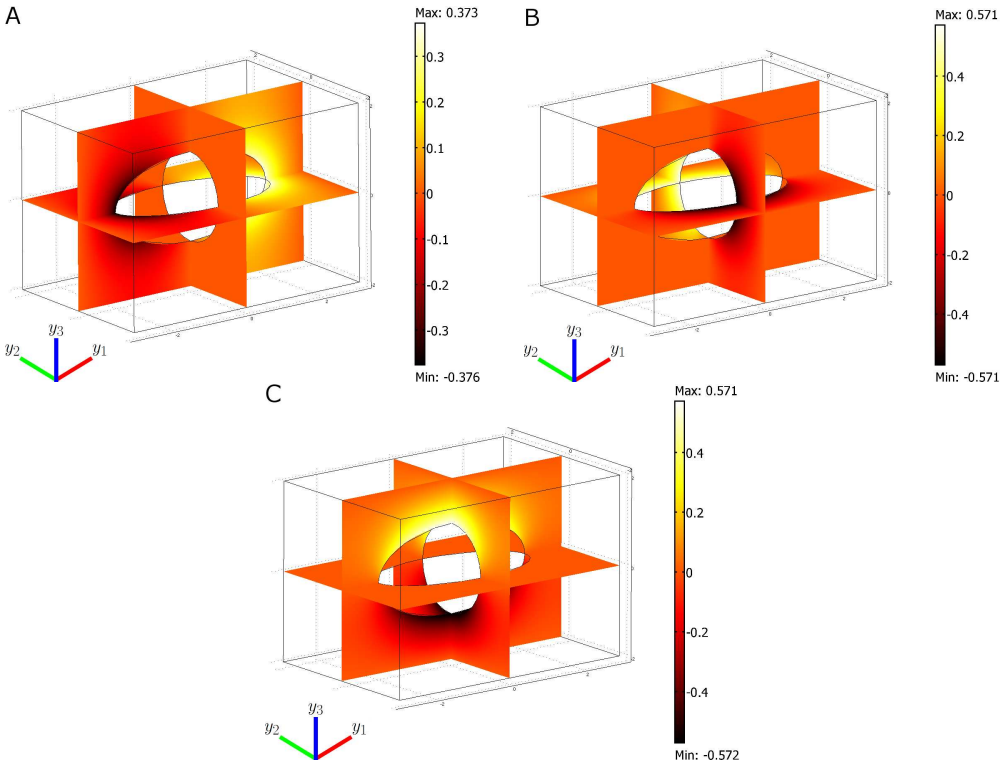

Figure 4.4: Graphical solutions to the first order problem for χ_i. Plot **A** shows the solution to χ_1, **B** to χ_2 and **C** to χ_3.

are such that,

$$K_{ij} = \iiint_{V_\varepsilon} \frac{\partial \chi_i}{\partial y_j} \, dV_\varepsilon = \begin{pmatrix} 1.667 & 3.311 \cdot 10^{-5} & -1.478 \cdot 10^{-4} \\ -6.213 \cdot 10^{-5} & 4.991 & 7.665 \cdot 10^{-5} \\ 1.315 \cdot 10^{-4} & -1.878 \cdot 10^{-6} & 4.991 \end{pmatrix}. \tag{4.63}$$

Due to the symmetry of the system the off diagonal values should be zero. In the above solution the values are small, but non zero, due to numerical errors. Therefore these entries in the permeability tensor will be neglected. The resulting tensor can be substituted into equation (4.58) to give a final leading order equation for the effective diffusion and consumption of nutrients through a periodic region of ellipsoid cells.

$$\frac{\partial C}{\partial t} - \frac{\partial}{\partial x_i}\left(\frac{\partial C}{\partial x_i} - \widetilde{K}_{ij}\frac{\partial C}{\partial x_j}\right) = -\alpha \frac{|S_\varepsilon|}{|V_\varepsilon|} C, \tag{4.64}$$

where,

$$\widetilde{K}_{ij} = \begin{pmatrix} 1.90 & 0 & 0 \\ 0 & 5.70 & 0 \\ 0 & 0 & 5.70 \end{pmatrix} \cdot 10^{-2}. \tag{4.65}$$

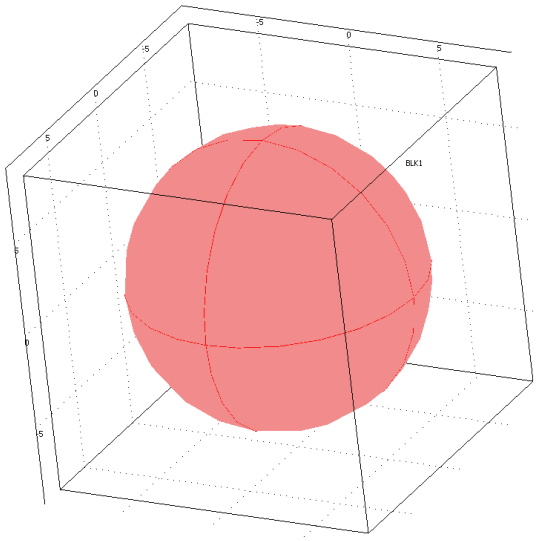

Figure 4.5: Schematic of a spheroid cell contained inside its periodic region.

This differs from a conventional macroscopic approach in that diffusion now has a directional preference. The permeability tensor gives the resistance to the movement in the direction of interest. Thus a zero in a diagonal entry of $\widetilde{K}$ would describe unimpeded diffusion at a rate equal to that in a fluid with no cells. Whilst a value of one would impose that there was no diffusion in that direction. Thus in our example the diffusion will be fastest along the length of the cells, in the direction y_1, whilst being a factor of three slower in either the y_2 or y_3 directions. However the magnitude of the values in this permeability tensor are small. This is due to the relatively small size of the cells compared to the surrounding region. This imposes that the effects on the rate of diffusion are small. The surface area to volume ratio is approximately 0.25. This results in a relatively high level of consumption of nutrients. Cells packed at a higher density or with a larger surface area would cause the nutrients to be consumed at a faster rate.

4.4.2 Example 2: Spherical cells

We shall now derive the effective diffusion coefficient of a chemical species diffusing through a MCTS. The tumour cells shall be assumed spherical, with radius r and packed at constant density ρ. The numerical value of ρ is given in Table 2.3 and we shall assume the radius of a cell to be $7.5\mu m$. A schematic of the setup used is given in Figure 4.5. In this example we only wish to study the effects of transport, therefore consumption shall be neglected and effectively we consider the case where $\beta \geq 3$. We will consider glucose as our example nutrient and thus transport will only take place in the extracellular regions. Therefore the leading

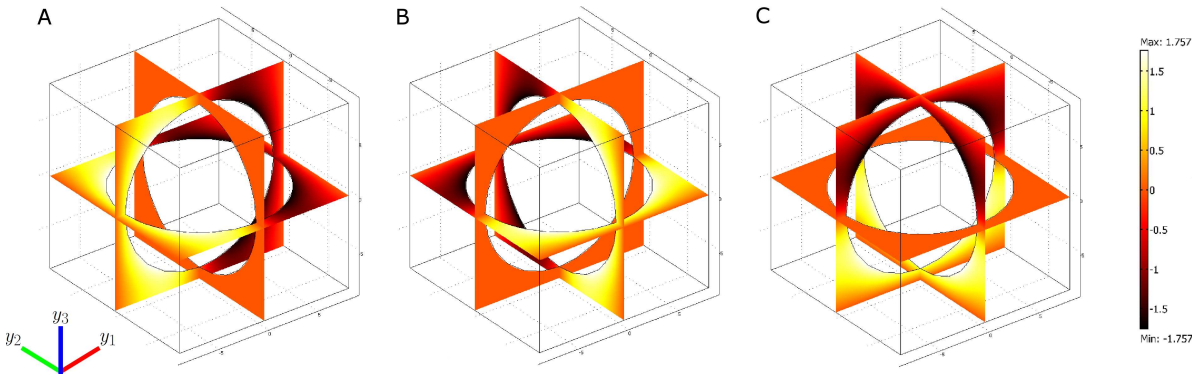

Figure 4.6: Graphical solutions to the first order problem for χ_i. Plots **A**, **B** and **C** show the solutions to χ_1, χ_2 and χ_3 respectively.

order solvability equation for the concentration of glucose is given by,

$$\frac{\partial \bar{C}}{\partial \bar{t}} - D\frac{\partial}{\partial \bar{x}_i}\left(\frac{\partial \bar{C}}{\partial \bar{x}_i} - \frac{K_{ij}}{|\bar{V}_\varepsilon|}\frac{\partial \bar{C}}{\partial \bar{x}_j}\right) = 0. \tag{4.66}$$

The permeability tensor K is again defined such that

$$K_{ij} = \iiint_{V_\varepsilon} \frac{\partial \chi_i}{\partial y_j}\, dV_\varepsilon \tag{4.67}$$

and

$$\nabla_y^2 \chi_i = 0 \quad \text{in } V_\varepsilon, \tag{4.68}$$

$$\frac{\partial \chi_i}{\partial y_j} n_j = n_i \quad \text{on } S_\varepsilon. \tag{4.69}$$

The solution for χ and the resulting permeability tensor K were solved using COMSOL Multiphysics [32]. The geometric setup is shown in Figure 4.5 and the resulting solutions for χ_i are shown in Figure 4.6. Similar to the case of the ellipsoid cell, an extra boundary condition was imposed on the surfaces normal to the component considered, that stated that χ equals zero. The resulting permeability tensor was then derived such that,

$$K_{ij} = \begin{pmatrix} 5.14 & 0 & 0 \\ 0 & 5.14 & 0 \\ 0 & 0 & 5.14 \end{pmatrix} \cdot 10^{-16}. \tag{4.70}$$

Due to the symmetry of the problem the diagonal terms are identical whilst the off diagonal

terms are zero. Thus the solvability equation can be re-written as,

$$\frac{\partial \bar{C}}{\partial \bar{t}} \; - \; D_{new} \frac{\partial^2 \bar{C}}{\partial \bar{x}_i^2} \; = \; 0, \tag{4.71}$$

where,

$$D_{new} \; = \; D \left(1 - \frac{5.14 \cdot 10^{-16}}{\frac{1}{\rho} - \frac{4}{3}\pi r^3} \right). \tag{4.72}$$

By substituting in the diffusion coefficient of glucose in a fluid, given in [104] to be $9.25 \cdot 10^{-10}\, m^2 s^{-1}$, and the known values for r and ρ, we derive a new effective diffusion coefficient for glucose inside a tumour spheroid, such that,

$$D_{new} \; = \; 7.77 \cdot 10^{-10}\, m^2 s^{-1}. \tag{4.73}$$

The diffusion coefficient of glucose in a tumour was also derived experimentally by Casciari *et al.* [23] and given to be $1.1 \cdot 10^{-10}\, m^2 s^{-1}$. The difference in the theoretical and experimental diffusion coefficients could be due to a number of reasons.

In this study we have studied the transport around a spherical cell, distributed periodically in space in which the periodic region is a cube encapsulating a single cell. This structure was used as a simple representation of a tumour, which could be easily solved using numerical methods. In practice each cells will not be centred in a cube, but will be enclosed in a face centred cubic lattice [33]. A two dimensional representation of the system used in this study is shown alongside the more efficient face centred cubic lattice arrangement in Figure 4.7. The problem of efficiently packing cells has been widely studied in literature [33, 81]. By optimally arranging the cells it can be shown that the packing density of cells can reach $\pi/\sqrt{18} \approx 0.7405$ [33]; this is compared to the cubed arrangement which has a packing density of $\pi/6 \approx 0.524$. This increase in cell density would reduce the space available for diffusion. However in our example of tumour spheroids the packing density of cells is known to be approximately 0.355. Therefore of greater relevance to this study is the tortuosity of the geometry. As shown in Figure 4.7, the cubic arrangement provides large cylindrical 'pipes' that provide efficient and fast transport of nutrients in all dimensions. The alternative arrangement; illustrated by hexagons in two dimensions, provides a tortuous path for nutrient transport. The glucose would have to diffuse around the cells, travelling a greater distance than in the cubed arrangement. This would reduce the effective diffusion coefficient. However the geometry makes this problem harder to solve numerically and is thus not included in this thesis. Along with the structural layout of cells we have also assumed the cells to be of equal size and uniformly distributed. Larger cells, or a higher packing density, would reduce the extracellular volume available for the glucose to diffuse through and thus decrease the rate of diffusion. Similarly a non-uniform distribution of cells would provide greater resistance to glucose transport.

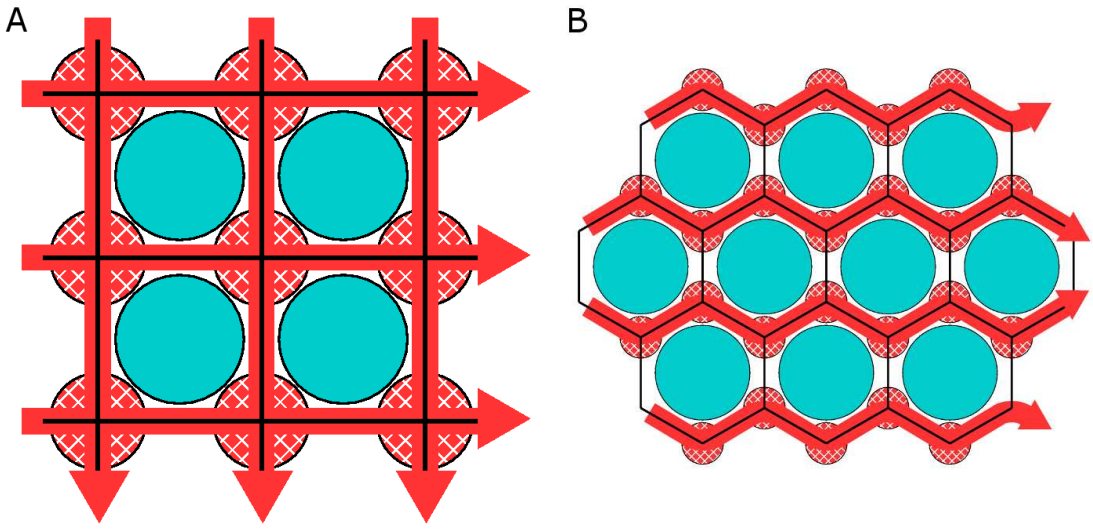

Figure 4.7: Two dimensional schematic of the cubic (**A**) and face centred cubic lattice (**B**) packing arrangements. Arrowed lines and hashed circles indicate the flow of nutrients.

4.5 Discussion

In this chapter we have studied the effects of species transport and consumption on the concentration of a nutrient surrounding a cell. Using homogenization theory we have then shown how these microscopic effects can be used to derive continuum equations on a macroscopic scale. The resulting macroscopic equations are shown to give directional preference for the diffusion of nutrients due to the geometry and arrangement of the cells. The consumption of nutrients was modelled by imposing a flux of nutrients across the cell boundary. The overall consumption rate was thus shown to be relative to the extracellular volume and the surface area of the cells. When compared to experimental data this approach was shown to lower the effective diffusion rate by an insufficient amount. Therefore at present it is more accurate to model the transport of nutrients using the experimental data and equations implemented in Chapter 2. In the future, further investigation is required into cell characteristics, cell geometry and the make up of the extracellular matrix to generate a theoretical model that simulates what is seen in experiments with a greater degree of accuracy.

Chapter 5

Modelling of engineered orthopaedic tissue

5.1 Introduction

The process of biologically engineering tissue to replace degraded or injured tissue in the body is a rapidly expanding area. In the developed world, it is likely that one in every five people over the age of sixty-five will benefit from organ replacement technology, creating a demand for engineered products that was a billion dollar industry in 2008 alone [90].

Tissue engineering uses cells extracted from living organisms to grow biological material *in vitro* with the aim of replacing damaged or degenerate *in vivo* tissue. Unlike organ transplants, engineered tissues can be designed and made compatible for individual patients, reducing the risk of rejection or infections. Engineered tissues also provide a more ethical basis for testing drugs and medical treatments.

Tissues have been engineered for many different uses. Example areas include bone, blood vessels, heart valves, and skin [144, 175]. This study will look at the growth of cartilage. Articular cartilage provides a soft, shock absorptive layer between joints that is low in friction and reduces the stress and wear on bones [106, 195]. It is estimated that ten thousand people a year in the UK alone experience cartilage damage that is severe enough to require treatment [133]. Cartilage is often damaged as the result of gradual degradation over time or as the result of a sudden and direct impact. The simplicity of the cartilage structure makes it an ideal tissue to model mathematically. Many engineered tissues suffer from the inability to recreate vascular networks, thus limiting the blood supply and growth [90]. Cartilage is non vascularised and so is not potentially limited in this way. This enables *in vitro* growth to accurately replicate what is seen *in vivo*.

The aim of this chapter is to explain the growth characteristics of a layer of chondrocytes. To begin a brief outline of the structural and functional properties of tissue and cartilage will be given in Section 5.1.1. This will be followed by a literature review of the experimental progress made in the field of tissue engineering as well as in the mathematical modelling of tissue engineered constructs. This review, given in Section 5.2, will also explore the metabolic pathways that govern tissue cells. The model presented in this chapter has been constructed with particular focus on monolayer cultures of cartilage. A comparison of the mathematical predictions is made to experimental data provided by Jos Malda and Wouter Schuurman working at Utrecht University and University Medical Center Utrecht, The Netherlands [114]. The experimental procedures used are described in Section 5.3 and analysis of the resulting data is given in Section 5.4. This analysis then forms the basis for the mathematical model laid out in Section 5.5. The results of this model are then presented and comparisons are made to experimental data in Section 5.7. These results and the potential for developing the model in the future is discussed in Section 5.8.

5.1.1 Tissue and cartilage

We shall now give a brief overview of the properties of tissue, with particular focus on cartilage. The summary has been based on work presented in [169, 175], but further information on cartilage and chondrocytes can be found in [13, 168], collagen and proteoglycans in [44, 154] and reviews from a clinical viewpoint in [16, 83, 105, 112].

There are four types of tissue; epithelial tissue, connective tissue, muscular tissue and nervous tissue. Each tissue type is used for differing purposes and thus has its own characteristics. Epithelial tissue is used to cover surfaces throughout the body and forms many of the glands found within the body. Connective tissue protects and supports the body and the organs within. This tissue type also binds organs together and in certain cases stores energy as fat. Muscular tissue provides the forces required for the body to move. This can be on a large scale such as the physical movement of the human body, or on a smaller scale such as in the beating of a heart. Finally nervous tissue detects changes to the body both internally and externally and thus regulates the body's conditions. Cartilage is classified as a connective tissue and thus we shall focus our discussion on this tissue type.

Connective tissue consists of three elements, cells, extracellular matrix (ECM) and interstitial fluid. The cells within connective tissue can be divided into two groups; immature cells and mature cells. Immature cells have the capacity to undergo mitosis as well as produce ECM. In cartilage these immature cells are called chondroblasts and once they have produced the necessary amount of ECM required of them, they differentiate into mature cells. In cartilage the mature cells are known as chondrocytes. Mature cells have a lower capacity to proliferate

and create ECM than immature cells. Instead their main role is in maintaining the matrix surrounding them [175].

The ECM can be broken up into two parts; these are ground substance and fibres. The ground substance is the material that fills the spaces between the cells and the fibres. In doing so it holds the cells in place, stores water and provides the medium by which the nutrients and other substances can diffuse through. The ground substance also consists of a large variety of large organic molecules that are a combination of proteins and polysaccharides. The collectives name given to the polysaccharides is glycosaminoglycans, more commonly known as GAGs. With the exception of hyaluronic acid the GAGs then combine with the proteins to form large molecules known as proteoglycans, where the GAGs 'project from the proteins like the bristles on a bottle brush' [175]. The hyaluronic acid then binds the proteoglycans and surrounding fluid together to form larger structures. The fibres, ground substance and cells are then bound together by the protein fibronectin.

Embedded in the ground substance are the fibres. The role of the fibres is to provide strength and support and they can be thought of as providing the scaffold to the connective tissue. The fibres come as one of three types; collagen fibres, elastic fibres and reticular fibres. Collagen fibres are very strong, inextensible and can withstand large tensile forces. However the fibres are not stiff, which allows the tissue to be flexible. Collagen fibres can form ropes as found in ligaments and tendons or flat sheets as in cartilage. Collagen fibres in cartilage have a large capacity to retain water, thus making cartilage resistant to impact, where as collagen in bone has a much smaller water content and thus allows bone to be more rigid. Although the collagen fibres vary in size they often group together to form bundles between five and two hundred nanometres in diameter [169]. It is these bundles that provide the tissue with its strength. Elastic fibres have a much smaller diameter than collagen fibres and form large networks within the tissue. These networks add strength and stability. Like their name suggests, these fibres are highly elastic and thus help the tissue to retain its shape. Reticular fibres are constructed from the protein collagen and are much thinner than collagen fibres. Like elastic fibres, reticular fibres form highly ordered networks throughout the tissue giving the tissue strength and support. Cartilage consists of a dense arrangement of collagen fibres and elastic fibres within the ground substance. The collagen fibres make the cartilage very strong and resilient to loading and external forces.

The surface of cartilage is often covered by a dense irregular connective tissue, this is known as the perichondrium. The perichondrium contains two layers; an outer layer of collagen fibres, blood vessels and fibroblasts and an inner cellular layer of chondroblasts and chondrocytes, that contribute to the ECM production of the cartilage.

Cartilage can be classified into one of three groups; Hyaline cartilage, fibro cartilage and elastic cartilage. Hyaline cartilage has a white glassy appearance. Most hyaline cartilage is

coupled with a perichondrium layer, with the exceptions of articular cartilage in joints. Hyaline cartilage is the most commonly found cartilage in the body, providing support and flexibility. Hyaline cartilage also reduces friction and acts as a shock absorber. Of the three types of cartilage hyaline cartilage is the weakest. Fibro cartilage contains large bundles of collagen fibrils and is not surrounded by a perichondrium. The ground substance is minimal and thus this is the strongest of the three types. Fibro cartilage is commonly found in intervertebral discs. Elastic cartilage provides strength and is highly elastic. Elastic cartilage contains a high density of chondrocytes and thus a lower proportion of ground substance. A perichondrium surrounds elastic cartilage. An example of where elastic cartilage can be found is in the external ear.

Most connective tissues are highly vascularised and thus have an efficient supply of nutrients. Cartilage however emits antiangiogenic factor that prevents the growth of blood vessels [175]. Thus cartilage is avascular. The lack of a vascular network means cartilage is reliant on diffusion, and to a lesser extent convection, for its nutrient supply. Diffusion is a much less efficient transport mechanism than blood flow and thus cartilage can struggle to obtain the necessary nutrients it requires. This results in cartilage being slow to grow and slow to repair itself if damaged. The growth of a cartilage layer is the product of interstitial growth and appositional growth. Interstitial growth is where the chondrocytes within the tissue produce ECM and push each other away from one another. This causes the tissue to expand from within. This form of growth occurs when the cartilage is young, during childhood and adolescence. Appositional growth is where the tissue is added to at the surfaces. Cells in the perichondrium differentiate into chondroblasts which in turn produce large quantities of ECM. The ECM is then pushed underneath the perichondrium and the outer surface of the cartilage expands. Appositional growth occurs during adolescence.

Along with the slow nutrient transport mechanisms available to cartilage the other main factor that can affect the rate of tissue repair is age. As the body and cartilage ages the metabolic rate of the cells will become lower, leading to a slower rate of ECM production and thus the cells will be less efficient at repairing the tissue when required.

5.2 Literature review

We shall now discuss the literature available regarding cartilage tissue engineering. This review shall be broken down into three parts. Firstly we shall discuss the metabolic pathways that chondrocytes take to produce the energy they require. In particular this will be discussed in terms of the Crabtree and Pasteur effects and we shall also focus our discussion on the role of oxygen in producing energy. Secondly, we shall look at the experimental work that has been done in this area. The various methods of culturing the tissue shall be presented and discussed.

Finally, the various attempts at modelling tissue growth using mathematical models shall be reviewed.

5.2.1 Metabolism and the role of oxygen

It is commonly reported that chondrocytes synthesize the energy they require through glycolysis, [12, 77, 80, 86, 138, 169]. However the governing processes that determine how a cell creates ATP under different environments, *e.g.* Pasteur or Crabtree effect[1], differs between studies. Lee and Urban [99] studied cells taken from articular cartilage across a range of animals. The results show that in an environment in which the oxygen concentration was less than one percent[2], both the glucose consumption and lactate production were strongly inhibited and thus the cells were governed by a negative Pasteur effect[3]. These measurements were taken on a short time scale of hours and the effects over a longer time scale were not shown. Lee and Urban also considered the age of the animal from which the cells were taken. The results of this showed that the older the host donor the lower the cellular glucose uptake under both anaerobic and aerobic conditions. The negative Pasteur effect is confirmed by Bibby *et al.* [12] for isolated bovine nucleus pulposus cells, in which the lactic acid production by the cells decreased as the oxygen concentration also decreased. However Bibby *et al.* go on to point out that the metabolic effects can be dependent on the culture systems and that in explants a positive Pasteur effect was seen. This is the case presented in [86] in which Ishihara and Urban study dissected bovine coccygeal intervertebral discs. The results of a decrease in oxygen consumption on lactate production were described as showing a 'positive progressive Pasteur effect'. However this study implies that the difference is due to the origins of the cell rather than the culture process and that although intervertebral disc tissue and articular cartilage are similar, they are ultimately governed by different processes.

The driving force behind what determines the metabolic pathway cells take is studied further in [76, 77]. In [77], Heywood and Lee hypothesise that articular chondrocytes will switch from a glycolytic to an oxidative metabolism when they are introduced to a monolayer culture environment. This study looked at bovine articular chondrocytes and showed that there was a significant increase in oxygen consumption when the cells were cultured. However it was also shown that lactate production also increased and thus there was assumed an overall increase in the production of ATP. The oxygen consumption and thus ATP production due to aerobic respiration was shown to be very small during the first two days in which the cells were placed in the monolayer culture. However, in the subsequent twelve days the oxygen consumption was shown to consistently increase, with a reported thirty fold increase after fourteen days. The

[1] For more details on the Pasteur and Crabtree effects see Section 2.2 or [35, 36, 193].

[2] 1 % oxygen = 0.01 mole per m^3 = 7.6 mmHg

[3] Negative Pasteur effect implies that as the oxygen concentration decreases and aerobic respiration becomes inhibited, the rate of anaerobic respiration and glucose consumption does not increase

corresponding increase in lactate production was only two fold. It was thus concluded that the cells act differently initially after being seeded than in the subsequent period of time. More recently Heywood *et al.*, [76], studied whether sub populations of cells within cartilage layers consume oxygen at different rates. The sub populations were determined by the depth from which the cells were extracted from the cartilage layer. Both deep and superficial cells were observed to be governed by the Crabtree effect, with the deep cells demonstrating a greater capacity for oxygen consumption than the superficial cells.

Zhou *et al.* study chondrocytes from bovine cartilage in [197]. The rate of consumption was shown to be constant until the glucose concentration fell below one milli-molar. The metabolism of the chondrocytes was also shown to be affected by the pH, where a linear decrease in lactate production as pH fell from 7.4 to 6.4. In the same range a smaller percentage reduction in oxygen consumption was seen.

Murphy and Sambanis, [128], report that in bovine articular chondrocytes the concentration of oxygen has a significant effect on the rate of proliferation of a cell and the quantity of ECM it produces. In a high concentration of oxygen cells were observed to constantly proliferate throughout the twenty day culture period. At five percent oxygen, cells stopped proliferating after twenty days and in one percent oxygen there was no proliferation seen after six days. The author of this thesis suggests this may imply that the energy demand for proliferation is very large and thus a cell requires aerobic respiration, due to its higher efficiency rate, to create enough ATP to undergo mitosis. However further investigation would be required to confirm this. Clark *et al.*, [30] report that the maximum rate of GAG synthesis for bovine chondrocytes is at an oxygen tension of twenty-one percent. Whilst the maximum rate of proteoglycan aggregation was found at an oxygen tension of three percent. Bovine articular chondrocytes were once again used in the study presented by Domm *et al.* in [43] in which the effects of oxygen concentration on cell differentiation were studied. Monolayers cultures of initially proliferating cells were shown to continue proliferating for all concentrations of oxygen. No collagen was produced in these cultures during the three week experiments. At high oxygen concentrations the same results were seen in alginate bead cultures. Only when the oxygen concentration was reduced to five percent did these cells re-differentiate and synthesize collagen.

The contribution of aerobic respiration for ATP production in bovine articular chondrocytes is shown to be small in [77, 99]. Therefore the role of oxygen in determining ATP production when modelling tissue growth would also be small. However it has already been shown that the contribution from oxygen differs across different regions of tissue and also plays a role in the differentiation of cells as well as the production of ECM. Therefore the distribution of oxygen may still be important when modelling the growth of tissue. Malda *et al.* [113] measure the oxygen gradients within tissue engineered constructs grown from the femoral condyle of bovine

calves. The low consumption rate of the cells resulted in the oxygen concentration remaining high for large tissue constructs. Only when the depth of tissue was greater than a millimetre was the oxygen concentration reported to drop significantly, in this case to below a fifth of its original value. This gradient was also considered to be more pronounced than in cartilage explants due to the higher density of cells and lower diffusion coefficient in the engineered tissue. The oxygen consumption was also thought to be affected by the cells differentiating. From the study presented by Malda *et al.* we can conclude that for tissue engineered constructs under a millimetre in depth the oxygen gradient will be small and thus the distribution of oxygen will have little effect on the growth of the tissue layer. More recently Zhou *et al.*, [196] investigated the oxygen concentration across cartilage samples taken from a range of animals. They concluded that both the delivery and consumption of oxygen was determined by a combination of cell density, cell distribution, cartilage thickness, oxygen supply and the oxygen consumption rate of the individual cell type.

Further reviews of the effects of metabolism and oxygen are given by Grunhagen *et al.* [70] and Henrotin *et al.* [75].

5.2.2 Experimental

The growth of tissue *in vitro* has been shown to be possible using various methods, each with their individual characteristics and merits. The most common methods are pellet cultures, monolayer cultures and seeded scaffolds. Pellet cultures are simply balls of cells packed at high densities which are placed in culture medium and left to evolve; as used in [108, 173] to grow cartilage constructs. Pellets share many of the same properties of multicellular tumour spheroids, and therefore nutrient transport and consequently growth will be dependent of the transport of nutrients and dominated by diffusion. Monolayer cultures have been successfully used to grow tissue structures [7, 58, 72, 127, 141]. Like pellets, monolayer cultures have no framework to give the cells a physical structure to bind to. A monolayer culture will begin as a densely packed layer of cells and expand due to proliferation and ECM production. As in pellet cultures it is likely that insufficient nutrient transport, due to inadequate diffusion, will limit the rate of growth. The limitations of diffusive transport can be reduced by the use of polymer scaffolds, as used in [49, 115]. These provide a highly porous framework for the cells to be seeded onto, allowing more efficient diffusion and the opportunity to have a driven flow of fluid through the cellular region, thus enhancing nutrient transport. These scaffolds are often degradable, thus the final tissue structure will only consist of cells and the ECM that has been produced. Bioreactors are often used to further enhance the growth of a tissue construct [47, 48, 148, 182]. The bioreactor provides a controlled environment for the tissue growth, in which the pH, temperature, media flow rate and hydrodynamical and mechanicals forces can all be maintained [26]. For reviews and further information on the design and methods of

tissue growth, involving scaffolds and bioreactors we refer to [38, 84, 98]

Studies into the *in vitro* growth of tissue engineered construct have yielded results comparable to tissue grown *in vivo*, [148]. It has been shown that mechanical loading affects the production and structure of the ECM both *in vitro* [182] and *in vivo* [85, 189], as well as the cells metabolic activity [180]. Although the ECM provides a tortuous path for nutrient transport [101], Torzilli *et al.* [176] showed that as the tissue developed from immature to mature cartilage there was no statistical difference in the diffusion properties.

Hayes *et al.* [72] present results of experimental work on the expansion of bovine cartilage cells from a monolayer culture. Photographic results of tissue growth, distribution and movement of cells, alongside a discussion of the structural components that make up the extracellular matrix is given. The thickness of the tissue is shown to increase at a constant rate over time, whilst the cells are shown to spread out at different rates dependent on their location within the tissue. The highest density of cells is found in the lower part of the tissue. A similar setup was used by Furukawa *et al.* [58], however this study found that a rotational culture was required for the tissue construct to maintain its shape. Chondrocytes isolated from articular cartilage were cultured in a scaffold free environment both *in vitro* and *in vivo* by Park *et al.*, [141]. The total mass of GAGs was shown to rise throughout the culture period as did the total cell number. It was observed that in the early phases both cell proliferation and differentiation were occurring simultaneously. At later stages the majority of cells were solely producing GAGs. Riesle *et al.* [148] show that in bovine cartilage cell seeded scaffold the percentage weight of cells dropped over time, whilst the percentage weight of GAGs and collagen increased at constant rates. Ofek *et al.*, [137] provide a similar analysis for chondrocytes seeded in aragose coated wells. The results of this experiment show the percentage wet weight and mass of GAGs within the construct to rise. The mass of collagen within the construct was shown to rise at a steady rate, however the percentage wet weight of collagen within the construct decreased over the fifty-six day culture period. The production of GAG was shown to increase over time, suggesting the cells focused on collagen production in the initial stages before differentiating and producing GAGs. Further investigation would be required to determine the reason behind this difference, but the author of this thesis believes possible factors that caused this are transport of nutrients and the density of cells.

For further reviews of the mechanical properties of tissue and the field of tissue engineering refer to [19, 69, 167].

5.2.3 Mathematical modelling

The growth of *in vitro* tissue can take many forms, depending on the culture system and cell line studied. These differences mean there is a wide variety of mathematical models that study

the individual cases.

The gradients in concentration of oxygen, glucose and lactate have been individually or collectively modelled across a wide range of systems including within chondrocyte pellets, [129], cartilage explants [113], intervertebral discs [119, 120] and other tissue engineered constructs [60, 61, 113, 159, 197]. The distribution of nutrients and the effects these have on cell growth and density have been studied in [59, 102]. These models look at transport in terms of diffusion and provide good explanations for the distribution of nutrients. However with the exception of [59], these models do not show how nutrient transport affects the growth of the tissue. Galban and Locke, [59] incorporate a moving boundary into their model of nutrient consumption and tissue growth in a polymer scaffold. This model imposes that the tissue expansion is dependent on the growth of cells at a rate proportional to the concentration of nutrients on the moving boundary.

So far, the models listed have looked at the transport of nutrients but have not considered the production of ECM or the growth of a tissue construct. DiMicco and Sah [42] investigate the composition of cartilage in terms of the transport of nutrients and the evolution of matrix within cartilage tissue. The distribution of synthesized matrix was further studied by Sengers *et al.*, [158], to determine the mechanical properties of tissue engineered cartilage.

The transport of nutrients through *in vivo* tissue is dominated by diffusion. However an advantage of *in vitro* engineered tissue is that alternative transport mechanisms can be utilised to help promote growth. Zhou *et al.*, [197] study the nutrient transport in a perfusion culture system, whilst Whitaker *et al.*, [190], show the effects of inducing a flow of culture medium through a scaffold and the effects this has on nutrient and waste transport, as well as shear stress. Similarly O'Dea *et al.* [136], study how an imposed flow can affect the growth of a tissue construct. The work presented by O'Dea *et al.* [136], builds on work in [100] by using a continuum two phase fluid model of tissue growth. The first phase consisting of cells and ECM and the second culture medium. Ferguson *et al.*, [45] and Gardiner *et al.*, [62] both consider how the mechanical forces can affect fluid flow. Ferguson *et al.* studied the flow in an intervertebral disc, showing that mechanical loading can aid the transport of large molecules. Whilst Gardiner *et al.* [62] considered a cylindrical plug of cartilage and showed that altering the frequency of loading can increase of decrease the transport or insulin-like growth factor-I.

Mathematical modelling of the growth of engineered tissues is still in its infancy. Obradovic *et al.* [135] model the distribution of GAGs within a seeded scaffold cultivated in a bioreactor. The model imposed a maximum concentration of GAGs. This was defined as being the time at which the production of GAGs balanced degradation and incorporation into the ECM. The rate of GAG synthesis was then a function of the local concentration of oxygen and GAGs. The model showed good comparison to experimental data regarding the concentrations of GAGs. The model presented by Obradovic *et al.* was expanded by Catt *et al.* [25] to include

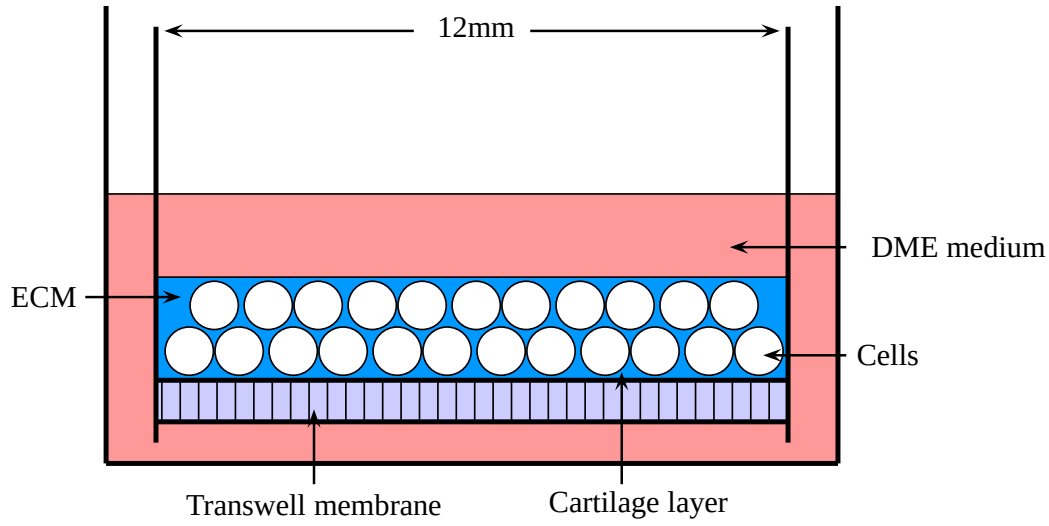

Figure 5.1: Schematic of the Millipore filter and layer of cartilage.

cell proliferation and cell differentiation as well as the effects of scaffold degradation and water transport. A similar model was developed by Lewis *et al.* [103] which considers the consumption of nutrients and production of proteoglycans in cartilage pellet cultures.

There have been various other studies relating to tissue engineered constructs. These include studies into the movement of individual and groups of cells, [140, 139], transport of insulin-like growth factors and the effects on production of GAGs, [195] and investigations into the properties of single chondrocytes, [178]. For a review of some of the current mathematical models of tissue constructs see [34, 111, 157].

5.3 Experimental setup

We shall now incorporate the ideas and concepts reviewed in Section 5.2 to construct a continuum model for the growth of a tissue engineered construct. The model will look specifically at a monolayer culture of equine cartilage. The model will then be compared to experimental data at various stages of the tissues development.

It has already been shown that the properties of tissue engineered constructs are individual to their culture systems, therefore a review of the culture process and resulting constructs will be given. These observations will be used alongside the known characteristics of chondroblasts, chondrocytes and cartilage to create a mathematical model for the growth of the construct, as well as the evolution of the chemical species that determine the growth. We shall begin by explaining the experimental setup we used to culture the cartilage layers.

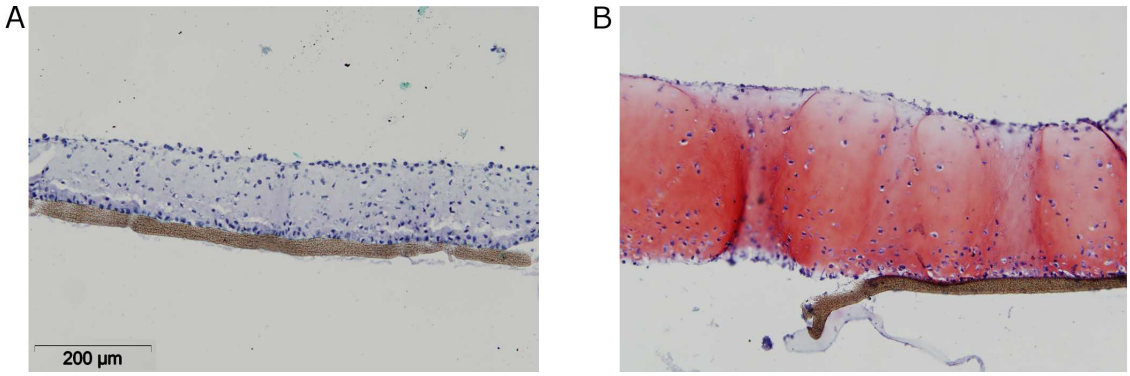

Figure 5.2: Tissue samples at 14 (**A**) and 49 days (**B**). The staining indicates the presence of collagen (blue) and GAGs (red). The cells can be seen as darker dots, distributed throughout the tissue but at highest density at the surface of the membrane and at the surface of the tissue.

Equine chondrocytes were isolated and seeded in t-flasks at a density of 5000cells/cm^2. The chondrocytes were left for approximately ten days to proliferate before being harvested and seeded onto collagen coated Millipore filters. The filters were then immersed in Dulbecco's modified Eagles medium (high glucose) (DME). DME provides the nutrients required by the chondrocytes to satisfy their energy requirements as well as providing the necessary building blocks required for extracellular matrix production. Millipore filters consist of a permeable Transwell membrane that allows DME transport from beneath the tissue layer as well as from the surrounding fluid above the tissue. This experimental setup is schematically shown in Figure 5.1. Three samples of the tissue were then taken at seven time points over the forty-nine day period. Individual samples were then halved; one half was processed for histology whilst the other half for quantitative assays. The DME was replaced at regular intervals, between three and four days and the extracted fluid was stored for further analysis.

5.3.1 Tissue processing; histology and quantitative assays

The tissue samples were sliced into ten micron deep slices and analysed to determine the thickness of the layer, the distribution of cells within the layer, the presence of collagen, the distribution of GAGs and the quantity of GAG being excreted into the surrounding medium. This analysis was achieved by staining the tissue slices with Safranin-O. This staining indicates the presence of collagen and distribution of GAGs. Photographs of all samples were then taken to quantitatively assess the distribution of ECM. Example images of the stained tissue slices at fourteen and forty-nine days are given in Figure 5.2. The complete set of images is given in Appendix C.

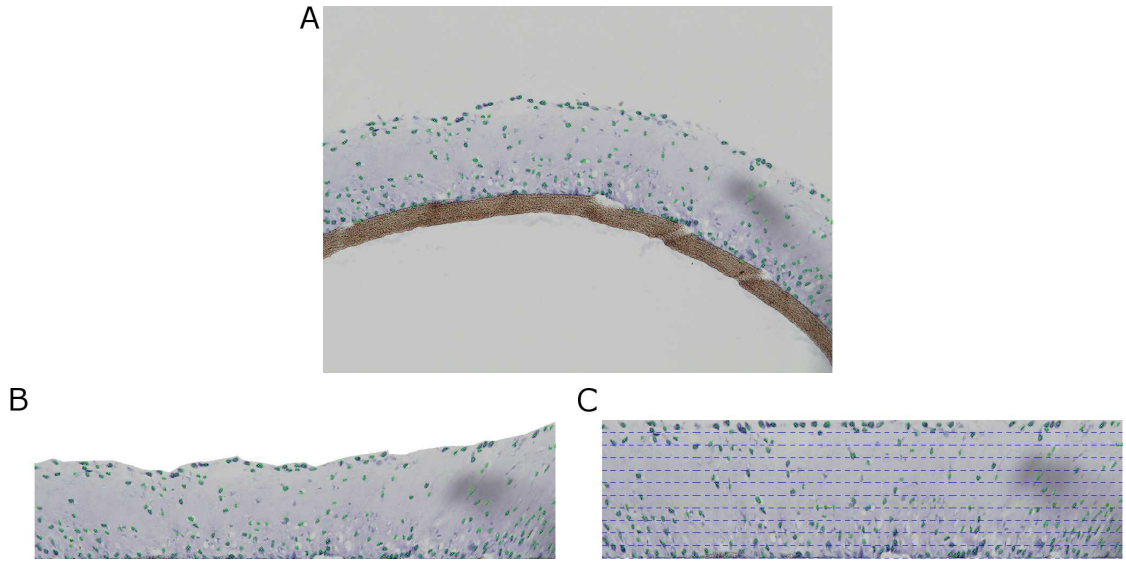

Figure 5.3: A sample of an analysed slice of tissue. The original sample (**A**), the adjusted image (**B**), and the one dimensional image (**C**), are given.

5.3.2 Data analysis

During processing samples were occasionally damaged or experienced rips or folding. The photographs of these samples were cropped to discount misleading sections of tissue. The distribution of cells was then derived using image analysis software[4] written in MATLAB [174]. As can be seen in Figure 5.3**A** the tissue samples did not grow as perfectly uniform layers. Nor did the shape of the membrane remain flat during processing. Thus the images were adjusted so that the lower edge of tissue remained horizontal, as shown in Figure 5.3**B**. The position of each cell was then derived in relation to the adjusted image.

Throughout the duration of the experiment the width of the cell layer is always at least two orders of magnitude greater than the height. Therefore an appropriate approximation is to model the growth as a one dimensional layer, expanding in the vertical direction.

The samples taken on any single day were analysed to give a single representation of the tissue at each point. Early methods of analysing the samples consisted of dividing the slices into bands of constant heights in which the lowest band was adjacent to the Transwell membrane. The number of cells in each band was then calculated and the cell density derived. This method accurately accounted for distribution of cells in the lower regions. However the vertical growth of the tissue is not at a constant rate across the layer. Thus the upper surface of the tissue is not flat and does not necessarily reside in one band. These factors meant the density of cells was shown in the data to be at its lowest at the surface of the tissue, which does not describe

[4]The original code was written by Bram Sengers, [156] and was developed further for this study.

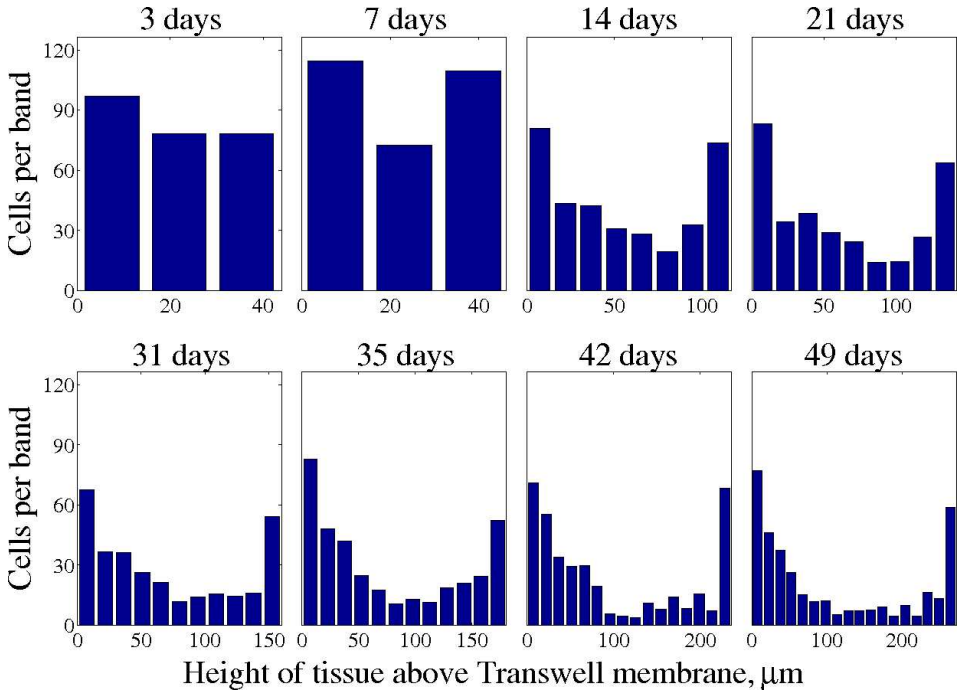

Figure 5.4: Histograms showing the averaged distribution of cells through the tissue samples. The first bar of each histogram represents the cell density next to the Transwell membrane in the lower band. The right hand bar in each histogram is the cell density in the upper band at the tumour surface. The bars in between represent the cell density in the central region. The height of each band is approximately 15μm.

the characteristics of the tissue samples. Thus the images and derivation of band positioning was adjusted. The process for which was the same at each time point and consisted of the following steps. Firstly an average height of the tissue was derived by using the images which had been adjusted so that the lower edge was straight, as in Figure 5.3**B**. The vertical height of the surface over the slice was then derived and an average was then taken for each individual sample. The averaged heights were again averaged to give an average height of the tissue slice at that time point. A representative height of tissue has now been derived at each time point. Using this height, each image was vertically scaled so that the height of the slice at every point was equal. An example of a resulting image is shown in Figure 5.3**C**. These uniform images were then divided up into bands and the cell density derived. The height of each band was chosen to be approximately fifteen microns; the diameter of a cell. However the exact height was determined by the height of the tissue, such that,

$$\text{number of bands} = \left[\frac{\text{tissue height (microns)}}{15}\right], \tag{5.1}$$

where the square brackets indicate that the surrounded number should be rounded to the nearest integer. Thus as the tissue height increases it can be shown that the height of each

Parameter		Value	Units
Cell density in lower band	N_{lo}	$2.36 \cdot 10^{14}$	cell m^{-3}
Cell density in upper band	N_{up}	$1.87 \cdot 10^{14}$	cell m^{-3}
Cell in-flux	$F_{N_{pro}}$	$1.66 \cdot 10^{3}$	cell m^{-2} s^{-1}
Cell over-count fraction	ζ	0.410	
Height of lower and upper bands	Δ_{pro}	$1.5 \cdot 10^{-5}$	m
Height of Transwell membrane	Δ_t	$3 \cdot 10^{-5}$	m
Initial cell density	N_0	$1.72 \cdot 10^{14}$	cell m^{-3}
Initial height of tissue	S_0	$3.6 \cdot 10^{-5}$	m
Radius of a cell	r	$7.5 \cdot 10^{-6}$	m

Table 5.1: Parameters resulting from the experimental setup and data.

band will tend to fifteen microns. Histograms of each sample were then calculated and an averaged sample for each time point derived. An analysed sample of tissue that has been scaled is shown in Figure 5.3**C** and the averaged histograms are given in Figure 5.4.

When slicing the tissue samples cells are cut into multiple pieces. These cells will be included in at least two samples when the cell densities are calculated. This results in an over counting of cells. Therefore the fraction of cells that belong to each slice must be derived so that the cell density of each sample can be adjusted. This was achieved by taking random sections of photographed samples, where the width of the selection was the same as the depth of the sliced tissue, ten microns and the height was that of the sample slice. The number of cells in this selection was then derived and the density of cells in these sections were then compared to the density in the corresponding tissue slice. The ratio of these densities gave a scaling factor that determines the number of cells that belong to each slice. The individual scaling factors were averaged to give a scale which was used to adjust the cell densities of each slice. The value of which, denoted by ζ, is given in Table 5.1.

At any time step a wide range of tissue heights were observed. However, using the method described above, the averaged data shows a linear increase in the height of the tissue layers. Similarly the number of cells per slice are scattered over a large range, but again the averaged data shows a linear increase in the population of cells over time. These results are presented graphically in Figure 5.6.

The stained tissue slices appear blue before approximately five weeks. This implies a dominant presence of collagen in the early growth stages. Thereafter the tissue slices are red, implying the production of GAGs has increased. However, subsequent analysis of the data reveals that this is misleading. All samples were analysed after the completion of the experiment. This

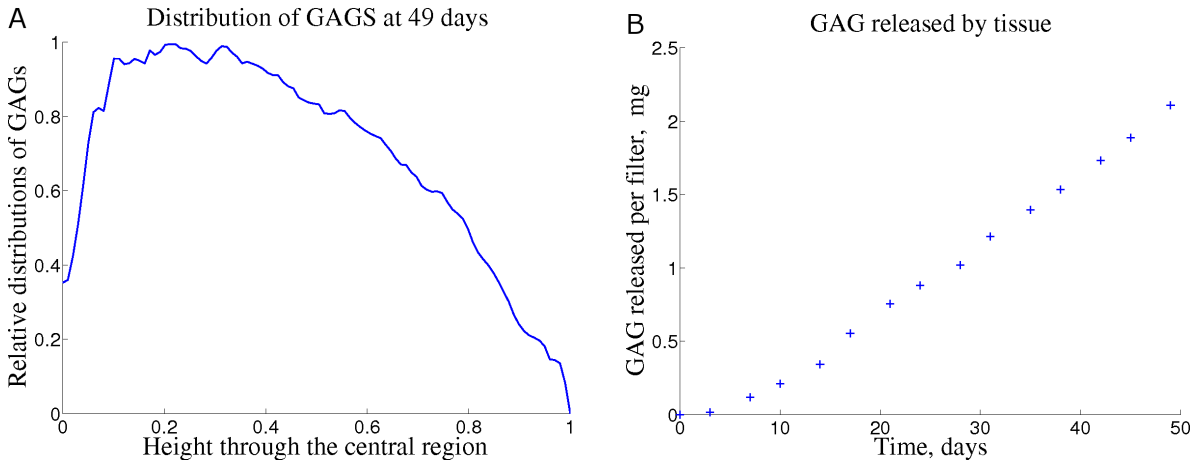

Figure 5.5: Data showing the distribution of GAG within the structure at 49 days (**A**) and the accumulated quantity of GAG released (**B**).

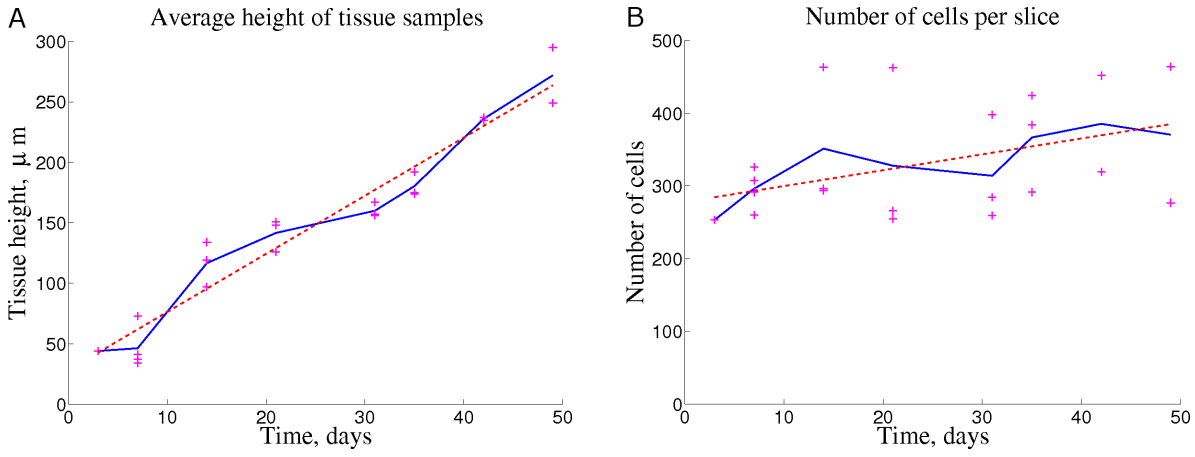

Figure 5.6: Data showing the average height of the tissue over time (**A**), and the number of cells per tissue slice (**B**). The experimental data (+), averaged data (—) and a linear fit to the averaged data (- - -) are given.

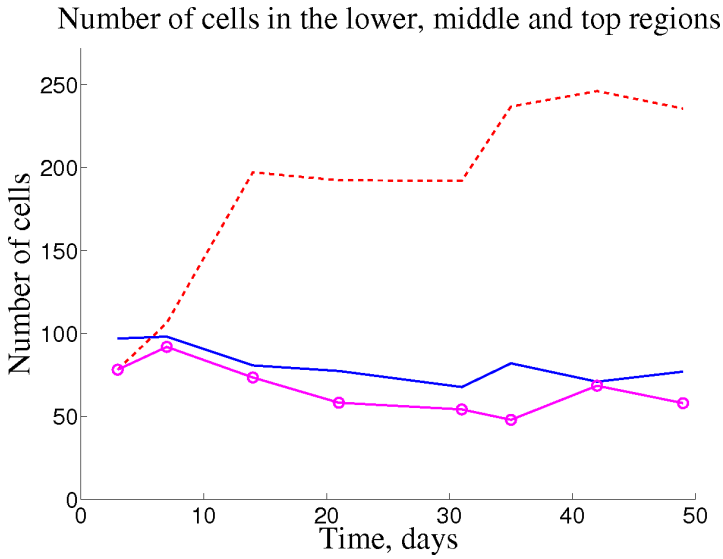

Figure 5.7: Experimental data showing the number of cells in the lower band (—), upper band (-o-) and in the central region (- - -). Both the lower and upper bands are $15\mu m$ high.

delay allowed the GAGs to diffuse out of the samples taken at the early time points. Thus the early samples appear to be absent of GAGs. Therefore it was decided that the data regarding the distribution of GAGs taken from early time samples should be neglected. The time between sampling and analysis for the samples taken at forty-nine days was small and thus it was decided that the distribution of GAGs within these samples could be studied. The GAG distribution was derived by analysing the photographs. Safranin-O dyes tissue red in the presence of GAGs. Therefore the colour distribution of the photographs was taken and the red light that had been filtered out was derived. The resulting distribution of GAGs for a sample taken at forty-nine days is shown in Figure 5.5**A**.

The extracted fluid that surrounded the tissue was analysed for GAG content. This gave an indication of GAG loss from the tissue structure over time. The structure of the Millipore filters allows the medium above and below the layer to mix. Therefore quantity of GAG released is the combination of that excreted from the top surface of the tissue layer and that which has diffused through the membrane. The results are presented in Figure 5.5**B** and after an initial period show a linear increase in the accumulated mass of GAGs released form the tissue construct over time. In the early stages of the experiments the rate of GAG release is less than derived at later time points.

5.4 Review of the experimental data

We shall now review the experimental data that has been extracted from the tissue samples. Figure 5.4 shows the density of cells in an averaged tissue slice over time. The experimental data suggests that the movements of cells is a consequence of ECM production. Therefore a cell which has a plentiful supply of nutrients will synthesize ECM and spread away from its neighbours. However the data detailing the distribution of cells shows this to be a more complicated process. At all time points the highest cell density is found at the lower and upper boundaries. This coincides with the position of the maximum nutrient concentration. Thus although these cells exist in the optimal environment for ECM production they do not separate. Therefore more complicated mechanisms, such as cell signalling or contact guidance, must be at work. The cells at the boundaries are obviously trying to stay attached to the edges and are not producing ECM to promote separation. This is shown more clearly in Figure 5.7, where the number of cells in the lower band, upper band and the central region are plotted over time. The number of cells in the lower and upper bands are almost equal and remain relatively constant over time. The population in the central region increases, however the histograms in Figure 5.4 show that the density of cells to decrease with time in this region. Therefore ECM production is separating the cells at a rate faster than cell proliferation within the central region. The cell density plots in Figure 5.4 also show that after fourteen days the cell density in the lowest six bands does not continue to change. This may be due to inefficient nutrient transport and the resistance due to the Transwell membrane, restricting the supply of nutrients to the lower cells; but the distances are small relative to the rate of diffusion. A more likely explanation is that the cells on the lower membrane recognize their location and excrete inhibitors that signal to the surrounding cells to stop proliferation and ECM production.

5.5 Cartilage layer model

We shall now use the experimental findings and literature review given in sections 5.2 to 5.4 to construct a model that describes the physical and chemical processes that occur within a growing layer of cartilage tissue. In particular the model will focus on the density of cells, and concentration of ECM through the construct. However, firstly, the role of DME and glucose shall be discussed.

DME medium primarily consists of glucose, which is the main ingredient used by cells to synthesise ECM, as well being an essential ingredient to create energy through respiration. Therefore it maybe necessary to include the concentration of glucose in this model of tissue growth. However the concentration of glucose within the DME medium is very high, 4.5g/L [165]. The medium is also replaced at regular intervals throughout the experiment and thus

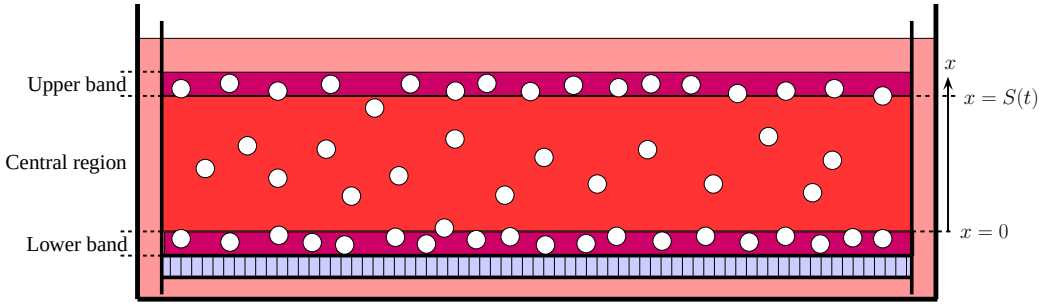

Figure 5.8: Schematic of the idealised model and modelling notation. The upper and lower bands are $15\mu m$ in height. The cells in the upper band are proliferating whilst the cells in the lower band are quiescent. The central region contains cells producing collagen and GAGs and increases in depth over time.

the glucose is replenished. We can therefore assume that the medium surrounding the tissue is well mixed. By using a typical cell density from the experiment results, N_0, a typical diffusion coefficient, D_{gl} and consumption rate of glucose, R_{gl} from the literature, [155] and the concentration of glucose in the DME medium, Gl_0, we can approximate the distance away from the surface in which diffusion will be an insufficient transport mechanism to provide glucose to the cells. This is calculated to be,

$$\sqrt{\frac{Gl_0\, D_{gl}}{N_0\, R_{gl}}} \;=\; \mathcal{O}\left(10^{-3}\right) m. \tag{5.2}$$

The height of the tissue during the experiment never exceeds 300μm and thus the distance a cell is from the well mixed medium is much smaller than the distance required for consumption to dominate over diffusion. Therefore the gradients in glucose concentration within the tissue structure will be negligible throughout the experiment and the cells will constantly have a plentiful supply of glucose to synthesize ECM and convert to ATP by respiration. Thus the consumption and transport of DME and glucose can be neglected in this model.

The ECM found in cartilage tissue is a complex structure consisting of many different components. In this model we will only consider collagen and GAG. Collagen is the most common fibrous protein found in the ECM of tissue. In particular type II collagen is the most abundant protein found in cartilage [11]. Made of thin fibrils, type II collagen makes the cartilage structure very strong [41]. Consequently, as described in Section 5.1.1, collagen will be thought of as forming a scaffold in which the cells and GAGs will exist.

As shown in Figure 5.8 the tissue shall be broken down into three regions. Firstly a thin, fifteen micron, layer of densely packed cells that are situated directly on top of the Transwell membrane. Due to inhibitory factors these cells will not proliferate nor create ECM and thus will not spread out. The density of cells will remain constant over time in this region and the

cells will be assumed quiescent.

In the central region there will be no proliferation. Cells in this region will create collagen and/or GAG and to simplify the model a cell will only undertake one type of reaction act a time. Cells are therefore not allowed to simultaneously produce collagen and GAGs. Thus the cell population can be broken down into the density of collagen producing cells and the density of GAG producing cells. The fibrous framework for the tissue structure is required before the ground substance can be added. Thus any new cells will be defined as collagen producing cells before differentiating to GAG producing cells. Once a cell is defined as a GAG producing cell we shall assume that it can not return to collagen production. This coincides with the experimental findings of Ofek *et al.* [137].

Finally there is an upper region. Lying on top of the central region the upper region is a thin, fifteen micron, layer of proliferating cells, that remains at constant density by emitting the newly synthesised cells into the central region. These new cells will be collagen producing cells. The cells within this region do not create collagen nor GAG and so this region will not expand in size. The density of cells in this region is different to that in the lower region. It will be assumed that the cells within this upper region are proliferating at a constant rate and the newly formed cells will be pushed into the central region.

Throughout the whole structure the effects of cell death will be neglected as these are believed to be negligible in tissue of this size. It has been shown than the gradients in glucose concentration that arise within the tissue are negligible. Similarly the gradients in oxygen will be small as oxygen will diffuse faster than glucose and the consumption of oxygen will be low due to the Crabtree effect governing cell metabolism. Therefore the cells will always be able to obtain the energy they require for respiration. Thus ATP production and cell metabolism will also be neglected at this stage. The ideas presented above are schematically shown in Figure 5.8.

5.6 Modelling equations

We shall now consider the equations that govern the structural growth of the tissue and the distribution of cells and ECM within the layer. We shall consider ECM to only consist of collagen and GAG.

The density of cells and concentration of ECM in the lower and upper bands are constant for all time. Therefore we shall focus the model on the central region and only study the lower and upper bands when considering boundary conditions. In the central region the density of collagen producing cells, N_{col} and GAG producing cells, N_{gag}, is governed by conservation of

mass, such that,

$$\frac{\partial N_i}{\partial t} + \boldsymbol{\nabla} \cdot \mathbf{F}_{N_i} = P_{N_i}, \tag{5.3}$$

where $\mathbf{F}_{N_i}$ and P_{N_i} are the flux and production rates of cell type N_i. As discussed in Section 5.3 this model shall consider the growth only to be in one dimension, in the vertical direction, defined by $x \in [0, S(t)]$, where $S(t)$ is the upper surface of the tissue as shown in Figure 5.8. Cells will only move due to the production of ECM causing the structure to expand. Therefore cell flux will be due to the effects of advective transport. There are various different velocities associated with the growth of the tissue layer. These include the velocity of cells, the velocity of the ECM and the velocity of the extracellular water. This model will not consider these independently and will instead consider an averaged velocity, $U(x,t)$. Hence the flux of cells can be expressed as,

$$F_{N_i} = N_i\, U. \tag{5.4}$$

Both collagen and GAG only exists in the space between cells, thus we shall only consider their concentrations in the space available to them. The volume fraction of extracellular space is denoted by Φ and is is derived by multiplying the volume of a cell by the numbers of cells contained in a given space. If we assume that the space we are considering has a volume of $1m^3$ and that the cells are spherical with constant radius r, then the volume of cells in this region equals

$$\frac{4}{3}\,\pi\, r^3\, \left(N_{col} + N_{gag}\right). \tag{5.5}$$

The extracellular volume in this region is thus,

$$1 - \frac{4}{3}\,\pi\, r^3\, \left(N_{col} + N_{gag}\right). \tag{5.6}$$

Therefore to obtain the extracellular volume faction we simply divide by the volume of the space we are considering. Thus,

$$\Phi = 1 - \frac{4}{3}\,\pi\, r^3\, \left(N_{col} + N_{gag}\right). \tag{5.7}$$

The concentrations of GAG and collagen, C_{gag} and C_{col} respectively, are governed by conservation of mass, such that through the tissue layer,

$$\frac{\partial}{\partial t}\left(\Phi\, C_i\right) + \frac{\partial F_i}{\partial x} = P_i, \tag{5.8}$$

where F_i and P_i are the flux and production rates of component i.

The transport mechanisms that determine the distribution of GAGs are advection and diffusion. Due to the structural nature of collagen we shall assume that the transport collagen will

solely be a function of advection. Advection will be a consequence of the structure growing, whilst diffusion shall be given by Fick's law, where D_i will denote the diffusion coefficient of species i. The flux of collagen and GAGs are thus given by,

$$F_{col} \;=\; \Phi\, C_{col}\, U, \tag{5.9}$$

$$F_{gag} \;=\; \Phi\, \left(C_{gag}\, U \;-\; D_{gag}\, \frac{\partial C_{gag}}{\partial x} \right). \tag{5.10}$$

5.6.1 Source terms

We shall now consider the production of cells, collagen and GAG within the central region. Collagen has previously been described as a fibrous protein that provides the scaffold that supports the tissue. Thus it shall be assumed that cells will initially produce collagen. GAG is more gel-like in structure and provides the bulk around the collagen framework. Thus GAG will be synthesised only once the collagen scaffold has been produced. Therefore it shall be assumed that cells initially produce collagen and then switch over to GAG production. This switch could be determined by cell density, collagen density or by nutrient concentration. However due to the uniform concentration of glucose within the tissue this switch over will be a function of time only. This rate of conversion of cells producing collagen to GAG producing cells will be denoted by R_{cg}. Thus the rate of change in density of collagen and GAG producing cells due to cell differentiation is described by,

$$P_{N_{col}} \;=\; -\, N_{col}\, R_{cg}, \tag{5.11}$$

$$P_{N_{gag}} \;=\; N_{col}\, R_{cg}. \tag{5.12}$$

Rates of proliferation and necrosis are assumed negligible in the central region and thus are not included in the above expressions for the production of cells.

The rates at which collagen and GAG are synthesized are denoted by R_{col} and R_{gag}. We shall assume that the components required for collagen and GAG synthesis are at high concentrations and do not restrict ECM production. Therefore the rate of collagen and GAG production is described by,

$$P_{col} \;=\; N_{col}\, R_{col}, \tag{5.13}$$

$$P_{gag} \;=\; N_{gag}\, R_{gag}. \tag{5.14}$$

Parameter		Value	Units	Ref.
Concentration of collagen	Col_0	$1.23{\cdot}10^5$	g m^{-3}	[47]
Diffusion coefficient GAG	D_{gag}	$7.42{\cdot}10^{-11}$	m^2 s^{-1}	[135]
ECM production rate	R_{ecm}	$1.55{\cdot}10^{-14}$	g $cell^{-1}$ s^{-1}	[155]
Transwell filtration fraction	Φ_t	0.5305		[116]

Table 5.2: Parameter values taken from the literature.

5.6.2 Collagen and growth

The model as presented so far is under-defined. Thus along with initial and boundary conditions an extra condition must be imposed to close the problem. This maybe achieved by balancing forces in the tissue or by momentum conservation. However we wish the structure of this model to remain as simple as possible. Thus we shall instead focus on the properties of collagen.

We have previously discussed that collagen forms the frame work or scaffold for the tissue and that the cells and GAGs exist within this. The structural nature of collagen results in the diffusion of collagen being very slow, $\mathcal{O}\left(10^{-12}\right) m^2 s^{-1}$ [160]. Therefore the relative distribution of the synthesised collagen would change very slowly if collagen production spontaneously ceased. The tissue is also growing under no compressive loads, therefore the mechanical forces on the structure will be small. Thus it is reasonable to assume that the density of the collagen scaffold will be spatially uniform through the structure and over time. Collagen is made up of fibrils that allow it to remain bounded to together in long strands. Therefore we can also assume the mixing of the fluid above the top surface does not tear any of the collagen fibrils away from the structure. Therefore to close the model we shall impose that the density of collagen remains evenly distributed throughout the tissue structure and that this density will remain constant over time, such that,

$$C_{col}\left(x,t\right) \,=\, Col_0, \tag{5.15}$$

where the value of Col_0 is given in Table 5.2. This will also impose that the cells move with the collagen as it is synthesized.

The main consequence of this assumption is that we can now develop an equation explicitly for the velocity of the tissue. This can be shown by rewriting equation (5.8), which imposes conservation of collagen, with the new condition given by equation (5.15), such that,

$$\frac{\partial \Phi}{\partial t} \,+\, \frac{\partial}{\partial x}\left(\Phi\, U\right) \,=\, \frac{P_{col}}{Col_0}. \tag{5.16}$$

Using equation (5.7), we expand equation (5.16), to give,

$$-\frac{4}{3}\pi r^3 \left(\frac{\partial}{\partial t}\left(N_{col} + N_{gag}\right) + \frac{\partial}{\partial x}\left(\left(N_{col} + N_{gag}\right)U\right)\right) + \frac{\partial U}{\partial x} = \frac{P_{col}}{Col_0}. \tag{5.17}$$

In the central region there is no proliferation nor cell death. Thus away from the upper edge the aggregate cell density is conserved. Alternatively this can be derived by summing equation (5.3) over all cell types to give,

$$\frac{\partial}{\partial t}\left(N_{col} + N_{gag}\right) + \frac{\partial}{\partial x}\left(\left(N_{col} + N_{gag}\right)U\right) = 0. \tag{5.18}$$

Therefore equation (5.17) can be simplifed to give,

$$\frac{\partial U}{\partial x} = \frac{P_{col}}{Col_0} \quad \text{for } x \in [0,\, S(t))\,. \tag{5.19}$$

5.6.3 Initial conditions

The cells go through a settling period immediately after being seeded in which their characteristics greatly differ from that seen during the later stages of the growth period. The settling period will not be modelled and the modelling simulations will begin at day seven, such that t represents the time after day seven. The initial conditions will therefore be taken from the analysed data rather than the experimental set up. Therefore the initial height will be such that,

$$S = S_0 \tag{5.20}$$

and the cell density governed by,

$$N_{col} + N_{gag} = N_0 \quad \text{at } t = 0, \tag{5.21}$$

where the initial density of cells is assumed to be uniform through out the tissue and S_0 and N_0 are given in Table 5.1. We shall assume that by the end of the settling period there has already been cell differentiation. The initial ratio of collagen producing cells to GAG producing cells will be given by α_{cg}, such that,

$$N_{col} = \alpha_{cg} N_0 \quad \text{and} \quad N_{gag} = (1 - \alpha_{cg})\, N_0 \quad \text{at } t = 0. \tag{5.22}$$

Although the cells will have been in culture for seven days by the time our simulation begins the height of the tissue is still small. Therefore it will be assumed that the cells have not yet produced any GAGs and thus we impose,

$$C_{gag} = 0 \quad \text{at } t = 0. \tag{5.23}$$

5.6.4 Boundary conditions

The lower surface of the tissue is attached to the membrane, thus there is zero velocity in the lower band. Similarly the lower edge of the central region must remain attached to the lower band and thus,

$$U = 0 \quad \text{at } x = 0. \tag{5.24}$$

The cells in the lower region are assumed quiescent and are packed at a high density. Therefore there will be no flux of cells into or out of the lower band into the central region. This imposes that,

$$N_{col}\, U = 0 \quad \text{and} \quad N_{gag}\, U = 0 \quad \text{at } x = 0. \tag{5.25}$$

Cells in the upper region are assumed to be proliferating and the newly formed daughter cells will be emitted into the central region. From the analysis of the experimental data we know this rate to be constant and thus the flux of cells across the upper boundary will be given by $F_{N_{pro}}$. The newly formed cells will be assumed to be solely of the collagen producing cell type. Therefore there will be no flux of GAG producing cells into or out of the central region. The flux of cells across the upper boundary is thus given by,

$$N_{col}\, U = N_{col}\, \dot{S} - F_{N_{pro}} \quad \text{and} \quad N_{gag}\, U = N_{gag}\, \dot{S} \quad \text{at } x = S(t). \tag{5.26}$$

The flux of cells into the top layer, $F_{N_{pro}}$ is a positive constant. Therefore when studying the characteristics of the equation (5.3) we observe there is an ingoing characteristic at the outer boundary. Thus we must specify a vale of the cell density at the boundary $S(t)$. To do this we shall assume the cells are emitted from the upper region surrounded by collagen at a density equal to that of the upper region. Therefore on the boundary between the central and upper region the extracellular volume fraction will be constant such that,

$$N_{col} + N_{gag} = N_{up} \quad \text{at } x = S(t), \tag{5.27}$$

where N_{up} is the density of the upper region.

The boundary condition for GAG producing cells, given in equation (5.26) can rewritten as,

$$N_{gag} \left(U - \dot{S} \right) = 0. \tag{5.28}$$

The flux of collagen cells into the central region is greater than zero. Therefore in the context of this model the only valid solution to equation (5.28) is that the density of GAG producing cells at the upper boundary is zero. This then imposes that the cells on the surface are collagen producing cells and by the boundary condition given in equation (5.27), the cells will be at constant density N_{up}. We can therefore rearrange the Neumann boundary for collagen

producing cells, given in equation (5.26), to give an equation for the height of the tissue, such that,

$$\dot{S} = U + \frac{F_{N_{pro}}}{N_{up}} \quad \text{at } x = S(t). \tag{5.29}$$

The pores in the Transwell are small relative to the diameter of a cell, thus there is no flux of cells across the boundary between the lower region and the Transwell. The boundary conditions along with the modelling equations for both cell types are shown in Figure 5.9, in which Δ_{pro} represents the height of the both the lower and upper bands and Δ_t represents the heights of the Transwell membrane.

The size of GAG molecules compared to the pores in the Transwell membrane is small. Thus GAG will be able to diffuse through the Transwell. The area available for the molecules to filter through in the Transwell membrane is less than the total area of membrane. Thus the membrane will provide a resistance to the flow of GAGs. Due to the short distances diffusion will take place on a shorter time scale than ECM production within the central region. Therefore the steady state diffusion equation can be imposed in the Transwell region, such that,

$$\Phi_t \frac{\partial^2 C_{gag}}{\partial x^2} = 0, \tag{5.30}$$

where Φ_t is the fraction of the membrane that is available for filtration.

In between the Transwell and the central region is the lower band. This region consists of a densely packed band of cells. The cells in this region are assumed quiescent and thus no GAG is produced in the lower band. Once again the time scale on which diffusion and consumption in this region take place will be small compared to ECM production within the central region, therefore the concentration of GAGs will be modelled using the steady state diffusion equation,

$$\Phi_{lo} \frac{\partial^2 C_{gag}}{\partial x^2} = 0, \tag{5.31}$$

where Φ_{lo} is the volume of extracellular space. The derivation of Φ_{lo} is the same as that given earlier for Φ. Thus in the lower region the extracellular volume fraction is defined by,

$$\Phi_{lo} = 1 - \frac{4}{3}\pi r^3 N_{lo}, \tag{5.32}$$

where N_{lo} denotes the density of cells in the lower band.

Above the central region is the upper band. This region is a highly dense band of proliferating cells. There will be no GAG production but GAG will be able to diffuse through this region.

Thus in the upper band the concentration of GAGs will be modelled by,

$$\frac{\partial}{\partial x}\left(\Phi_{up}\left(C_{gag}\,\dot{S}\,-\,D_{gag}\,\frac{\partial C_{gag}}{\partial x}\right)\right)\,=\,0, \tag{5.33}$$

where Φ_{up} is the volume of extracellular space in the upper region. The density of cell within this region is denoted by N_{up} and therefore the extracellular volume fraction in the upper band is defined as,

$$\Phi_{up}\,=\,1\,-\,\frac{4}{3}\pi\,r^3\,N_{up}. \tag{5.34}$$

The fluid surrounding the upper layer tissue and beneath the Transwell membrane is assumed to be well mixed, containing no cells, collagen, or GAG. GAG is not bound to the structure as strongly as collagen and thus will be washed away from the surface due to the mixing of the fluid above the top surface. Therefore the concentration of GAG on the top surface will equal zero. Therefore,

$$C_{gag}\,=\,0\quad\text{at } x\,=\,-\left(\Delta_t+\Delta_{pro}\right)\quad\text{and at } x\,=\,S(t). \tag{5.35}$$

The modelling equations and boundary conditions for cells, collagen and GAG are schematically shown in Figure 5.9.

The system of equations described in Figure 5.9 can be solved in the Transwell and the lower band with continuity of flux imposed at the interface. Solving equations (5.30) to (5.35) gives a flux condition at the lower boundary of the central region for GAG, such that,

$$\Phi\left(C_{gag}\,U\,-\,D_{gag}\,\frac{\partial C_{gag}}{\partial x}\right)\,=\,-\,D_{gag}\,\Phi_{lo}\,\frac{\Phi_t\,C_{gag}}{\Phi_{lo}\Delta_t+\Phi_t\Delta_{pro}}\quad\text{at } x\,=\,0. \tag{5.36}$$

The equivalent system of equations in the upper band provides a flux condition at the surface of the central region such that,

$$\Phi\left(C_{gag}\,U\,-\,D_{gag}\,\frac{\partial C_{gag}}{\partial x}\right)\,=\,\Phi_{up}\left(C_{gag}\,\dot{S}\,+\,\frac{\dot{S}C_{gag}}{\exp\left(\frac{\dot{S}\Delta_{pro}}{D_{gag}}\right)-1}\right)\quad\text{at } x\,=\,S(t). \tag{5.37}$$

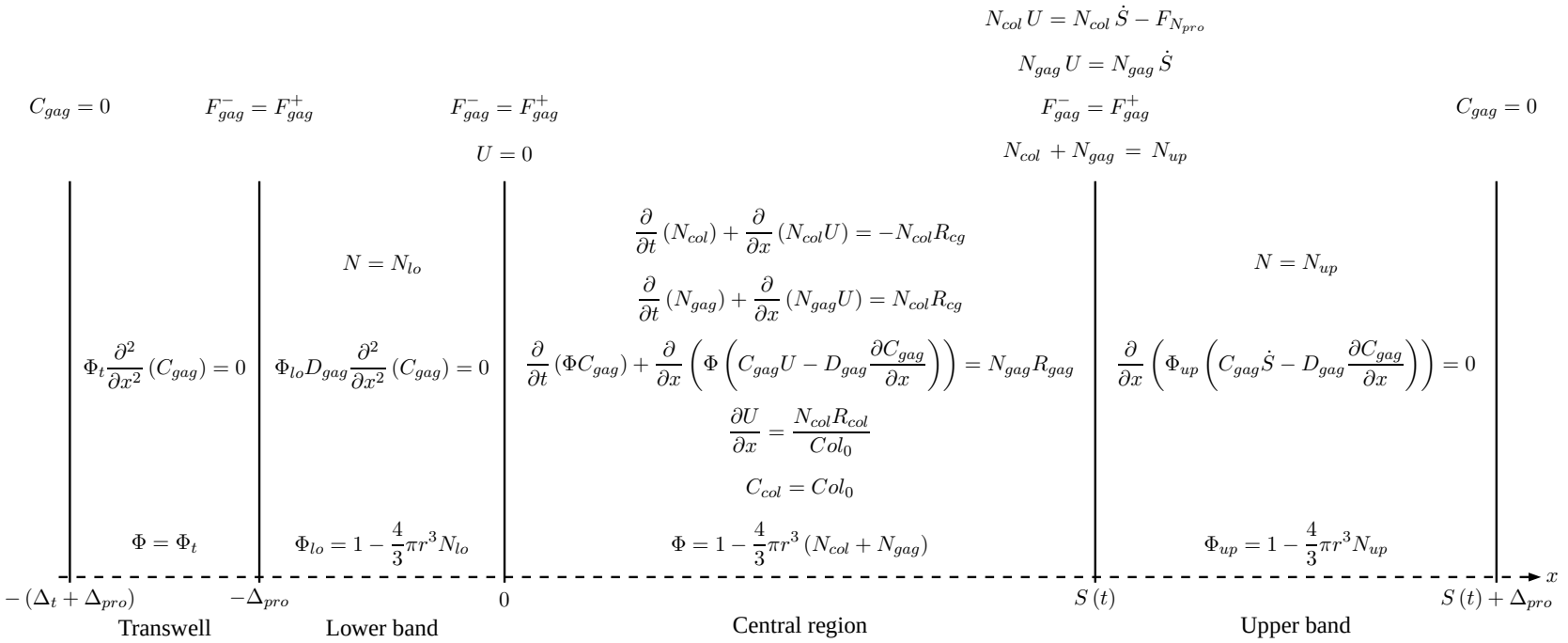

Figure 5.9: Schematic of the modelling equations.

5.6.5 Model simplifications

The model thus far contains very few unknown parameters. However the literature provides no information regarding how the rates of collagen and GAG production differ. Therefore for simplicity, and to avoid adding to the number of fitting parameters, we shall assume that a cell can synthesize one gram of glucose into one gram of ECM independent of the type of ECM being produced. Therefore the rates of collagen and GAG production are equal such that,

$$R_{col} \;=\; R_{gag} \;=\; R_{ecm}. \tag{5.38}$$

5.6.6 Full system of equations

Inside the central region, $0 < x < S(t)$, the model is given by,

$$\frac{\partial N_{col}}{\partial t} \;+\; \frac{\partial}{\partial x}\left(N_{col}\, U\right) \;=\; -\, N_{col}\, R_{cg}, \tag{5.39}$$

$$\frac{\partial N_{gag}}{\partial t} \;+\; \frac{\partial}{\partial x}\left(N_{gag}\, U\right) \;=\; N_{col}\, R_{cg}. \tag{5.40}$$

$$\frac{\partial U}{\partial x} \;=\; \frac{N_{col}\, R_{ecm}}{Col_0}, \tag{5.41}$$

$$\frac{\partial}{\partial t}\left(\Phi\, C_{gag}\right) \;+\; \frac{\partial}{\partial x}\left(\Phi\,\left(C_{gag}\, U \;-\; D_{gag}\,\frac{\partial C_{gag}}{\partial x}\right)\right) \;=\; N_{gag}\, R_{ecm}, \tag{5.42}$$

$$\Phi \;=\; 1 \;-\; \frac{4}{3}\,\pi\, r^3\,\left(N_{col} + N_{gag}\right). \tag{5.43}$$

The corresponding boundary conditions are such that at $x \;=\; 0$,

$$U \;=\; 0, \tag{5.44}$$

$$\Phi\,\left(C_{gag}\, U \;-\; D_{gag}\,\frac{\partial C_{gag}}{\partial x}\right) \;=\; -\, D_{gag}\,\Phi_{lo}\,\frac{\Phi_t\, C_{gag}}{\Phi_{lo}\Delta_t + \Phi_t \Delta_{pro}} \tag{5.45}$$

and at $x \;=\; S(t)$,

$$N_{col}\, U \;=\; N_{col}\,\dot{S} \;-\; F_{N_{pro}}, \tag{5.46}$$

$$N_{gag}\, U \;=\; N_{gag}\,\dot{S}, \tag{5.47}$$

$$\Phi\,\left(C_{gag}\, U \;-\; D_{gag}\,\frac{\partial C_{gag}}{\partial x}\right) \;=\; \Phi_{up}\,\left(C_{gag}\,\dot{S} \;-\; D_{gag}\,\left(\frac{-C_{gag}}{\Delta_{pro}}\right)\right), \tag{5.48}$$

$$N_{col} \;+ N_{gag} \;=\; N_{up}. \tag{5.49}$$

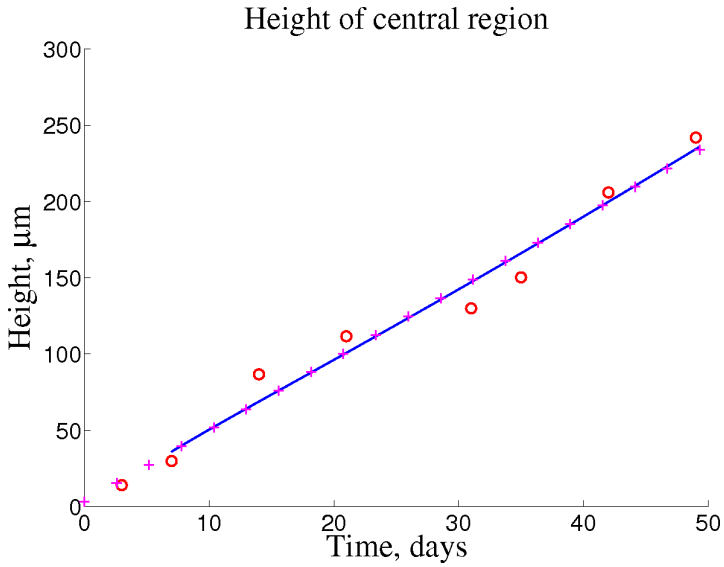

Figure 5.10: Height of the central region. Experimental data (o) and linear fit (+) are given alongside the modelling result (—).

The corresponding initial conditions are such that at $t = 0$,

$$N_{col} = \alpha_{cg} N_0, \quad N_{gag} = (1 - \alpha_{cg}) N_0, \quad C_{gag} = 0 \quad \text{and} \quad S = S_0. \tag{5.50}$$

5.6.7 Parameters and fitting

We shall now discuss the parameters used in the model and the derivation of those not available in the literature.

The wide variety of experimental and culture techniques means there is a large range of values for many of the parameters published in the literature. Where possible results for bovine articular cartilage have been used. The diffusion coefficient for GAGs given by Obradovic *et al.* [135] was implemented. However it should be noted that there is an error in the units published for the diffusion coefficient of GAGs in [135] and the corrected value, as given in Table 5.2, is then in agreement with Comper and Williams [31].

Glucose is a major ingredient for both ATP and ECM production. The proportion of glucose consumed to produce ATP compared to ECM is unknown in the literature. Due to the cells preference for anaerobic respiration the consumption of glucose for ATP will not be negligible. Therefore we shall define the proportion of glucose that is converted into ECM to be α_{ecm} and use this as a fitting parameter. There are a wide range of glucose consumption rates given in

Parameter		Value	Units
Cell differentiation rate	R_{cg}	$3.04{\cdot}10^{-6}$	s^{-1}
Initial ratio of cells	α_{cg}	0.101	
Proportion of glucose converted to ECM	α_{ecm}	0.610	

Table 5.3: Fitted parameters values.

the literature [134, 155, 192]. In this model we shall use the maximum rate given by Sengers [155].

The density of collagen was determined using the density of cartilage and percentage wet weight of collagen given by Freed *et al.* [47].

The dimensions of the Transwell membrane were taken from [116] and the dimensions and properties of the upper and lower bands were taken from the experimental data, as given in Section 5.3 and 5.4.

The remaining three parameters that could not be derived from the literature are; the cell differentiation rate, R_{cg}, the initial ratio collagen producing cells to GAG producing cells, α_{cg} and the proportion of glucose converted to ECM, α_{ecm}. These parameters were found by solving the model and comparing the results regarding the height of the tissue to that found experimentally. For this comparison the linear fit, as shown in Figure 5.6**A**, was used to represent the experimental data. The model was solved and the fitting achieved using MATLAB. The fitting used MATLAB's inbuilt function 'fminsearchbnd' as described in Section 2.4.8. The height of the central region and experimental data used in the fitting process are shown in Figure 5.10.

The numerical values for all known parameters are given in Table 5.1 and 5.2, whilst the fitted parameters are given in Table 5.3.

The model presented derives the concentration of GAG in g m^{-3}. However the experimental data is derived by staining tissue slices and detecting the intensity of light shone through the tissue. Finding the relationship between the relative distribution shown by the staining and the absolute density of GAG within the tissue is a common problem in biological analysis. We shall assume that the concentration of GAG and intensity of staining are linearly related. The scaling for this relation is unknown and may vary between experiments. Thus the distribution of GAG through the tissue will be compared to the data and the mass of GAG shall not be considered.

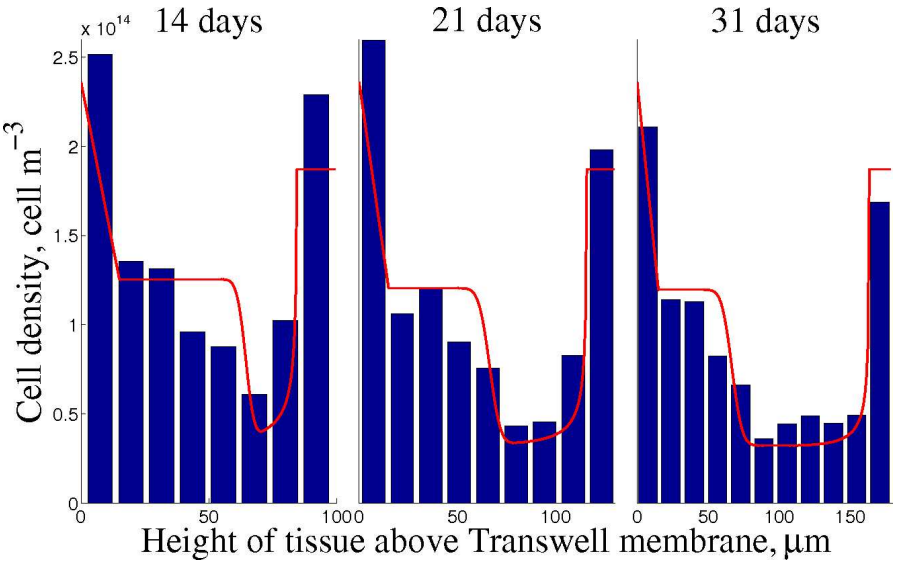

Figure 5.11: Density of cells within the central region at 14, 21 and 31 days. The histograms show the averaged experimental data, whilst the continuous line represents the results of the model.

5.7 Method and results

The system of modelling equations given in Section 5.6.6 were solved numerically in MATLAB, [174]. To incorporate the moving boundary the equations were transformed from the original expanding domain $x \in [0, S(t)]$ to a stationary coordinate frame, $\eta \in [0, 1]$, using the transformation $x = \eta S(t)$ and $t = \tau$. The transformed system of equations were then rearranged into conservation form. Using a finite difference method the system of partial differential equations were discretised centrally in space. The backward Euler method was then used to discretise in time before solving at each time step using Newton's method. At each iteration the Jacobian was updates using Broyden's method. The model was solved using two different methods. The first implemented the Neumann boundary conditions at $x = S(t)$, given in Section 5.6.6, whilst the second used the derived Dirichlet conditions discussed in Section 5.6.4 such that,

$$N_{col} = N_{up} \quad \text{and} \quad N_{gag} = 0 \quad \text{at } x = S(t). \tag{5.51}$$

Numerical errors prevented the two codes being identical. The Neumann boundary condition conserved mass accurately, but the density of collagen and GAG producing cells at the surface was not constant as derived in Section 5.6.4. Solving with Dirichlet boundary conditions imposed the density of the cells at the boundary. However this regime does not state the in flux of cells. This is only inferred by the Dirichlet boundary condition for collagen producing cells. This created errors in the conservation of cells, however by using small spacial steps this inaccuracy was reduced such that the relative increase in cells after forty-nine days was

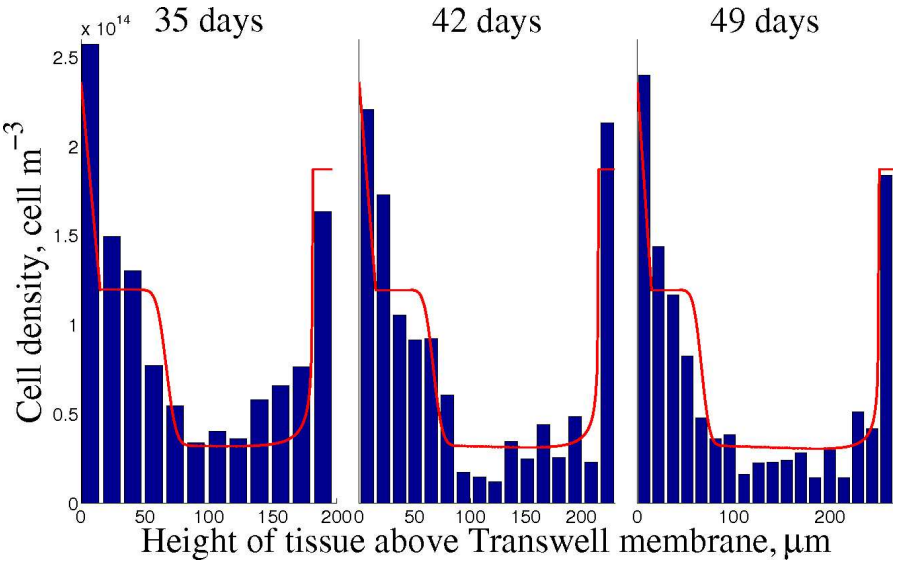

Figure 5.12: Density of cells within the central region at 35, 42 and 49 days. The histograms show the averaged experimental data, whilst the continuous line represents the results of the model.

less than 0.25%. The results from the code implementing Dirichlet conditions at the outer boundary are shown in this section.

The model presented determines the distribution of cells and GAGs, as well as the growth of the tissue structure. The tissue initially constitutes a highly dense region of cells that are producing collagen and GAG, causing the tissue to expand rapidly and the cell density to drop within the central region. Cell differentiation creates a region of predominantly GAG producing cells in the lower regions of the tissue, see Figure 5.14. Within this region collagen production is low and therefore the growth of the tissue is negligible, Figure 5.13. Above this region the flux of cells into the central region from the upper layer results in a population of cells that are predominantly producing collagen. Thus close to the upper layer the tissue continues to expand and the cell density continues to drop.

The influx of collagen producing cells beneath the upper band results in a population of cells close to the surface of the tissue predominantly consisting of collagen producing cells, Figure 5.13. The consequence of this is a region of growth, immediately beneath the upper band which is the sole contributor to the growth of the layer. Growth is now a function of the influx of cells and the rate of differentiation of cells from producing collagen to producing GAGs.

Figures 5.13 and 5.14 show that the cells in the lower and middle regions of the tissue have fully differentiated to cells that produce GAGs. This results in a high concentration of GAGs accumulating in the lower half of the tissue. GAGs are excreted from the tissue structure through both the upper and lower boundaries. However this is heavily restricted by the

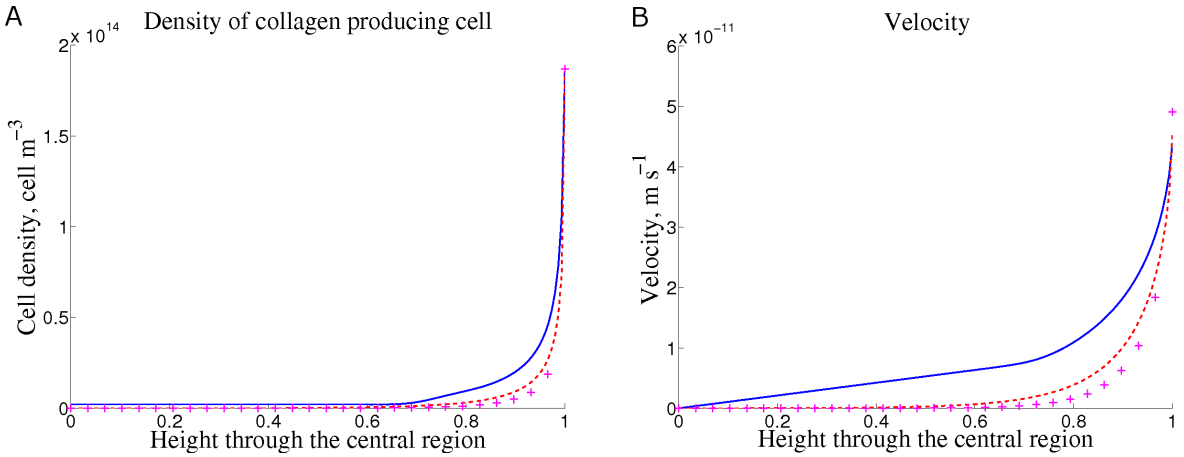

Figure 5.13: The density of cells producing collagen (**A**), and the velocity of growth (**B**) through the central region at 14 (—), 31 (- - -) and 49 days (+).

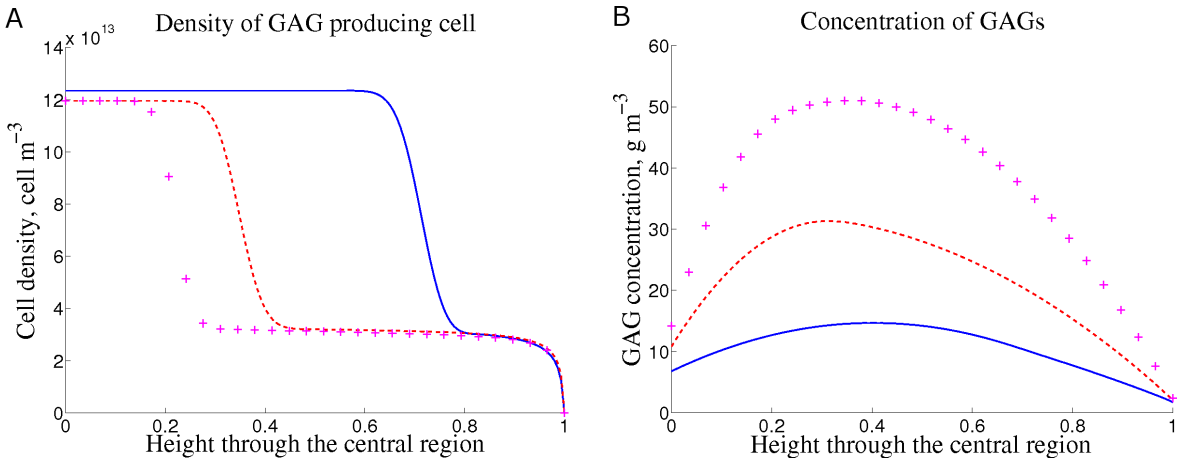

Figure 5.14: The density of cells producing GAGs (**A**) and the density of GAG (**B**) through the central region at 14 (—), 31 (- - -) and 49 days (+).

resistance due to the Transwell, the physical barrier created by the high cell density at the edges and the slow diffusional properties of GAG. The distribution of GAGs is shown to agree well with the experimental data at forty-nine days, Figure 5.15**A**. The maximum concentration of GAGs is shown to be closer to the Transwell membrane in the experimental data than given in the modelling predictions. This may indicate that the membrane is putting up a greater resistance than calculated, potentially being clogged by collagen and GAGs. Alternatively the cells in the lower half of the tissue and the lower band may be producing more GAGs than accommodated for by the model. Further investigation of cell behaviour in different environments would be required to draw more positive conclusions.

The mass of GAGs released by the tissue is shown to be higher than given by the experimental data, Figure 5.15**B**. Therefore the modelled production of GAGs by the tissue structure

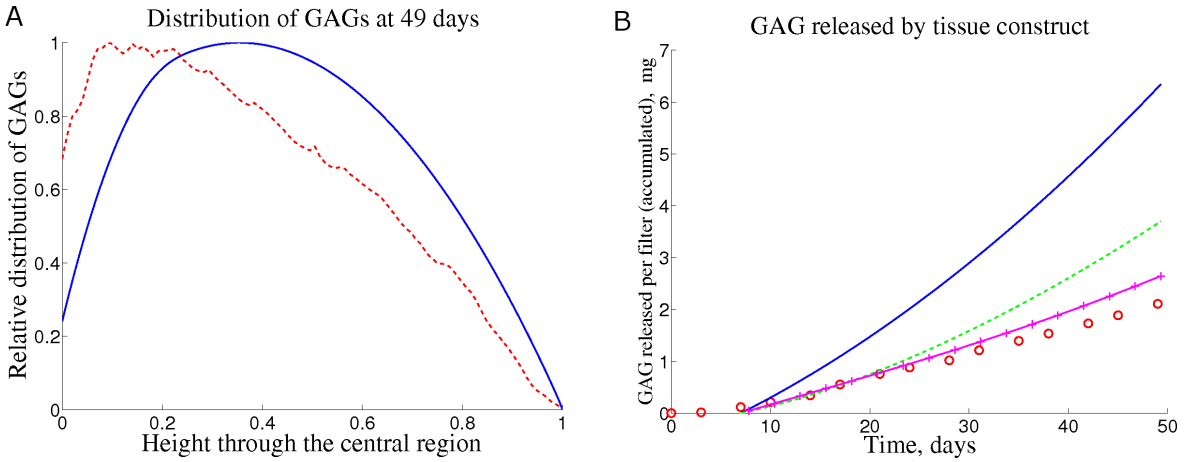

Figure 5.15: **A**: Distribution of GAG through the central region at 49 days (—) compared to experimental data (- - -). **B**: Total mass of GAG released from the tissue layer (—) alongside GAG released through the Transwell membrane (- - -), the upper surface (++) and experimental data (o).

should be lower. This may suggest the need to include quiescence in the model, which could be initiated by a number of factors including the density of GAG or the local cell density. Alternatively a further review of collagen production and the role of a cell in creating the tissue may suggest that the resources and number of cells dedicated to the production of GAGs is lower than previously accommodated.

Under this model the growth of the tissue layer is confined to a small region close to the upper surface. The size of this layer is defined by the differentiation rate of cells and is currently far less than the diffusion length of glucose. Therefore under the governing equations of the model presented, the growth would continue indefinitely. The central regions would never cease to produce GAGs and the tissue would be unaffected mechanisms such as cell death and ECM degradation. However for tissue structures of the size shown in this study, the structural integrity of the tissue should not be affected in this way and thus neglecting these factors does not affect the accuracy of the results of the model.

5.8 Discussion

Equine chondrocytes were cultured in monolayer structures to form cartilage layers. Samples of these constructs were then taken at regular intervals over a forty-nine day period. The samples were analysed to determine the distribution and density of cells, heights of the tissue layer, distribution of GAGs and the mass of GAG released from the structure. From these results a number of characteristics were observed. These included,

- A constant density of cells at both the lower and upper surfaces of the tissue.
- The lower region was inactive after fourteen days.
- Linear growth of the tissue layer.
- Linear increase in the number of cells.
- Linear increase in the accumulated mass of GAGs released from the tissue.
- The height of the tissue is insufficient to cause significant gradients in nutrients.

Based on these characteristics and the existing literature regarding tissue formation, a mathematical model was formulated that derived the density of cells, production of collagen, production of GAGs and the growth of the tissue layer. The effects of cell metabolism, cell differentiation, ECM production, nutrient transport and structural growth have all been considered.

The results of the model have shown that large regions of the tissue are inactive when it comes to proliferation and growth of the tissue layer. Cells in the lower half of the layer were shown to not proliferate and cease collagen production even at high concentrations of glucose. Only a relatively small region close to the upper surface contribute to the expansion of the tissue layer and the population of cells. The model predicted a quantity of GAG released from the tissue layer in excess of that seen experimentally. Thus the properties of GAG production must be reviewed for future work. Cells were said to differentiate from collagen producing cells to GAG producing cells. To improve the modelling of GAG production, a quiescent state of cells may need to be introduced and the relevant triggering mechanism determined. The release of GAGs from the structure could also be reviewed, with particular focus on the adhesion properties of GAG and the resistance of the lower membrane. In the current model the mixing of the outer medium is said to wash away all GAGs from the upper surface. GAGs may in fact adhere to each other, the surrounding cells and collagen fibers in a way that makes this boundary condition inaccurate. Similar effects may occur at the interface with the Transwell membrane and also cause the membrane to become clogged and thus further resist flow.

In this model we also assumed that cells either produce collagen or GAGs and never both simultaneously. This may be an inaccurate interpretation of the experiments. However if we consider a population of cells that is again divided up into collagen producing cells and GAG producing cells but in which cell differentiation is a forward and backward reaction at non

constant rates f_{cg} and f_{gc}, then conservation of mass imposes that,

$$\frac{\partial N_{col}}{\partial t} + \frac{\partial}{\partial x}\left(N_{col}\, U\right) = -f_{cg}\, N_{col} + f_{gc}\, N_{gag}, \tag{5.52}$$

$$\frac{\partial N_{gag}}{\partial t} + \frac{\partial}{\partial x}\left(N_{gag}\, U\right) = f_{cg}\, N_{col} - f_{gc}\, N_{gag}. \tag{5.53}$$

By adding these equations, this system can be rewritten as gives,

$$\frac{\partial N_{col}}{\partial t} + \frac{\partial}{\partial x}\left(N_{col}\, U\right) = -f_{cg}\, N_{col} + f_{gc}\, N_{gag}, \tag{5.54}$$

$$\frac{\partial N}{\partial t} + \frac{\partial}{\partial x}\left(N\, U\right) = 0, \tag{5.55}$$

where,

$$N = N_{col} + N_{gag}. \tag{5.56}$$

However consider the general case where cell differentiation happens on a time scale $\epsilon\tau$,such that the non dimensional equation give,

$$\epsilon\left(\frac{\partial \hat{N}_{col}}{\partial \hat{t}} + \frac{\partial}{\partial \hat{x}}\left(\hat{N}_{col}\,\hat{U}\right)\right) = -\hat{f}_{cg}\,\hat{N}_{col} + \hat{f}_{gc}\,\hat{N}_{gag}, \tag{5.57}$$

$$\frac{\partial \hat{N}}{\partial \hat{t}} + \frac{\partial}{\partial \hat{x}}\left(\hat{N}\,\hat{U}\right) = 0. \tag{5.58}$$

In the present model the time scale on which cell differentiation takes place is comparable to that of the growth of the tissue layer, where ϵ is order one. This suggests the cells remember whether they have previously been making collagen or GAGs and will have to convert to the other form when required. However by taking ϵ to be small implies that equation (5.57) can be reduced to,

$$\hat{N}_{col} = f\,\hat{N}_{gag}, \tag{5.59}$$

where f is an unknown function that determines the relative amount of collagen and GAG made. This simplified equation now states that the cells do not remember what they have been producing but simply react to the current situation. The cell density is now modelled as just a single population of cells, with density N and the N_{col} and N_{gag} give the proportion of collagen and GAGs that are made. This simplified model may give a better representation of the experimental observations.

In this chapter we have presented a model that simulates the growth of a layer of cartilage tissue. The model deduced that cell activity was not defined by nutrient concentration gradients, as these were absent throughout the tissue structure. Instead it was shown that the position of the cell within the tissue layer determined the role of the cell and thus the rate of growth and distribution of ECM. The ultimate aim of such a model would be to optimize

the *in vitro* growth procedure. At present it is not obvious which parameters are dominant and thus would require adjusting. To derive this we require a better understanding of cell activity, particularly at differing cell densities, nutrient concentrations and positions within the structure; both in terms of distance from a boundary and with respect to the contents of the surrounding ECM. From this we should gain a better understanding of the mechanisms at work, such as cell metabolism, quiescence, necrosis and mechanical forces. This will then allow us to revise our model and either modify or give further justification to the assumptions we have made, such as the density of collagen being constant.

Chapter 6

Conclusions

The first part of this thesis focused on the modelling and characteristics of a multicellular tumour spheroid. We were particularly interested in how the energy demands of a cell are affected by its local environment and how this in turn affects the cell cycle and subsequent growth of the tumour. We constructed a multispecies model that accounted for metabolic reactions alongside chemical and ionic buffering reactions. In addition to diffusion, this model also included the effects of charge migration on ionic species. The model showed that the ATP demand of a cell are dependent on the concentration of oxygen and glucose within its local environment. One of the notable findings was that the concentration of waste products has a negligible effect on the cell cycle. In particular we showed that the concentration of glucose restricted the growth of the tumour, whilst the level of oxygen determined the contributions of aerobic and anaerobic respiration in producing ATP. The switch over from aerobic respiration to anaerobic respiration was also shown to determine when a cell changes from being proliferative to quiescent. Low concentrations of glucose reduced the cells capability for ATP production and thus promoted necrosis.

The results of the modelling showed that diffusion was the dominant transport mechanism within the tumour. The gradients in electric potential were small throughout and waste materials diffused out of the tumour spheroid before significant quantities could accumulate. It was thus shown that the any model of tumour growth must include both oxygen and glucose and only diffusion need be considered as a transport mechanism. These conclusions were then used to develop a simplified model of tumour growth, which only contained these essential elements. This simplified model gave results comparable with that of the full model, but is more accessible and appropriate for further applications; for example studying drug delivery. In Chapter 3 we chose to use the simplified model of tumour growth to study the mechanical forces that develop within growing tissue. In both the full and simplified models of tumour growth, presented in Chapter 2, the effects of residual stresses had been neglected. The aim

of Chapter 3 was to see if this simplification was appropriate or whether the forces that build up during growth could potentially affect whether a cell is proliferative, quiescent or necrotic. A full investigation into the effects of mechanical forces on cells was beyond the scope of this thesis. However we have explored how the sensitivity of the direction of growth of a cell is dependent on the local stress field.

A morphoelastic model was implemented that assumed the tumour was made up of an incompressible elastic material. Varying degrees of sensitivity of growth to the local stress field were considered. In all cases necrosis was shown to be the largest factor in creating residual stress. The onset of necrosis caused the centre of the spheroid to collapse, pulling in surrounding cells and creating large tensile forces. This was particular apparent where the direction of growth was highly sensitive to stress. The creation of a necrotic core caused the cells to divide along the radial axis. Thus large radial forces were generated pulling the cells in towards the centre, whilst large circumferential stresses were generated as the cells tried to stay attached to their neighbours. It was thus shown that the role of mechanical forces in the growth of a tumour spheroid are important and should not be neglected.

To aid the analysis of the tumour mechanics model we only considered the case of an incompressible material. In this limit the growth model and mechanics model can be decoupled and therefore solved separately. An interesting extension to this work would be to consider a tumour with a lower Poisson's ratio and include the effects of mechanics in the growth of a compressible tumour spheroid. This coupled problem would not just show how stresses build up during growth but also the effects they have on growth, in both a physical sense and in determining a cells position within the cell cycle.

An application of the mechanics model was used to derive the deformation of a tumour that has been sliced in half, at the radius at which the centre became necrotic. At present this is only a theoretical application. However in future this can easily be compared to experimental results. It was shown that necrosis was causing the centre of the spheroid to collapse in on itself, dragging in the cells from the surrounding regions. The region close to the surface were shown to expand, releasing the circumferential compressive forces they were previously under.

Predominantly, mathematical models of tumour growth have been based on conservation of mass, formulated by viewing a tumour from a macroscopic view point. The validity of these equations, governing the nutrient transport and consumption was reviewed by deriving alternative equations in Chapter 4. The microscopic behaviour was studied and used to derive governing equations on a macroscopic level, using homogenization theory. The derived equations included directional preference for nutrient transport, that showed the effective diffusion rate to be dependent on the the volume and shape of the extracellular space available. However, the newly derived diffusion coefficient was shown to be larger than that found experimentally. The cells and extracellular matrix are thus impeding the flow more than that theoretically

calculated. Further investigation into the matrix and cell structure is required to refine the problem and develop a more accurate model.

The second part of this thesis, Chapter 5, developed a model for the growth of a layer of cartilage tissue. This was motivated by experimental results provided by Jos Malda and Wouter Schuurman. The aim of this study was to explain the distribution of cells and extracellular matrix throughout the tissue construct over time. In future this could then be used to optimise the experimental methods and grow cartilage structures similar to those found *in vivo*. The model was based on experimental data grown from equine chondrocytes which showed the behaviour of the cells to be dependent on their location within the tissue structure. Cells on the upper and lower boundaries were shown to stay attached to the boundary and not separate away from each other. It was thus assumed these cells do not synthesize extracellular matrix. Cells in the central region were also shown to be mostly quiescent with only a relatively small region of cells below the top surface contributing to the growth of the tissue layer. An important, and maybe surprising aspect of this model, was that the concentration of neither oxygen nor glucose was required in determining the cell cycle state. The experiments had taken place in glucose rich environments and on length scales in which diffusion was not limiting. Thus the cells were exposed to glucose and oxygen such that their energy requirements could be consistently met. Therefore the growth must be impeded by other mechanisms. In this work we imposed that growth was determined by the position of a cell within the tissue layer. Establishing which mechanisms are responsible for cell state and growth rates would be an interesting extension to this work. In particular conducting a similar experiment with a lower concentration of glucose in the surrounding medium could shed light on what determines whether a cell synthesizes extracellular matrix, proliferates or is quiescent. Similarly studying the behaviour of cells at various cell densities and at varying distances from surfaces would be useful in determining how cells construct cartilage.

In conclusion we have shown that by stripping biological processes back to their simplest forms we can derive mathematical models that accurately replicate what has been seen during *in vitro* experiments. Whilst doing this, new scientific knowledge is synthesized and has shown that both metabolism and mechanical forces play an important part in tumour growth, whilst cell signalling and the surrounding structural environment determines the growth of a tissue layer. There are a wide variety of applications for both the tumour and tissue models. However the importance of well defined and understood experimental data should not be overlooked. It is essentially impossible to produce a model for all cell types, but with knowledge of the metabolic pathways and cell characteristics the modelling framework suggested in this thesis can be adapted to a large range of experiments.

Appendix A

Nondimensional analysis of full tumour model

The concentrations of oxygen, glucose, carbon dioxide, hydrogen, chlorine and sodium were scaled with respect to that found in the surrounding medium, such that,

$$C_i = C_{\infty_i} \bar{C}_i, \tag{A.1}$$

where the values of C_{∞_i} are given in Table 2.2. The length scale was chosen such that the effect of the transport of oxygen due to diffusion balanced the production of oxygen. This gives,

$$r = r_\infty \, \bar{r} \qquad \text{where} \qquad r_\infty = \sqrt{\frac{C_{\infty_{ox}} \, D_{ox}}{\rho \, R_{ox}}}. \tag{A.2}$$

The concentration of lactate and bicarbonate were then scaled by balancing the diffusion terms with the dominant production terms in their respective governing equations. The resulting scalings give,

$$C_{\infty_{la}} = \frac{\rho \, R_{ox} \, r_\infty^2}{D_{la}} \qquad \text{and} \qquad C_{\infty_{bi}} = \frac{C_{\infty_{cd}} \, k_f \, r_\infty^2}{D_{bi}}. \tag{A.3}$$

Time was scaled by the growth rate given in equation (2.66), such that,

$$t = \frac{1}{K_M} \, \bar{t}. \tag{A.4}$$

The electric potential was scaled using the maximum value for the electric potential gradient seen in the results for the full model, shown in Figure 2.11. Thus,

$$\Phi = \Phi_\infty \, r_\infty \, \bar{\Phi} \qquad \text{where} \qquad \Phi_\infty \, r_\infty^{-1} = 10^{-3}. \tag{A.5}$$

Lastly the desired energy production rate will be scaled by the rate of maximum oxygen consumption, such that,

$$P_{atp} \;=\; R_{ox}\,\rho\,\bar{P}_{atp}. \tag{A.6}$$

The production terms can now be nondimensionalised such that the production of oxygen is,

$$P_{ox} \;=\; P_{\infty_{ox}}\bar{P}_{ox} \tag{A.7}$$

where,

$$P_{\infty_{ox}} \;=\; R_{ox}\,\rho \qquad \text{and} \qquad \bar{P}_{ox} = -\min\left(\frac{6}{38}\bar{P}_{atp}\,,\,\bar{P}_{ox}^{max}\right). \tag{A.8}$$

The remaining production terms are,

$$\begin{aligned}
P_{gl} &= P_{\infty_{ox}}\left(\frac{1}{6}\bar{P}_{ox} \;-\; \frac{1}{2}\left(\bar{P}_{atp} + \frac{6}{38}\bar{P}_{ox}\right)\right), && \text{(A.9)}\\
P_{cd} &= -\,P_{\infty_{ox}}\bar{P}_{ox} \;+\; k_r C_{\infty_{bi}} C_{\infty_{hy}} \bar{C}_{bi}\bar{C}_{hy} \;-\; k_f C_{\infty_{cd}}\bar{C}_{cd}, && \text{(A.10)}\\
P_{la} &= -2P_{\infty_{ox}}\left(\bar{P}_{gl} - \frac{1}{6}\bar{P}_{ox}\right), && \text{(A.11)}\\
P_{hy} &= -2P_{\infty_{ox}}\left(\bar{P}_{gl} - \frac{1}{6}\bar{P}_{ox}\right) \;-\; k_r C_{\infty_{bi}} C_{\infty_{hy}} \bar{C}_{bi}\bar{C}_{hy} \;+\; k_f C_{\infty_{cd}}\bar{C}_{cd}, && \text{(A.12)}\\
P_{bi} &= k_f C_{\infty_{cd}}\bar{C}_{cd} \;-\; k_r C_{\infty_{bi}} C_{\infty_{hy}} \bar{C}_{bi}\bar{C}_{hy}, && \text{(A.13)}\\
P_{ch} &= 0. && \text{(A.14)}
\end{aligned}$$

We now factor out the largest expression in each of these production terms and relabel each constant by P_{∞_i}. We thus can rewrite the production terms as,

$$\begin{aligned}
P_{ox} &= P_{\infty_{ox}}\bar{P}_{ox}, && \text{(A.15)}\\
P_{gl} &= P_{\infty_{gl}}\left(\frac{1}{6}\bar{P}_{ox} \;-\; \frac{1}{2}\left(\bar{P}_{atp} + \frac{6}{38}\bar{P}_{ox}\right)\right), && \text{(A.16)}\\
P_{cd} &= P_{\infty_{cd}}\left(-\,\sigma\bar{P}_{ox} \;+\; \psi\bar{C}_{bi}\bar{C}_{hy} \;-\; \bar{C}_{cd}\right), && \text{(A.17)}\\
P_{la} &= P_{\infty_{la}}\left(-2\left(\bar{P}_{gl} - \frac{1}{6}\bar{P}_{ox}\right)\right), && \text{(A.18)}\\
P_{hy} &= P_{\infty_{hy}}\left(-2\sigma\left(\bar{P}_{gl} - \frac{1}{6}\bar{P}_{ox}\right) \;-\; \psi\bar{C}_{bi}\bar{C}_{hy} \;+\; \bar{C}_{cd}\right), && \text{(A.19)}\\
P_{bi} &= P_{\infty_{bi}}\left(\bar{C}_{cd} \;-\; \sigma\bar{C}_{bi}\bar{C}_{hy}\right), && \text{(A.20)}\\
P_{ch} &= P_{\infty_{ch}}, && \text{(A.21)}
\end{aligned}$$

Species	α_i	β_i	γ_i
Oxygen	$1.75 \cdot 10^{-4}$	0	1
Glucose	$2.63 \cdot 10^{-3}$	0	0.57
Carbon dioxide	$2.22 \cdot 10^{-4}$	0	2.18
Lactate	$1.55 \cdot 10^{-3}$	-10^{-3}	1
Hydrogen	$1.30 \cdot 10^{-5}$	10^{-3}	$2.94 \cdot 10^{3}$
Bicarbonate	$2.85 \cdot 10^{-4}$	-10^{-3}	1
Chloride	$1.31 \cdot 10^{-3}$	-10^{-3}	0

Table A.1: Nondimensional constants.

where,

$$\sigma = \frac{R_{ox}\,\rho}{k_f\,C_{\infty_{cd}}} \qquad \text{and} \qquad \psi = \frac{k_r\,C_{\infty_{bi}}C_{\infty_{hy}}}{k_f\,C_{\infty_{cd}}}. \tag{A.22}$$

Individual terms in the expressions for production rates will not be considered. Only the largest terms will be used for each species. Therefore the non dimensional production rates will be given by,

$$P_i = P_{\infty_i}\,\bar{P}_i. \tag{A.23}$$

The nondimensional form of equation (2.67) can now be written as,

$$K_M C_{\infty_i}\frac{\partial \bar{C}_i}{\partial t} + \frac{C_{\infty_i}}{\bar{r}^2}\frac{\partial}{\partial \bar{r}}\left(\bar{r}^2\left(K_M \bar{C}_i \bar{U} - \frac{D_i}{r_\infty^2}\left(\frac{\partial \bar{C}_i}{\partial \bar{r}} + z_i \Phi_\infty C_i \frac{\partial \bar{\Phi}}{\partial \bar{r}}\right)\right)\right) = P_{\infty_i}\,\bar{P}_i. \tag{A.24}$$

This can be rearranged to give,

$$\alpha_i\frac{\partial \bar{C}_i}{\partial t} + \frac{1}{\bar{r}^2}\frac{\partial}{\partial \bar{r}}\left(\bar{r}^2\left(\alpha_i \bar{C}_i \bar{U} - \left(\frac{\partial \bar{C}_i}{\partial \bar{r}} + \beta_i\,C_i \frac{\partial \bar{\Phi}}{\partial \bar{r}}\right)\right)\right) = \gamma_i\,\bar{P}_i, \tag{A.25}$$

where

$$\alpha_i = \frac{K_M\,r_\infty^2}{D_i}, \qquad \beta_i = z_i\,\Phi_\infty \qquad \text{and} \qquad \gamma_i = \frac{P_{\infty_i}\,r_\infty^2}{C_{\infty_i}\,D_i}. \tag{A.26}$$

The numerical values of α_i, β_i, and γ_i are given in Table A.1.

Appendix B

Nondimensional analysis of full tumour model

To analyse the error in the numerical codes used in solving the tumour models in Chapter 2 and tissue model in Chapter 5 the convergence of each code was derived. As a representation of this analysis the error in the simplified tumour model given in Section 2.5 is given. The model was solved using 5, 10, 20 and 40 grid points and the separate results were compared to the results of the model solved using 80 grid points. The error was then derived by calculating the relative error using 2-norm. These error values have been plotted against the number of spacial grid points on a log-log scale. A linear fit was then made of all the error values and of just the last three. These fitted lines are show to agree well with the data and have a gradient with magnitude of approximately 2. This coincides with the error of the finite difference method used where the error is proportional to the spatial step squared. The time stepping was achieved using an adaptive scheme such that the relative change in the solution stayed constant. An analysis of the error of the time stepping has thus not been given.

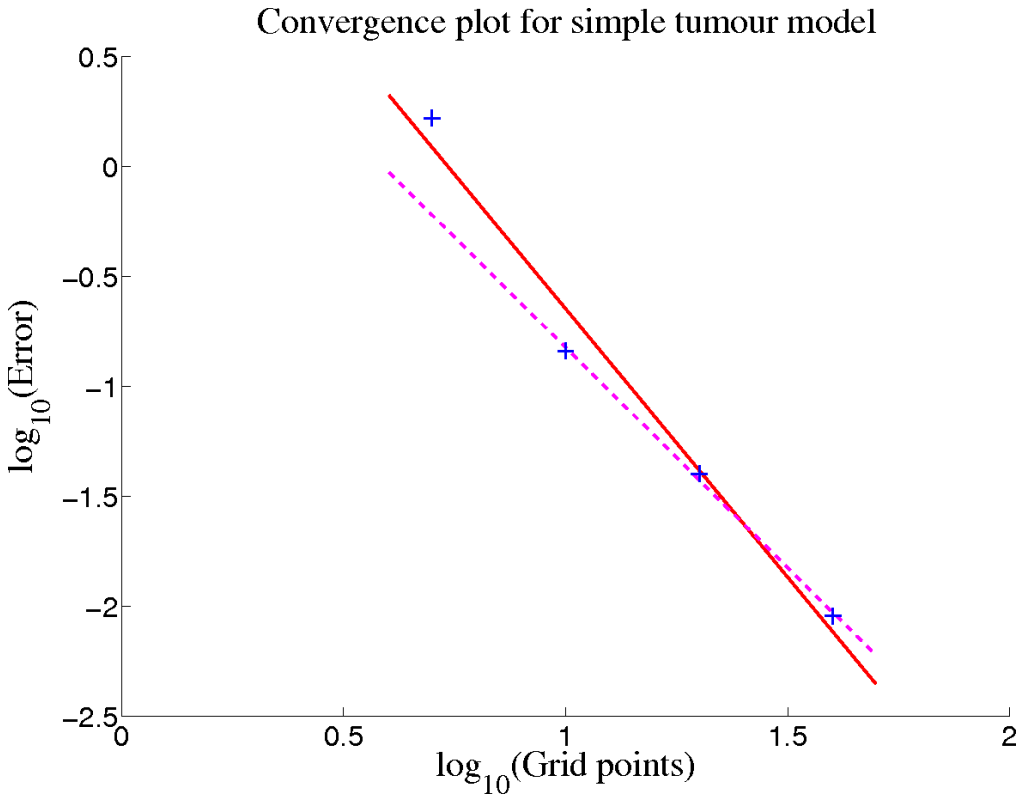

Figure B.1: Convergence plot of the finite difference code used to solve the simplified tumour model in Chapter 2. The log of the error when solving the model using 5, 10, 20 and 40 grid points compared to the result using 80 grid points is shown (+) against a fit of all four error points (—) and a fit of the final three error points (- - -). The corresponding gradients of the fitted curves are -2.441 and -2.003.

Appendix C

Tissue images

Photographic images of the stained tissue slices used for analysis in Chapter 5 are given on the CD-ROM attached to the back cover of this thesis. The original images and the cropped images, as described in Section 5.3.2, are both given. Slices of the tissue are given at 3, 7, 14, 21, 31, 35, 42 and 49 days and the images are labelled accordingly. Multiple slices were taken at each time point and this in indicated in the file name. Some slices were cropped into multiple samples, these are indicated by the letter 'B' being added to the end of their file name.

A copy of this thesis is also given on the CD-ROM as a .pdf file.

Bibliography

[1] E.L. Allgower and K. Georg. *Introduction to Numerical Continuation Methods*. Society for Industrial Mathematics, 2003.

[2] D. Ambrosi and F. Guana. Stress-modulated growth. *Mathematics and Mechanics of Solids*, 12(3):319–343, 2007.

[3] D. Ambrosi, A. Guillou, and E.S. Di Martino. Stress-modulated remodeling of a non-homogeneous body. *Biomechanics and Modeling in Mechanobiology*, 7(1):63–76, 2008.

[4] D. Ambrosi and F. Mollica. On the mechanics of a growing tumor. *International Journal of Engineering Science*, 40(12):1297–1316, 2002.

[5] D. Ambrosi and F. Mollica. The role of stress in the growth of a multicell spheroid. *Journal of Mathematical Biology*, 48(5):477–499, 2004.

[6] A.R.A. Anderson, K.A. Rejniak, P. Gerlee, and V. Quaranta. Microenvironment driven invasion: a multiscale multimodel investigation. *Journal of Mathematical Biology*, 58(4):579–624, 2009.

[7] W. Ando, K. Tateishi, D.A. Hart, D. Katakai, Y. Tanaka, K. Nakata, J. Hashimoto, H. Fujie, K. Shino, H. Yoshikawa, and N. Nakamura. Cartilage repair using an in vitro generated scaffold-free tissue-engineered construct derived from porcine synovial mesenchymal stem cells. *Biomaterials*, 28(36):5462–5470, 2007.

[8] R.P. Araujo and D.L.S. McElwain. A history of the study of solid tumour growth: the contribution of mathematical modelling. *Bulletin of Mathematical Biology*, 66(5):1039–1091, 2004.

[9] R.P. Araujo and D.L.S. McElwain. A linear-elastic model of anisotropic tumour growth. *European Journal of Applied Mathematics*, 15(03):365–384, 2004.

[10] M. Ben Amar and A. Goriely. Growth and instability in elastic tissues. *Journal of the Mechanics and Physics of Solids*, 53(10):2284–2319, 2005.

[11] A. Berk, S.L. Zipursky, P. Matsudaira, D. Baltimore, J. Darnell, and H. Lodish. *Molecular Cell Biology*. New York, WH Freeman, 1999.

[12] S.R.S. Bibby, D.A. Jones, R.M. Ripley, and J.P.G. Urban. Metabolism of the intervertebral disc: Effects of low levels of oxygen, glucose, and pH on rates of energy metabolism of bovine nucleus pulposus cells. *Spine*, 30(5):487–496, 2005.

[13] G. Bock and J. Goode, editors. *Tissue Engineering of Cartilage and Bone*. Wiley, 2003.

[14] C.J.W. Breward, H.M. Byrne, and C.E. Lewis. The role of cell-cell interactions in a two-phase model for avascular tumour growth. *Journal of Mathematical Biology*, 45(2):125–152, 2002.

[15] C.J.W. Breward, H.M. Byrne, and C.E. Lewis. A multiphase model describing vascular tumour growth. *Bulletin of Mathematical Biology*, 65(4):609–640, 2003.

[16] M. Brittberg, L. Peterson, E. Sjogren-Jansson, T. Tallheden, and A. Lindahl. Articular cartilage engineering with autologous chondrocyte transplantation: A review of recent developments. *The Journal of Bone and Joint Surgery*, 85(3):109–115, 2003.

[17] C.G. Broyden. A class of methods for solving nonlinear simultaneous equations. *Mathematics of Computation*, 19(92):577–593, 1965.

[18] A.C. Burton. Rate of growth of solid tumours as a problem of diffusion. *Growth*, 30(2):157–176, 1966.

[19] D.L. Butler, S.A. Goldstein, and F. Guilak. Functional tissue engineering: the role of biomechanics. *Journal of Biomechanical Engineering*, 122:570–575, 2000.

[20] H.M. Byrne. The effect of time delays on the dynamics of avascular tumor growth. *Mathematical Biosciences*, 144(2):83–117, 1997.

[21] H.M. Byrne and M.A.J. Chaplain. Growth of nonnecrotic tumors in the presence and absence of inhibitors. *Mathematical Biosciences*, 130(2):151–181, 1995.

[22] J.J. Casciari. *The effects of the diffusion and reaction of nutrients and metabolic waste products on the growth and microenvironment of multicellular tumor spheroids*. PhD thesis, University of Rochester, Rochester, NY, 1989.

[23] J.J. Casciari, S.V. Sotirchos, and R.M. Sutherland. Glucose diffusivity in multicellular tumor spheroids. *Cancer Research*, 48(14):3905–3909, 1988.

[24] J.J. Casciari, S.V. Sotirchos, and R.M. Sutherland. Mathematical-modeling of microenvironment and growth in EMT6/Ro multicellular tumour spheroids. *Cell Proliferation*, 25(1):1–22, 1992.

[25] C.J. Catt, D. Friedrich, and S. Naire. Modelling of the growth of engineered orthopaedic tissue in zero force and variable load environments. http://www.maths-in-medicine.org/uk/2008/orthopaedic-tissue, July 2009.

[26] J. Chaudhuri and M. Al-Rubeai. *Bioreactors for Tissue Engineeering: Principles, Design and Operation*. Springer, 2005.

[27] C.Y. Chen, H.M. Byrne, and J.R. King. The influence of growth-induced stress from the surrounding medium on the development of multicell spheroids. *Journal of Mathematical Biology*, 43(3):191–220, 2001.

[28] G. Cheng, J. Tse, R.K. Jain, and L.L. Munn. Micro-environmental mechanical stress controls tumor spheroid size and morphology by suppressing proliferation and inducing apoptosis in cancer cells. *PLoS ONE*, 4(2):e4632, 2009.

[29] D. Cioranescu and P. Donato. *An Introduction to Homogenization*, volume 17. Oxford Science Publications, 1999.

[30] C.C. Clark, B.S. Tolin, and C.T. Brighton. The effect of oxygen tension on proteoglycan synthesis and aggregation in mammalian growth plate chondrocytes. *Journal of Orthopaedic Research*, 9(4):477–484, 1991.

[31] W.D. Comper and R.P. Williams. Hydrodynamics of concentrated proteoglycan solutions. *Journal of Biological Chemistry*, 262(28):13464–13471, 1987.

[32] COMSOL, Inc. COMSOL-Multiphysics, 2007.

[33] J.H. Conway and N.J.A. Sloane. *Sphere packings, lattices, and groups*, volume 290 of *Grundlehren der mathematischen Wissenschaften*. Springer Verlag, 3rd edition, 1998.

[34] S.C. Cowin. Tissue growth and remodeling. *Annual Review of Biomedical Engineering*, 6:77–107, 2004.

[35] H.G. Crabtree. The carbohydrate metabolism of certain pathological overgrowths. *Biochemical Journal*, 22(5):1289–1297, 1928.

[36] H.G. Crabtree. Observations on the carbohydrate metabolism of tumours. *Biochemical Journal*, 23(3):536–544, 1929.

[37] S. Cui. Analysis of a mathematical model for the growth of tumors under the action of external inhibitors. *Journal of Mathematical Biology*, 44(5):395–426, 2002.

[38] A. Curtis and M. Riehle. Tissue engineering: the biophysical background. *Physics in Medicine and Biology*, 46:R47–R65, 2001.

[39] C.V. Dang and G.L. Semenza. Oncogenic alterations of metabolism. *Trends in Biochemical Sciences*, 24(2):68–72, 1999.

[40] R.L. David. *CRC Handbook of Chemistry and Physics*. Internet Version, Taylor and Francis, Boca Raton, FL, 87th edition edition, 2007.

[41] C.de L. Davies, D.A. Berk, A. Pluen, and R.K. Jain. Comparison of IgG diffusion and extracellular matrix composition in rhabdomyosarcomas grown in mice versus in vitro as spheroids reveals the role of host stromal cells. *British Journal of Cancer*, 86(10):1639–1644, 2002.

[42] M.A. DiMicco and R.L. Sah. Dependence of cartilage matrix composition on biosynthesis, diffusion, and reaction. *Transport in Porous Media*, 50(1):57–73, 2003.

[43] C. Domm, M. Schunke, K. Christesen, and B. Kurz. Redifferentiation of dedifferentiated bovine articular chondrocytes in alginate culture under low oxygen tension. *Osteoarthritis and Cartilage*, 10(1):13–22, 2002.

[44] D. Eyre. Collagen of articular cartilage. *Arthritis Research*, 4(1):30–35, 2002.

[45] S.J. Ferguson, K. Ito, and L.P. Nolte. Fluid flow and convective transport of solutes within the intervertebral disc. *Journal of Biomechanics*, 37(2):213–221, 2004.

[46] World Health Organisation: International Agency for Research on Cancer. Globocan 2008: Cancer incidence and mortality worldwide in 2008. http://globocan.iarc.fr/, August 2010.

[47] L.E. Freed, A.P. Hollander, I. Martin, J.R. Barry, R. Langer, and G. Vunjak-Novakovic. Chondrogenesis in a cell-polymer-bioreactor system. *Experimental Cell Research*, 240(1):58–65, 1998.

[48] L.E. Freed, R. Langer, I. Martin, N.R. Pellis, and G. Vunjak-Novakovic. Tissue engineering of cartilage in space. *Proceedings of the National Academy of Sciences*, 94(25):13885–13890, 1997.

[49] L.E. Freed, I. Martin, and G. Vunjak-Novakovic. Frontiers in tissue engineering: In vitro modulation of chondrogenesis. *Clinical Orthopaedics and Related Research*, 367:S46–S58, 1999.

[50] J.P. Freyer. *Heterogeneity in multicell spheroids induced by alterations in the external oxygen and glucose concentration*. PhD thesis, University of Rochester, Rochester, NY, 1981.

[51] J.P. Freyer. Rates of oxygen consumption for proliferating and quiescent cells isolated from multicellular tumor spheroids. *Advances in Experimental Medicine and Biology*, 345:335–242, 1994.

[52] J.P. Freyer. Decreased mitochondrial function in quiescent cells isolated from multicellular tumor spheroids. *Journal of Cellular Physiology*, 176(1):138–149, 1998.

[53] J.P. Freyer and P.L. Schor. Regrowth kinetics of cells from different regions of multicellular spheroids of four cell lines. *Journal of Cellular Physiology*, 138(2):384–392, 1989.

[54] J.P. Freyer and R.M. Sutherland. A reduction in the in situ rates of oxygen and glucose consumption of cells in EMT6/Ro spheroids during growth. *Journal of Cellular Physiology*, 124:516–524, 1985.

[55] J.P. Freyer and R.M. Sutherland. Proliferative and clonogenic heterogeneity of cells from EMT6/Ro multiclellular spheroids induced by the glucose and oxygen supply. *Cancer Research*, 46:3513–3520, 1986.

[56] J.P. Freyer and R.M. Sutherland. Regulation of growth saturation and development of necrosis in EMT6/Ro multicellular spheroids by the glucose and oxygen supply. *Cancer Research*, 46(7):3504–3512, 1986.

[57] J.P. Freyer, E. Tustanoff, A.J. Franko, and R.M. Sutherland. In situ consumption rates of cells inV-79 multicellular spheroids during growth. *Journal of Cellular Physiology*, 118:53–61, 1984.

[58] K.S. Furukawa, K. Imura, T. Tateishi, and T. Ushida. Scaffold-free cartilage by rotational culture for tissue engineering. *Journal of Biotechnology*, 133(1):134–145, 2008.

[59] C.J. Galban and B.R. Locke. Analysis of cell-growth in a polymer scaffold using a moving boundary approach. *Biotechnology and Bioengineering*, 56(4):422–432, 1997.

[60] C.J. Galban and B.R. Locke. Analysis of cell growth kinetics and substrate diffusion in a polymer scaffold. *Biotechnology and Bioengineering*, 65(2):121–132, 1999.

[61] C.J. Galban and B.R. Locke. Effects of spatial variation of cells and nutrient and product concentrations coupled with product inhibition on cell growth in a polymer scaffold. *Biotechnology and Bioengineering*, 64(6):633–643, 1999.

[62] B. Gardiner, D. Smith, P. Pivonka, A. Grodzinsky, E. Frank, and L. Zhang. Solute transport in cartilage undergoing cyclic deformation. *Computer Methods in Biomechanics and Biomedical Engineering*, 10(4):265–278, 2007.

[63] L.C. Garg and T.H. Maren. The rates of hydration of carbon dioxide and dehydration of carbonic acid at 37°C. *Biochimica et Biophysica Acta (BBA) - General Subjects*, 262(1):70–76, 1972.

[64] K. Garikipati, EM Arruda, K. Grosh, H. Narayanan, and S. Calve. A continuum treatment of growth in biological tissue: the coupling of mass transport and mechanics. *Journal of the Mechanics and Physics of Solids*, 52(7):1595–1625, 2004.

[65] R.A. Gatenby and E.T. Gawlinski. A reaction-diffusion model of cancer invasion. *Cancer Research*, 56(24):5745–5753, 1996.

[66] R.A. Gatenby and R.J. Gillies. Why do cancers have high aerobic glycolysis? *Nature Reviews Cancer*, 4(11):891–899, 2004.

[67] A. Goriely and M. Ben Amar. On the definition and modeling of incremental, cumulative, and continuous growth laws in morphoelasticity. *Biomechanics and Modeling in Mechanobiology*, 6(5):289–296, 2007.

[68] H.P. Greenspan. Models for the growth of a solid tumor by diffusion. *Studies in Applied Mathematics*, 52(3):17–340, 1972.

[69] A.J. Grodzinsky, M.E. Levenston, M. Jin, and E.H. Frank. Cartilage tissue remodeling in response to mechanical forces. *Annual Review of Biomedical Engineering*, 2(1):691–713, 2000.

[70] T. Grunhagen, G. Wilde, D.M. Soukane, S.A. Shirazi-Adl, and J.P.G. Urban. Nutrient supply and intervertebral disc metabolism. *The Journal of Bone and Joint Surgery*, 88(2):30–35, 2006.

[71] C.L. Hall. *Modelling of some biological materials using continuum mechanics*. PhD thesis, Queensland University of Technology, Brisbane, Australia, 2008.

[72] A.J. Hayes, A. Hall, L. Brown, R. Tubo, and B. Caterson. Macromolecular organization and in vitro growth characteristics of scaffold-free neocartilage grafts. *Journal of Histochemistry and Cytochemistry*, 55(8):853–866, 2007.

[73] G. Helmlinger, P.A. Netti, H.C. Lichtenbeld, R.J. Melder, and R.K. Jain. Solid stress inhibits the growth of multicellular tumor spheroids. *Nature Biotechnology*, 15(8):778–783, 1997.

[74] G. Helmlinger, A. Sckell, M. Dellian, N.S. Forbes, and R.K. Jain. Acid production in glycolysis-impaired tumors provides new insights into tumor metabolism. *Clinical Cancer Research*, 8(4):1284–1291, 2002.

[75] Y. Henrotin, B. Kurz, and T. Aigner. Oxygen and reactive oxygen species in cartilage degradation: friends or foes? *Osteoarthritis and Cartilage*, 13(8):643–654, 2005.

[76] H.K. Heywood, M.M. Knight, and D.A. Lee. Both superficial and deep zone articular chondrocyte subpopulations exhibit the crabtree effect but have different basal oxygen consumption rates. *Journal of Cellular Physiology*, 223:630–639, 2010.

[77] H.K. Heywood and D.A. Lee. Monolayer expansion induces an oxidative metabolism and ROS in chondrocytes. *Biochemical and Biophysical Research Communications*, 373(2):224–229, 2008.

[78] L. Hlatky, R.K. Sachs, and E.L. Alpen. Joint oxygen-glucose deprivation as the cause of necrosis in a tumor analog. *Journal of Cellular Physiology*, 134:167–178, 1988.

[79] M. Hockel, K. Schlenger, S. Hockel, and P. Vaupel. Hypoxic cervical cancers with low apoptotic index are highly aggressive. *Cancer Research*, 59(18):4525 – 4528, 1999.

[80] S. Holm, A. Maroudas, J.P.G. Urban, G. Selstam, and A. Nachemson. Nutrition of the intervertebral disc: solute transport and metabolism. *Connective Tissue Research*, 8(2):101–119, 1981.

[81] W.Y. Hsiang. On the sphere packing problem and the proof of Keplers conjecture. *International Joural of Mathematics*, 4(5):739–831, 1993.

[82] J.D. Humphrey. Review paper: Continuum biomechanics of soft biological tissues. *Proceedings of the Royal Society of London. Series A: Mathematical, Physical and Engineering Sciences*, 459(2029):3–46, 2003.

[83] E.B. Hunziker. Articular cartilage repair: basic science and clinical progress. a review of the current status and prospects. *Osteoarthritis and Cartilage*, 10(6):432–463, 2002.

[84] D.W. Hutmacher. Scaffolds in tissue engineering bone and cartilage. *Biomaterials*, 21(24):2529–2543, 2000.

[85] M.M. Hyttinen, J. Holopainen, P.R. van Weeren, E.C. Firth, H.J. Helminen, and P.A.J. Brama. Changes in collagen fibril network organization and proteoglycan distribution in equine articular cartilage during maturation and growth. *Journal of Anatomy*, 215(5):584–591, 2009.

[86] H. Ishihara and J.P.G. Urban. Effects of low oxygen concentrations and metabolic inhibitors on proteoglycan and protein synthesis rates in the intervertebral disc. *Journal of Orthopaedic Research*, 17(6):829–835, 2005.

[87] Y. Jiang, J. Pjesivac-Grbovic, C. Cantrell, and J.P. Freyer. A multiscale model for avascular tumor growth. *Biophysical Journal*, 89(6):3884–3894, 2005.

[88] A.F. Jones, H.M. Byrne, J.S. Gibson, and J.W. Dold. A mathematical model of the stress induced during avascular tumour growth. *Journal of Mathematical Biology*, 40(6):473–499, 2000.

[89] M. Kaczmarek, R.P. Subramaniam, and S.R. Neff. The hydromechanics of hydrocephalus: steady-state solutions for cylindrical geometry. *Bulletin of Mathematical Biology*, 59(2):295–323, 1997.

[90] A. Khademhosseini, J. Vacanti, and R. Langer. Progress in tissue engineering. *Scientific American Magazine*, 300(5):64–71, 2009.

[91] E.D. Kirson, Z. Gurvich, R. Schneiderman, E. Dekel, A. Itzhaki, Y. Wasserman, R. Schatzberger, and Y. Palti. Disruption of cancer cell replication by alternating electric fields. *Cancer Research*, 64(9):3288–3295, 2004.

[92] C. Koike, T.D. McKee, A. Pluen, S. Ramanujan, K. Burton, L.L. Munn, Y. Boucher, and R.K. Jain. Solid stress facilitates spheroid formation: potential involvement of hyaluronan. *British Journal of Cancer*, 86(6):947–953, 2002.

[93] L.A. Kunz, K. Groebe, and W. Mueller-Klieser. Oncogene-associated growth behavior and oxygenation of multicellular spheroids from rat embryo fibroblasts. *Advances in Experimental Medicine and Biology*, 345:359–366, 1994.

[94] J.C. Lagarias, J.A. Reeds, M.H. Wright, and P.E. Wright. Convergence properties of the nelder-mead simplex method in low dimensions. *SIAM Journal on Optimization*, 9(1):112–147, 1999.

[95] K.A. Landman and C.P. Please. Tumour dynamics and necrosis: surface tension and stability. *IMA Journal of Mathematics Applied in Medicine and Biology*, 18(2):131–158, 2001.

[96] J. Landry, J.P. Freyer, and R.M Sutherland. Shedding of mitotic cells from the surface of multicell spheroids during growth. *Journal of Cellular Physiology*, 106:23–32, 1981.

[97] J. Landry, J.P. Freyer, and R.M. Sutherland. A model for the growth of multicellular spheroids. *Cell Proliferation*, 15(6):585–594, 1982.

[98] R.G. LeBaron and K.A. Athanasiou. Ex vivo synthesis of articular cartilage. *Biomaterials*, 21(24):2575–2587, 2000.

[99] R.B. Lee and J.P.G. Urban. Evidence for a negative Pasteur effect in articular cartilage. *Biochemical Journal*, 321(1):95–102, 1997.

[100] G. Lemon, J.R. King, H.M. Byrne, O.E. Jensen, and K.M. Shakesheff. Mathematical modelling of engineered tissue growth using a multiphase porous flow mixture theory. *Journal of Mathematical Biology*, 52(5):571–594, 2006.

[101] J.R. Levick. Flow through interstitium and other fibrous matrices. *Experimental Physiology*, 72(4):409–438, 1987.

[102] M.C. Lewis, B.D. MacArthur, J. Malda, G. Pettet, and C.P. Please. Heterogeneous proliferation within engineered cartilaginous tissue: the role of oxygen tension. *Biotechnology and Bioengineering*, 91(5):607–615, 2005.

[103] M.C. Lewis, B.D. MacArthur, R.S. Tare, R.O.C. Oreffo, and C.P. Please. Extracellular matrix deposition in engineered micromass cartilage pellet cultures: Measurements and modelling. Unpublished.

[104] C.K.N. Li. The glucose distribution in 9L rat brain multicell tumor spheroids and its effect on cell necrosis. *Cancer*, 50(10):2066–2073, 1982.

[105] L.S. Lohmander. Tissue engineering of cartilage: do we need it, can we do it, is it good and can we prove it? In *Tissue Engineering of Cartilage and Bone*, volume 249, page 2. Novartis Foundation symposium, Wiley, 2003.

[106] X.L. Lu, D.D.N. Sun, X.E. Guo, F.H. Chen, W.M. Lai, and V.C. Mow. Indentation determined mechanoelectrochemical properties and fixed charge density of articular cartilage. *Annals of Biomedical Engineering*, 32(3):370–379, 2004.

[107] V.A. Lubarda and A. Hoger. On the mechanics of solids with a growing mass. *International Journal of Solids and Structures*, 39(18):4627–4664, 2002.

[108] C. Lubke, J. Ringe, V. Krenn, G. Fernahl, S. Pelz, R. Kreusch-Brinker, M. Sittinger, and M. Paulitschke. Growth characterization of neo porcine cartilage pellets and their use in an interactive culture model. *Osteoarthritis and Cartilage*, 13(6):478–487, 2005.

[109] A. Lyshchik, T. Higashi, R. Asato, S. Tanaka, J. Ito, J.J. Mai, C. Pellot-Barakat, M.F. Insana, A.B. Brill, T. Saga, M. Hiraoka, and K. Togashi. Thyroid gland tumor diagnosis at US elastography. *Radiology*, 237(1):202–211, 2005.

[110] B.D. MacArthur and C.P. Please. Residual stress generation and necrosis formation in multi-cell tumour spheroids. *Journal of Mathematical Biology*, 49(6):537–552, 2004.

[111] B.D. MacArthur, C.P. Please, M. Taylor, and R.O.C. Oreffo. Mathematical modelling of skeletal repair. *Biochemical and Biophysical Research Communications*, 313(4):825–833, 2004.

[112] P. Mainil-Varlet, T. Aigner, M. Brittberg, P. Bullough, A. Hollander, E. Hunziker, R. Kandel, S. Nehrer, K. Pritzker, S. Roberts, and E. Stauffer. Histological assessment of cartilage repair: a report by the histology endpoint committee of the international cartilage repair society (icrs). *The Journal of Bone and Joint Surgery*, 85(2):45–57, 2003.

[113] J. Malda, J. Rouwkema, D.E. Martens, E.P. Le Comte, F.K. Kooy, J. Tramper, C.A. Van Blitterswijk, and J. Riesle. Oxygen gradients in tissue-engineered PEGT/PBT cartilaginous constructs: measurement and modeling. *Biotechnology and Bioengineering*, 86(1):9–18, 2004.

[114] J. Malda and W. Schuurman. Personal Communication, 2008 - 2010.

[115] R.L. Mauck, M.A. Soltz, C.C.B. Wang, D.D. Wong, P.H.G. Chao, W.B. Valhmu, C.T. Hung, and G.A. Ateshian. Functional tissue engineering of articular cartilage through dynamic loading of chondrocyte-seeded agarose gels. *Journal of Biomechanical Engineering*, 122:252–260, 2000.

[116] Millipore. Products. millicell cell culture insert. http://www.millipore.com/catalogue/item/picm01250, March 2009.

[117] S. Modok, P. Hyde, H.R. Mellor, T. Roose, and R. Callaghan. Diffusivity and distribution of vinblastine in three-dimensional tumour tissue: Experimental and mathematical modelling. *European Journal of Cancer*, 42(14):2404–2413, 2006.

[118] S. Modok, R. Scott, R.A. Alderden, M.D. Hall, H.R. Mellor, S. Bohic, T. Roose, T.W. Hambley, and R. Callaghan. Transport kinetics of four-and six-coordinate platinum compoundsin the multicell layer tumour model. *British Journal of Cancer*, 97(2):194–200, 2007.

[119] D. Mokhbi Soukane, A. Shirazi-Adl, and J.P.G. Urban. Analysis of nonlinear coupled diffusion of oxygen and lactic acid in intervertebral discs. *Journal of Biomechanical Engineering*, 127(7):1121–1126, 2005.

[120] D. Mokhbi Soukane, A. Shirazi-Adl, and J.P.G. Urban. Computation of coupled diffusion of oxygen, glucose and lactic acid in an intervertebral disc. *Journal of Biomechanics*, 40(12):2645–2654, 2007.

[121] D.O. Morgan. *The Cell Cycle: Principles of Control*. New Science Press, 2007.

[122] W. Mueller-Klieser. Method for the determination of oxygen consumption rates and diffusion coefficients in multicellular spheroids. *Biophysical Journal*, 46(3):343–348, 1984.

[123] W. Mueller-Klieser. Three-dimensional cell cultures: from molecular mechanisms to clinical applications. *American Journal of Physiology - Cell Physiology*, 273(4):C1109–1123, 1997.

[124] W. Mueller-Klieser. Tumor biology and experimental therapeutics. *Critical Reviews in Oncology/Hematology*, 36:123–139, 2000.

[125] W. Mueller-Klieser, JP Freyer, and RM Sutherland. Influence of glucose and oxygen supply conditions on the oxygenation of multicellular spheroids. *British Journal of Cancer*, 53(3):345–353, 1986.

[126] W.F. Mueller-Klieser and R.M. Sutherland. Oxygen tensions in multicell spheroids of two cell lines. *British Journal of Cancer*, 45(2):256–264, 1982.

[127] A.D. Murdoch, L.M. Grady, M.P. Ablett, T. Katopodi, R.S. Meadows, and T.E. Hardingham. Chondrogenic differentiation of human bone marrow stem cells in transwell cultures: generation of scaffold-free cartilage. *Stem Cells*, 25(11):2786–2796, 2007.

[128] C.L. Murphy and A. Sambanis. Effect of oxygen tension and alginate encapsulation on restoration of the differentiated phenotype of passaged chondrocytes. *Tissue Engineering*, 7(6):791–803, 2001.

[129] D. Nehring, P. Adamietz, N.M. Meenen, and R. Portner. Perfusion cultures and modelling of oxygen uptake with three-dimensional chondrocyte pellets. *Biotechnology Techniques*, 13(10):701–706, 1999.

[130] J.A. Nelder and R. Mead. A simplex method for function minimization. *The Computer Journal*, 7(4):308–313, 1965.

[131] K. Newell, A. Franchi, J. Pouysségur, and I. Tannock. Studies with glycolysis-deficient cells suggest that production of lactic acid is not the only cause of tumor acidity. *Proceedings of the National Academy of Sciences of the United States of America*, 90(3):1127–1131, 1993.

[132] J.S. Newman and K.E. Thomas-Alyea. *Electrochemical Systems*. Number 3. Wiley-IEEE, 2004.

[133] NHS. Cartilage damage. http://www.nhs.uk/conditions/cartilage-damage/Pages/Introduction.aspx, June 2010.

[134] B. Obradovic, R.L. Carrier, G. Vunjak-Novakovic, and L.E. Freed. Gas exchange is essential for bioreactor cultivation of tissue engineered cartilage. *Biotechnology and Bioengineering*, 63(2):197–205, 1999.

[135] B. Obradovic, J.H. Meldon, L.E. Freed, and G. Vunjak-Novakovic. Glycosaminoglycan deposition in engineered cartilage: experiments and mathematical model. *AIChE Journal*, 46(9):1860–1871, 2000.

[136] R.D. O'Dea, S.L. Waters, and H.M. Byrne. A two-fluid model for tissue growth within a dynamic flow environment. *European Journal of Applied Mathematics*, 19(6):607–634, 2008.

[137] G. Ofek, C.M. Revell, J.C. Hu, D.D. Allison, K.J. Grande-Allen, and K.A. Athanasiou. Matrix development in self-assembly of articular cartilage. *PLoS ONE*, 3(7):e2795, 2008.

[138] P. Otte. Basic cell metabolism of articular cartilage. manometric studies. *Zeitschrift fur Rheumatologie*, 50(5):304–312, 1991.

[139] E. Palsson. A three-dimensional model of cell movement in multicellular systems. *Future Generation Computer Systems*, 17(7):835–852, 2001.

[140] E. Palsson and H.G. Othmer. A model for individual and collective cell movement in dictyostelium discoideum. *Proceedings of the National Academy of Sciences of the United States of America*, 97(19):10448–10453, 2000.

[141] K. Park, J. Huang, F. Azar, R.L. Jin, B.H. Min, D.K. Han, and K. Hasty. Scaffold-free, engineered porcine cartilage construct for cartilage defect repair in vitro and in vivo study. *Artificial Organs*, 30(8):586–596, 2006.

[142] G.A. Pavliotis and A.M. Stuart. *Multiscale Methods: Averaging and Homogenization*. Springer, 2008.

[143] G.J. Pettet, C.P. Please, M.J. Tindall, and D.L.S. McElwain. The migration of cells in multicell tumor spheroids. *Bulletin of Mathematical Biology*, 63(2):231–257, 2001.

[144] E.S. Place, N.D. Evans, and M.M. Stevens. Complexity in biomaterials for tissue engineering. *Nature Materials*, 8:457–470, 2009.

[145] C.P. Please, G. Pettet, and D.L.S. McElwain. A new approach to modelling the formation of necrotic regions in tumours. *Applied Mathematics Letters*, 11(3):89–94, 1998.

[146] C.P. Please, G. Pettet, and D.L.S. McElwain. Avascular tumour dynamics and necrosis. *Mathematical Models and Methods in Applied Sciences*, 9(4):569–579, 1999.

[147] C. Richter, M. Schweizer, A. Cossarizza, and C. Franceschi. Control of apoptosis by the cellular ATP level. *FEBS Letters*, 378(2):107–110, 1996.

[148] J. Riesle, A.P. Hollander, R. Langer, L.E. Freed, and G. Vunjak-Novakovic. Collagen in tissue-engineered cartilage: types, structure, and crosslinks. *Journal of Cellular Biochemistry*, 71(3):313–327, 1998.

[149] E.K. Rodriguez, A. Hoger, and A.D. McCulloch. Stress-dependent finite growth in soft elastic tissues. *Journal of Biomechanics*, 27(4):455–467, 1994.

[150] T. Roose. Personal Communication, 2009 - 2010.

[151] T. Roose, S.J. Chapman, and P.K. Maini. Mathematical models of avascular tumor growth. *SIAM Review*, 49(2):179–208, 2007.

[152] E. Sanchez-Palencia. *Non-homogeneous media and vibration theory*, volume 127 of *Lecture Notes in Physics*. Springer-Verlag, Berlin, 1980.

[153] S. Scheiner, P. Pivonka, and DW Smith. Two-scale model for electro-diffusive transport through charged porous materials. In *IOP Conference Series: Materials Science and Engineering*, volume 10, page 012112. IOP Publishing, 2010.

[154] J.E. Scott. Proteoglycan-fibrillar collagen interactions. *Biochemical Journal*, 252(2):313–323, 1988.

[155] B.G. Sengers. *Modeling the development of tissue engineered cartilage*. PhD thesis, Technische Universiteit Eindhoven, 2005.

[156] B.G. Sengers. Personal Communication, 2008 - 2010.

[157] B.G. Sengers, M. Taylor, C.P. Please, and R.O.C. Oreffo. Computational modelling of cell spreading and tissue regeneration in porous scaffolds. *Biomaterials*, 28(10):1926–1940, 2007.

[158] B.G. Sengers, C.C. Van Donkelaar, C.W.J. Oomens, and F.P.T. Baaijens. The local matrix distribution and the functional development of tissue engineered cartilage, a finite element study. *Annals of Biomedical Engineering*, 32(12):1718–1727, 2004.

[159] B.G. Sengers, C.C. Van Donkelaar, C.W.J. Oomens, and F.P.T. Baaijens. Computational study of culture conditions and nutrient supply in cartilage tissue engineering. *Biotechnology Progress*, 21(4):1252–1261, 2005.

[160] A. Serafini-Fracassini and J.W. Smith. *The Structure and Biochemistry of Cartilage*. Churchill Livingstone, 1974.

[161] J.A. Sherratt and M.A.J. Chaplain. A new mathematical model for avascular tumour growth. *Journal of Mathematical Biology*, 43(4):291–312, 2001.

[162] R.J. Shipley, G.W. Jones, R.J. Dyson, B.G. Sengers, C.L. Bailey, C.J. Catt, C.P. Please, and J. Malda. Design criteria for a printed tissue engineering construct: A mathematical homogenization approach. *Journal of Theoretical Biology*, 259(3):489–502, 2009.

[163] D. Shweiki, M. Neeman, A. Itin, and E. Keshet. Induction of vascular endothelial growth factor expression by hypoxia and by glucose deficiency in multicell spheroids: implications for tumor angiogenesis. *Proceedings of the National Academy of Sciences of the United States of America*, 92(3):768–772, 1995.

[164] Sigma-Aldrich. Cell culture products: Product directory: Basal medium eagle (BME). www.sigmaaldrich.com/life-science/cell-culture/cell-culture-products.html?TablePage=9628432, July 2010.

[165] Sigma-Aldrich. Media formulations: Dulbecco's modified eagle's medium (DME) formulation. http://www.sigmaaldrich.com/life-science/cell-culture/learning-center/media-formulations/dme.html, July 2010.

[166] A.J.M. Spencer. *Continuum Mechanics*. Dover Publications, 2004.

[167] U.A. Stock and J.P. Vacanti. Tissue engineering: Current state and prospects. *Annual Review of Medicine*, 52(1):443–451, 2001.

[168] R.A. Stockwell. Chondrocytes. *Journal of Clinical Pathology*, 31(12):7–13, 1978.

[169] R.A. Stockwell. *Biology of Cartilage Cells*. Cambridge University Press, 1979.

[170] E.A. Swabb, J. Wei, and P.M. Gullino. Diffusion and convection in normal and neoplastic tissues. *Cancer Research*, 34(10):2814–2822, 1974.

[171] I.F. Tannock. The relationship between cell proliferation and the vascular system in a transplanted mouse mammary tumour. *British Journal of Cancer*, 22(2):258–273, 1968.

[172] I.F. Tannock and R. Rotin. Acid pH in tumors and its potential for therapeutic exploitation. *Cancer Research*, 49(16):4373–4384, 1989.

[173] R.S. Tare, D. Howard, J.C. Pound, H.I. Roach, and R.O.C. Oreffo. Tissue engineering strategies for cartilage generation-micromass and three dimensional cultures using human chondrocytes and a continuous cell line. *Biochemical and Biophysical Research Communications*, 333:609–621, 2005.

[174] The MathWorks, Inc. MATLAB V7.9.0.529 (R2009b), 2009.

[175] G.J. Tortora and B.H. Derrickson. *Principles of Anatomy and Physiology*, volume 1. NJ: Wiley, 12th. international student edition, 2009.

[176] P.A. Torzilli, D.A. Grande, and J.M. Arduino. Diffusive properties of immature articular cartilage. *Journal of Biomedical Materials Research*, 40(1):132–138, 1998.

[177] O. Tredan, C.M. Galmarini, K. Patel, and I.F. Tannock. Drug resistance and the solid tumor microenvironment. *Journal of the National Cancer Institute*, 99(19):1441–1454, 2007.

[178] A.J. Trewenack, C.P. Please, and K.A. Landman. A continuum model for the development of tissue-engineered cartilage around a chondrocyte. *Mathematical Medicine and Biology*, 26(3):241–262, 2009.

[179] Cancer Research UK. Cancerstats key facts on cancer. cancer in the uk: July 2010. http://info.cancerresearchuk.org/cancerstats/index.htm, August 2010.

[180] J.P.G. Urban. The chondrocyte: a cell under pressure. *Rheumatology*, 33(10):901–908, 1994.

[181] M.G. Vander Heiden, L.C. Cantley, and C.B. Thompson. Understanding the warburg effect: the metabolic requirements of cell proliferation. *Science*, 324(5930):1029–1033, 2009.

[182] G. Vunjak-Novakovic, I. Martin, B. Obradovic, S. Treppo, A.J. Grodzinsky, R. Langer, and L.E. Freed. Bioreactor cultivation conditions modulate the composition and mechanical properties of tissue-engineered cartilage. *Journal of Orthopaedic Research*, 17(1):130–138, 1999.

[183] S. Walenta, J. Doetsch, W. Mueller-Klieser, and L.A. Kunz-Schughart. Metabolic imaging in multicellular spheroids of oncogene-transfected fibroblasts. *Journal Histochemistry and Cytochemistry*, 48(4):509–522, 2000.

[184] S. Walenta, M. Wetterling, M. Lehrke, G. Schwickert, K. Sundfor, E. K. Rofstad, and W. Mueller-Klieser. High lactate levels predict likelihood of metastases, tumor recurrence, and restricted patient survival in human cervical cancers. *Cancer Research*, 60(4):916–921, 2000.

[185] O. Warburg. On the origin of cancer cells. *Science*, 123(3191):309–314, 1956.

[186] J.P. Ward and J.R. King. Mathematical modelling of avascular-tumour growth. *Mathematical Medicine and Biology*, 14:39–69, 1997.

[187] J.P. Ward and J.R. King. Modelling the effect of cell shedding on avasacular tumour growth. *Computational and Mathematical Methods in Medicine*, 2(3):155–174, 2000.

[188] J.P. Ward and J.R. King. Mathematical modelling of drug transport in tumour multicell spheroids and monolayer cultures. *Mathematical Biosciences*, 181(2):177–207, 2003.

[189] P.R. Weeren, E.C. Firth, H. Brommer, M.M. Hyttinen, H.J. Helminen, C.W. Rogers, J. Degroot, and P.A.J. Brama. Early exercise advances the maturation of glycosaminoglycans and collagen in the extracellular matrix of articular cartilage in the horse. *Equine Veterinary Journal*, 40(2):128–135, 2008.

[190] R.J. Whittaker, R. Booth, R. Dyson, C. Bailey, L. Parsons Chini, S. Naire, S. Payvandi, Z. Rong, H. Woollard, L.J. Cummings, et al. Mathematical modelling of fibre-enhanced perfusion inside a tissue-engineering bioreactor. *Journal of Theoretical Biology*, 256(4):533–546, 2009.

[191] C.C. Widnell and K.H. Pfenninger. *Essential Cell Biology*. Williams & Wilkins, 1990.

[192] R.A.J. Windhaber, R.J. Wilkins, and D. Meredith. Functional characterisation of glucose transport in bovine articular chondrocytes. *Pflugers Archiv European Journal of Physiology*, 446(5):572–577, 2003.

[193] R. Wu and E. Racker. Regulatory mechanisms in carbohydrate metabolism. *Journal of Biological Chemistry*, 234(5):1036–1041, 1959.

[194] W. Yang, W.Y. Yang, W. Cao, T.S. Chung, and J. Morris. *Applied Numerical Methods Using MATLAB*. Wiley-Interscience, 2005.

[195] L. Zhang, B.S. Gardiner, D.W. Smith, P. Pivonka, and A.J. Grodzinsky. Integrated model of IGF-I mediated biosynthesis in a deformed articular cartilage. *Journal of Engineering Mechanics*, 135(5):439–449, 2009.

[196] S. Zhou, Z. Cui, and J.P.G. Urban. Factors influencing the oxygen concentration gradient from the synovial surface of articular cartilage to the cartilage-bone interface: a modeling study. *Arthritis & Rheumatism*, 50(12):3915–3924, 2004.

[197] S. Zhou, Z. Cui, and J.P.G. Urban. Nutrient gradients in engineered cartilage: Metabolic kinetics measurement and mass transfer modeling. *Biotechnology and Bioengineering*, 101(2):408–421, 2008.